Chemical Etching of Semiconductors Assisted by Graphene Oxide

Wataru Kubota

2023

Chemical Etching of Semiconductors Assisted by Graphene Oxide

A dissertation submitted to
Graduate School of Engineering,
Kyoto University

in partial fulfillment of the requirements
for the degree of
Doctor of Philosophy in Engineering

by

Wataru Kubota

2023

Abstract

Micro-nano processing for the functionalization of materials is one of the important approaches for revealing their potential. The development of micro-nano processing enables the integration of an enormous number of functions in a unit area and the extraction of unique functions that only emerge from nanostructures. In the field of semiconductors, many researchers have devoted their efforts to the development of micro-nano processing in the last several decades.

Chemical etching of semiconductors assisted by various types of catalysts is drawing much attention as one of the wet anisotropic etching methods for fabricating their micro-nano structures. Although noble metals are usually utilized as the catalysts, the utilization of metal materials is undesirable for semiconductor processes. The aim of this thesis is to apply graphene oxide, a 2D nanocarbon material, for the catalyst of semiconductor etching reactions and to reveal its catalytic mechanism.

In chapter 1, a brief review of semiconductor processing, catalyst-assisted etching of semiconductors, and graphene oxide were described.

In chapter 2, the catalytic activity of graphene oxide toward silicon etching reaction in a wet process is revealed and its catalytic mechanism with the etchant of HF-HNO_3 solution is discussed in terms of reaction kinetics and a catalytic active center of graphene oxide. The selection of the oxidant in the etchant influences the etching rate due to the difference in the catalytic activity of graphene oxide towards the oxidant reduction reaction. In the case of HF-HNO_3 etchant, the amount of adsorbed NO_3^- on silicon or graphene oxide surfaces affects the etching rate, and structural defects on graphene oxide have an advantage in terms of its adsorption, which results in the enhancement of the etching reaction under graphene oxide.

In chapter 3, chemical etching of silicon assisted by graphene oxide in vapor phase is suggested. The vapor phase etching can restrict the problems of porous structure formation and pealing of GO during the etching process which occurred in the assisted etching in the liquid phase. Furthermore, µm-order site-selective etching of silicon is demonstrated by combining the vapor phase assisted etching process and micro-contact printing of graphene oxide.

In chapter 4, etching behaviors of GO-loaded InP substrate in various types of etching solutions were reported. In the assisted etching of InP, the stability of its oxide affects the etching behavior. When the oxidant reduction is the rate-determining step in the assisted etching reaction by utilizing the optimized etchant, GO enhances the etching reaction due to its catalytic activity towards the oxidant reduction reaction.

In chapter 5, a summary and a conclusion of this thesis are described, and the outlook of chemical etching of semiconductors assisted by graphene oxide is suggested for further improvement and more practical application of this etching process.

Table of contents

Chapter 1 Introduction 1

1.1 Semiconductor processing..1

1.2 Catalyst-assisted chemical etching of semiconductors..2

1.3 Graphene Oxide...4

1.4 Objectives and outlines of this thesis...5

Chapter 2 Chemical etching of silicon assisted by graphene oxide in liquid phase 10

2.1 Introduction 10

2.2 Experimental procedure 10

2.2.1 Preparation of GO 10

2.2.2 GO-assisted silicon etching in liquid phase 11

2.3 Etching behavior with various types of etching compositions 12

2.3.1 Chemical etching of silicon assisted by graphene oxide in HF-H_2O_2 12

2.3.2 Chemical etching of silicon assisted by graphene oxide in HF-HNO_3 18

2.4 Reaction kinetics of GO-assisted silicon etching in HF-HNO_3 solution 23

2.5 Catalytic mechanism of GO-assisted silicon etching...27

2.6 Conclusion..32

Chapter 3 Vapor phase chemical etching of silicon assisted by graphene oxide 33

3.1 Introduction 33

3.2 Experimental procedure 34

3.2.1 Vapor phase GO-assisted silicon etching......34

3.2.2 Micro-contact printing of GO......35

3.3 Etching behavior with various types of etching compositions......37

3.4 The mechanism of vapor phase etching of silicon assisted by GO......43

3.5 Pattern etching of silicon assisted by patterned GO by combining μCP......51

3.6 Conclusion......56

Chapter 4 Chemical etching of InP assisted by graphene oxide......57

4.1 Introduction......57

4.2 Experimental procedure......57

4.3 Etching behavior with various types of etching compositions......59

4.4 Conclusion......71

Chapter 5 Conclusion and outlook......72

Appendix Local current mapping of electrochemically-exfoliated graphene oxide by conductive AFM......75

A.1 Introduction......75

A.2 Experimental procedure......77

A.2.1 Synthesis of electrochemically-exfoliated GO and reduction by vacuum ultraviolet light irradiation in high vacuum condition......77

A.2.2 Conductive AFM measurement......78

A.3 Results and discussion......79

A.3.1 Characterization of electrochemically-exfoliated GO......79

A.3.2 Local current mapping of electrochemically-exfoliated GO 84

References 90

Achievements 108

Acknowledgments 111

Chapter 1 Introduction

1.1 Semiconductor processing

The development of the semiconductor industry began with the invention of the transistor by John Bardeen and William B. Shockley in 1947[1]. After the invention of the integrated circuit by Jack Kilby in 1959, many researchers devoted their efforts to minimizing an electric component for the integration of an enormous number of functions in a unit cell. The trend of scaling semiconductor devices has continued to guide Moore's law that component density and performance of integrated circuits doubles every year, which was revised to doubling every two years. However, the chip size shrink trend in the 2D direction has been reaching its limitation because of the limitation of lithography techniques and the lack of reliability on the behavior of quite miniaturized devices[2].

The recent trend of the integration is the 3D stacking for 3D NAND fresh memory[3] or 3D structure FET for logic circuits represented by FinFET[4] and gate-all-around MOSFET[5]. For fabricating these complicated 3D structures, the micro-nano processing of semiconductor surfaces is indispensable for improving their performance. Furthermore, the development of micro-nano processing also enables the extraction of unique functions that only emerge from nanostructures, and the nanostructures are now utilized in nanoelectronics[6,7], bio- and chemical sensors[8,9], and solar cells[10].

A number of methods including both bottom-up and top-down processes are utilized to fabricate ideal nanostructures of semiconductors, such as vapor-liquid-solid growth[11], dry etching[12], and electrochemical etching[13] in the case of silicon. Focused on silicon etching techniques, they are categorized as wet etching and dry etching.

A wet etching enables low-cost and high throughput processing of silicon by attacking the liquid reagents directly to the silicon surfaces without high energy from the outside.

In wet etching, the kind of the etching solution has an influence on the morphology of the structure after etching depending on the rate-determining step in the etching reaction. When a certain reaction such as oxidation and dissolution of silicon restricts the whole etching reaction, the difference in the etching rate towards each orientation affects the morphology, which results in isotropic etching. On the other hand, when the diffusion of reactants or products restricts the whole etching reaction, the etching rate is the same in all directions and the etching proceeds isotropically. These etching behaviors are also seen in compound semiconductors such as InP and GaAs.

A dry etching generally means plasma etching technique. In this process, a glow discharge dissociates and ionizes the gaseous reactants to form reactive and ionic species which react with semiconductors. Although the dry etching needs expensive machines and the damage induced in the etching process is unavoidable, highly accurate processing of semiconductors can be achieved due to side wall passivation simultaneously introduced during the etching and the direction control of ions by the applied bias.

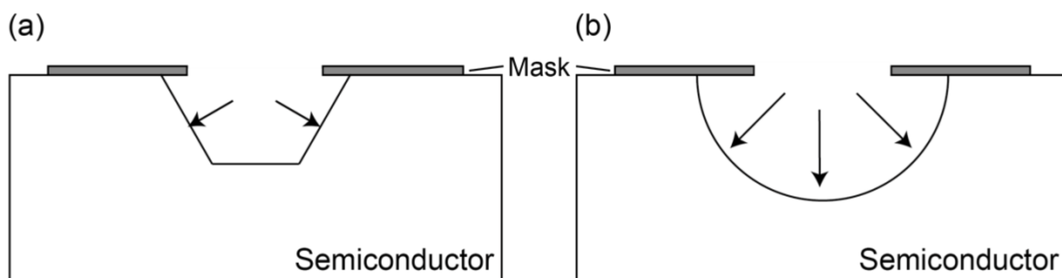

Figure 1-1 Schematic illustrations of (a) anisotropic etching and (b) isotropic etching.

1.2 Catalyst-assisted chemical etching of semiconductors

Since Li and Bohn reported an anisotropic etching of silicon by utilizing noble metals as catalysts for the etching reaction for the first time in 2000[14], metal-assisted chemical etching (Mac Etch) has been attracting increasing attention in the fabrication of

semiconductor micro-nano structures. In this process, when a semiconductor substrate deposited with catalysts is immersed in a solution composed of proper acids and strong oxidants, the semiconductor material under the catalysts dissolves faster than in non-covered areas. In the case of Mac Etch of silicon in HF-H_2O_2 solution which is generally utilized, the reaction equation is described as following cathode and anode reactions,

Cathode reaction

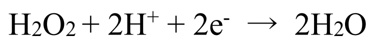
$H_2O_2 + 2H^+ + 2e^- \rightarrow 2H_2O$

Anode reaction

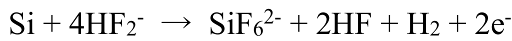
$Si + 4HF_2^- \rightarrow SiF_6^{2-} + 2HF + H_2 + 2e^-$

This anisotropic etching process is suitable for the fabrication of silicon micro-nano structures due to its simplicity, cost-efficiency, and controllability of crystalline quality and morphology. Formation of silicon complex structures, such as zigzag structures[15], nano-cones, and helical structures[16], has been suggested by choosing the optimized noble metal catalyst, etchant compositions, and etching conditions of the Mac Etch process. Furthermore, the application of Mac Etch towards other semiconductor materials of InP[17,18], GaAs[19], InGaAs[20], and SiC[21] has been reported.

Although Mac Etch has a number of advantages for the fabrication of micro-nano structures, the removal of noble metal particles embedded in silicon micro-nano structures is challenging and the remaining metals introduce deep-level traps that markedly affect device performance[22]. Moreover, the acid solution for the metal removal can dissolve compound semiconductors, which deteriorates their morphology.

Some researchers recently suggested the replacement of noble metal materials with non-metal catalysts of carbon materials for semiconductor etching reactions[23–29]. Carbon materials are widely known as catalysts of oxidant reduction in the assisted etching of silicon, such as hydrogen peroxide (H_2O_2)[30], oxygen[27,31], and nitric acid (HNO_3)[32].

Various types of carbon materials, including graphite particles[23,24], carbon nanotubes[25], and graphene[26], have been shown to enhance the silicon etching reaction with an optimized etching solution. Another research group has reported the application of graphene oxide to the catalyst for Ge etching reaction. However, the etching rate of carbon-assisted etching is very slow and its mechanism is still unclear.

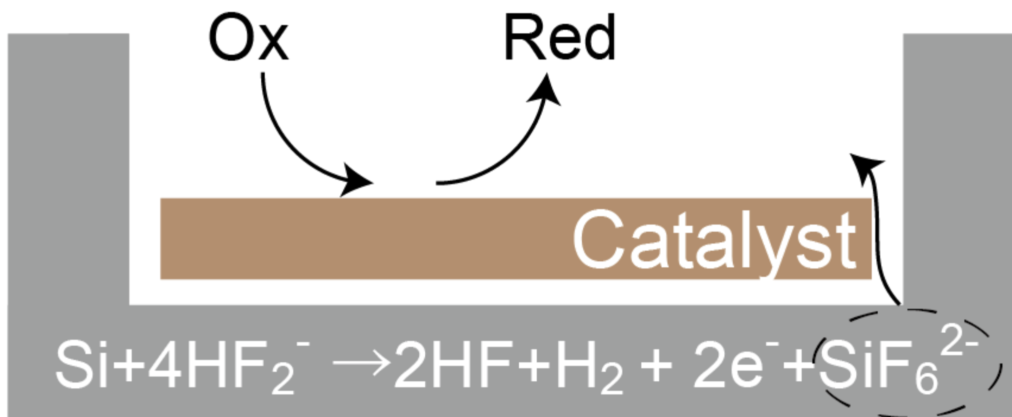

Figure 1-2 A schematic illustration of catalyst-assisted silicon etching.

1.3 Graphene Oxide

Products of oxidated graphite, called graphite oxide, were reported about two hundred years ago. Graphite oxide with a thickness of nm order was first suggested by Kovtyukhova[33], to the best of my knowledge and this monolayer graphite oxide was called graphene oxide (GO) after the discovery of graphene[34]. GO is a carbon-based ultrathin material decorated with ample oxygen functional groups. Various types of GO synthesis processes, represented by Brodie's method, Staudenmaier's method, Hummers' method, etc., are suggested, and different methods can synthesize GO with different structures in not only micro-scales such as sheet size and thickness but also nano-scales such as carbon crystallinity and the amount of oxygen functional groups[35]. Although the structure of GO is still under discussion, the Lerf-Klinowski model is the most accepted

model[36]. In this model, epoxy and hydroxy groups decorate the basal plane of a honeycomb structure of carbon, and carbonyl and carboxy groups are attached to edge areas of GO. These oxygen functional groups enable GO to disperse in some solvents, and solution-based manipulation has the advantage to load easily on a certain surface[37]. GO was in the spotlight as the precursor of graphene in the initial stage[38]. Recently, its unique features of the large specific surface area and the surface interaction with some molecules have been utilized as supercapacitors[39], bio-sensors[40], catalysts[41], and so on.

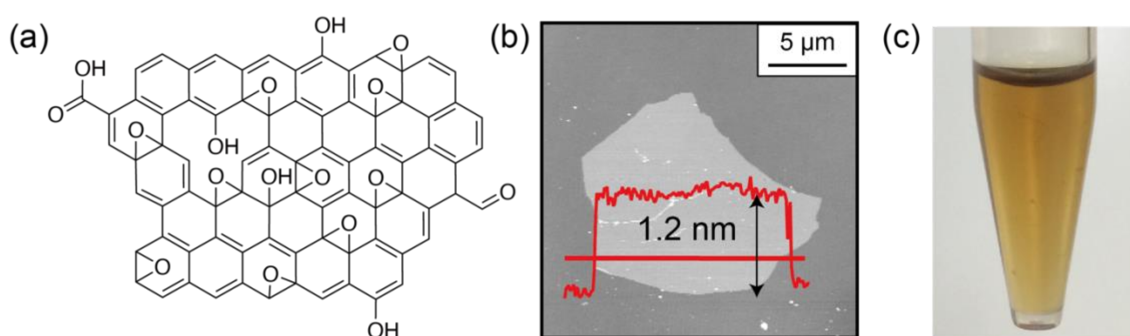

Figure 1-3 (a) A schematic illustration of GO structure. (b) An AFM topographic image of GO. (c) A graphic image of GO dispersion.

1.4 Objectives and outlines of this thesis

In this thesis, the catalytic activity of GO was focused on for its application to the assisted etching of semiconductors. The catalyst for the assisted etching reaction must have the potential to enhance the oxidant reduction reaction utilized in the assisted etching process such as H_2O_2, O_2, or HNO_3. In the case of GO, it has been widely reported that GO enhances the oxygen reduction reaction and applies to the catalyst of fuel cells. Furthermore, it was reported that other oxidant reduction reactions of H_2O_2 and HNO_3 are also catalyzed by GO. Many researchers have discussed the catalytic active center of graphite-related materials from the viewpoint of experiments and

simulations. When graphite-related materials are utilized as catalysts, intrinsic defects, edges, or heteroatoms of those materials play central roles in their catalytic activities[42]. These regions alter the charge or spin distribution of π electrons, enabling oxidants to readily adsorb to the surfaces, thereby increasing chemical reactivity. In terms of defects density, GO has a lot of defects which was introduced in the synthesis process, which can efficiently work as catalytic active sites.

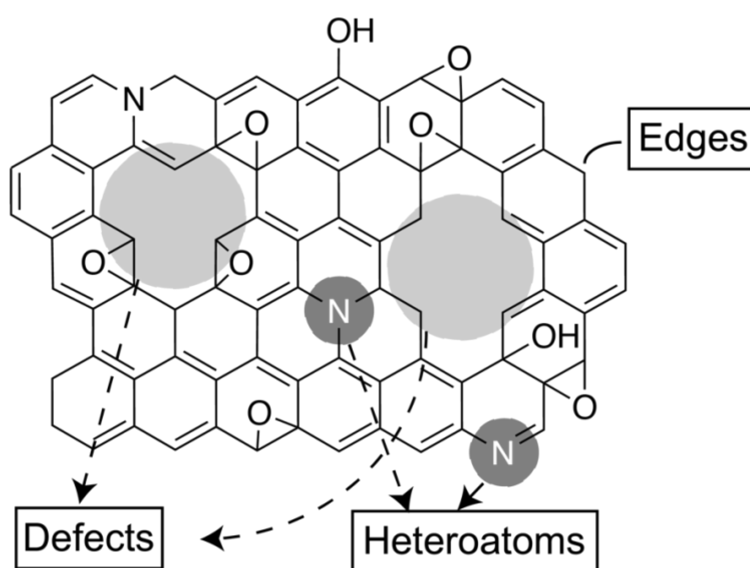

Figure 1-4 A schematic illustration of the catalytic active center of GO structure.

The purpose of this thesis is the semiconductor processing by utilizing GO as the catalyst for the etching reactions. Furthermore, the control of the assisted etching reaction is demonstrated by understanding its reaction mechanism.

The details are as follows.

Chapter 2 Chemical etching of silicon assisted by graphene oxide in liquid phase

In this chapter, GO-assisted silicon etching in liquid phase was demonstrated and its catalytic mechanism was discussed. It was revealed that GO promoted the etching reaction of silicon and that its etching rate was different in the solution containing a

different oxidant. Then, the reaction mechanism of GO-assisted etching was investigated using HF-HNO_3 etchant. The relationship between temperature and etching rate was investigated to understand GO-assisted silicon etching in terms of reaction kinetics. It was found that GO did not decrease the activation energy of the reaction but enhanced the frequency factor mainly due to the adsorption of reactants. Furthermore, when GO with different structural defect densities was applied to the assisted etching catalyst, higher etching rates were obtained for GO with more structural defects, indicating that the structural defects in the GO structure function as catalytic active sites. Based on these results, a catalytic mechanism for GO-assisted silicon etching was proposed, in which oxidants are more easily adsorbed on the GO structural defects than on the silicon surface, and this difference in adsorption frequency generates a difference in etching rate between the GO-covered and bare areas, resulting in the enhancement of the etching under the GO.

Chapter 3 Vapor phase chemical etching of silicon assisted by graphene oxide

In the GO-assisted silicon etching in the liquid phase described in the previous chapter, the following problems were identified. One issue is the peeling of GO sheets by the gases or bubbles produced during the etching process, such as hydrogen and nitrogen dioxide. Another difficulty is the formation of a porous structure during assisted etching. The formation of this layer is a phenomenon that is unique to the assisted etching process. As a new process to solve these problems, assisted etching using the vapor phase method was suggested. This is a method in which the substrate is exposed to etching vapor generated from the etchant, instead of directly immersing the semiconductor substrate in the etchant. It is known that this method does not generate bubbles due to the reaction gas formed in the solution process and suppresses the

formation of a porous structure, although the reaction mechanism is not clear. In this study, the vapor phase method was applied to GO-assisted etching and attempted to solve the problems that arose in the solution process.

It was shown that the etching reaction under GO was enhanced without the formation of a porous structure by using an appropriate solution as a vapor source. In order to investigate the reaction mechanism in the vapor phase method, the temperature dependence of the reaction rate was confirmed, and it was found that the etching rate was saturated at 60°C, suggesting that mass transfer contributed to the rate-determining process in the vapor phase method. Furthermore, a site-selective etching was demonstrated by combining μCP as a position control of GO. GO pattern was transferred to a silicon substrate by pressing a GO-loaded stamp onto the substrate. Pattern etching on the order of μm was achieved by vapor phase etching of silicon substrates on which GO patterns were transferred by μCP.

Chapter 4 Chemical etching of InP assisted by graphene oxide

Recently, metal-assisted etching has been applied to not only silicon but also compound semiconductors. In this chapter, chemical etching of InP assisted by GO was demonstrated, and a possible mechanism of GO-assisted InP etching was suggested by combining XPS analyses. The solubility of the InP oxide layer towards the etching solution affected the rate-determining step of the InP etching reaction. When the oxidant reduction reaction catalyzed by GO was the rate-determining step, the etching reaction under GO was enhanced. Furthermore, the etching behavior was different in utilizing different oxidants, indicating that the catalytic activity of GO for the oxidant reduction also affected the etching behavior.

Chapter 5 Conclusion and outlook

In chapter 5, a summary and a conclusion of this thesis are described, and the outlook of chemical etching of semiconductors assisted by graphene oxide is suggested for further improvement and more practical application of this etching process.

Chapter 2 Chemical etching of silicon assisted by graphene oxide in liquid phase

2.1 Introduction

In this chapter, the catalytic ability of GO for the silicon etching reaction was confirmed. Firstly, the condition of GO-assisted silicon etching was optimized. In general, a couple of reaction, that is, an oxidant reduction reaction and a silicon oxidation reaction, was necessary for the catalyst-assisted silicon etching. In this section, HF-H_2O_2 or HF-HNO_3 solution which is usually used as the etchant for catalyst-assisted silicon etching was utilized as the etchant. Next, temperature dependency on the etching rate was checked and the Arrhenius plot was created to comprehend the catalytic mechanism of GO-assisted silicon etching in the liquid phase in terms of reaction kinetics. Finally, the catalytic active sites on GO were identified by applying two types of GO sheets with different structural features.

2.2 Experimental procedure

2.2.1 Preparation of GO

Two types of GO were prepared by different two methods: a modified Hummers' method (CGO:Chemically-exfoliated Graphene Oxide) and an electrochemical exfoliation method (EGO:Electrochemically-exfoliated Graphene Oxide). Detailed processes were referred to previous reports[43,44]. The main difference between these two methods is the oxidation process. In the case of the modified Hummers' method, graphite powder (Z-100, the average particle size:60 μm, Ito Graphite Co., Ltd.) was mixed with $NaNO_3$ (98%, Nacalai Tesque), concentrated H_2SO_4 (97%, Nacalai Tesque) and $KMnO_4$ (99%, Nacalai Tesque) for 3 days in the ice bath. Then, 5% H_2SO_4 was added to the liquid

obtained, and the mixture was stirred for 2 hours. Furthermore, H_2O_2 (30%, Nacalai Tesque) was added to the mixture and stirred for 2 hours. The mixture was purified by exchanging the supernatant for ultrapure water after centrifuge.

In the electrochemical exfoliation method, regarding Cao's report[44], galvanostatic charging was applied to graphite foil (99.8%, 0.5 mm thickness, Alfa Aesar) in a two-electrode cell with a platinum wire as the cathode and concentrated H_2SO_4 (97 %, Nacalai Tesque) as the electrolyte. The charging current was kept at 100 mA for 20 minutes. After that, the graphite foil was removed from the first electrolyte, and potentiostatic charging was applied to the foil in a two-electrode cell with a platinum wire as the cathode and 0.1 M $(NH_4)_2SO_4$ (99%, Fujifilm Wako Pure Chemical Corp.) aqueous solution as the electrolyte. The charging voltage was kept at 10 V for around 10 minutes to exfoliate thoroughly. The exfoliated graphite flakes were then sonicated for 5 minutes and centrifuged for 10 min to remove the impurity, including $(NH_4)_2SO_4$. It is considered that the electrochemical process is milder than chemical oxidation with strong oxidants, resulting in conductive GO sheets even without reduction treatments[45].

2.2.2 GO-assisted silicon etching in liquid phase

For applying GO sheets to the assisted etching of silicon, each GO sheet was loaded on the silicon substrate at first. A single-side polished Si(100) wafer (1×1 cm^2, 1–10 Ω cm, p-type, boron-doped) was cleaned by sonication in acetone, ethanol, and ultrapure water (a resistivity of 18.2 MΩ•cm) in succession. The substrate was then subjected to the Xe excimer lamp (wavelength: 172 nm, 6~10 mW cm^{-2}, Ushio Co Ltd.) treatment for removing organic contaminations. Then GO sheets were loaded on the silicon substrate by spin-coating (500 rpm for 15 s and then 2000 rpm for 150 s).

Before the etching process, the PTFE beaker for etching was washed with diluted

HNO_3 (70 wt%, for the electrical industry, Fuji Film Wako Pure Chemical Corp) and UPW at 80°C for more than 30 min respectively. The GO-coated silicon substrate was then immersed in the mixture of HF (50 wt%, for the semiconductor industry, Morita Chemical) and oxidant of H_2O_2 (30 wt%, analytical grade, Fuji Film Wako Pure Chemical Corp.) or HNO_3. The surface structure of the obtained samples was observed by atomic force microscopy (AFM, MFP-3D, Oxford Instruments) with an Al-backside-coated Si cantilever (SI-DF40, spring const. 42 N m^{-1}, resonance freq. 280 kHz, Hitachi High-Tech,) in amplitude-modulation mode and 3D laser microscopy (OLS4000-SAT, Olympus). The cross-section of the samples after etching was also observed by scanning electron microscopy (SEM, JSM-6500F, JEOL). The chemical conditions of the samples were analyzed by X-ray photoelectron spectroscopy (XPS, ESCA-3400, Shimadzu). An Mg target was applied using an acceleration voltage and current of 10 kV and 10 mA, respectively. The spectra obtained were calibrated to the Si 2p peak at 99.8 eV[46]. Structural analyses of GO were conducted with micro Raman spectroscopy (μRS, Lucir). The wavelength of the laser for the excitation light source was 532 nm.

2.3 Etching behavior with various types of etching compositions

2.3.1 Chemical etching of silicon assisted by graphene oxide in HF-H_2O_2

To simplify the etching condition, only CGO was applied to the assisted etching at first. In this section, all of the GO was CGO. A topographic image of the silicon surface with a GO sheet is shown in Figure 2-1(a), with a cross-sectional profile obtained along the red line shown in the topographic image. A sheet of tens of μm in size with a thickness of ~1.2 nm was imaged, demonstrating that a single layer of GO sheet was loaded on the substrate[47]. The AFM topography of the samples after 1, 4, or 16 hour etching at 25℃ and the corresponding cross-sectional profiles are shown in Figures 2-1(b),(c), and (d).

As shown in Figures 2-1(c) and (d), pores with the shape of GO were formed. Based on the cross-sectional profiles of pores, the depth was about 1.8 nm after 4 hour etching and 18 nm after 16 hour etching, respectively. These results indicate that the GO sheets promote the etching reactions of silicon. However, in the case of 1 hour immersion, Si underneath the GO sheet was not etched and the height of GO area was 3.0 nm, which was approximately 1.8 nm thicker than a pristine GO sheet. This implies that silicon etching under the GO sheet was prevented in the first 1 hour.

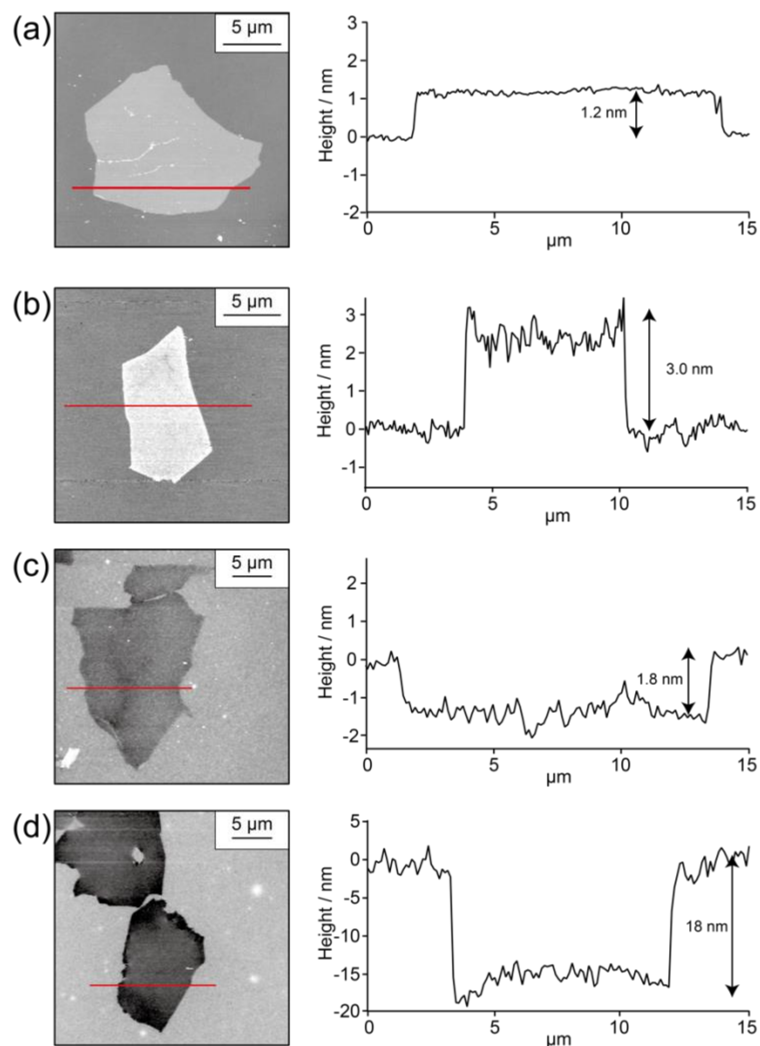

Figure 2-1 AFM topographic images and cross-sectional profiles along the lines of GO-loaded silicon substrate (a) before etching, and after (b) 1, (c) 4, or (d) 16 hours of etching at 25℃, respectively. The etchant concentration was [HF]:[H_2O_2]=15:4.9 (mol L^{-1}).

The etchant composition was optimized to improve the etching rate. Figure 2-2 shows AFM topographic images of GO-loaded silicon substrates after 16 hour etching. With others etching solutions, the etching rate was slower than that in the result of Figure 2-1. Chartier et al. reported that the etching rate is maximum when the etchant molar ratio of HF to H_2O_2 =3:1 in the case of Ag-assisted etching, which approximately fits this result of GO-assisted etching[48]. Furthermore, the GO-coated area was etched faster than not-covered areas when the etchant was composed of only HF. In this case, dissolved oxygen may work as the oxidant for the assisted etching reaction.

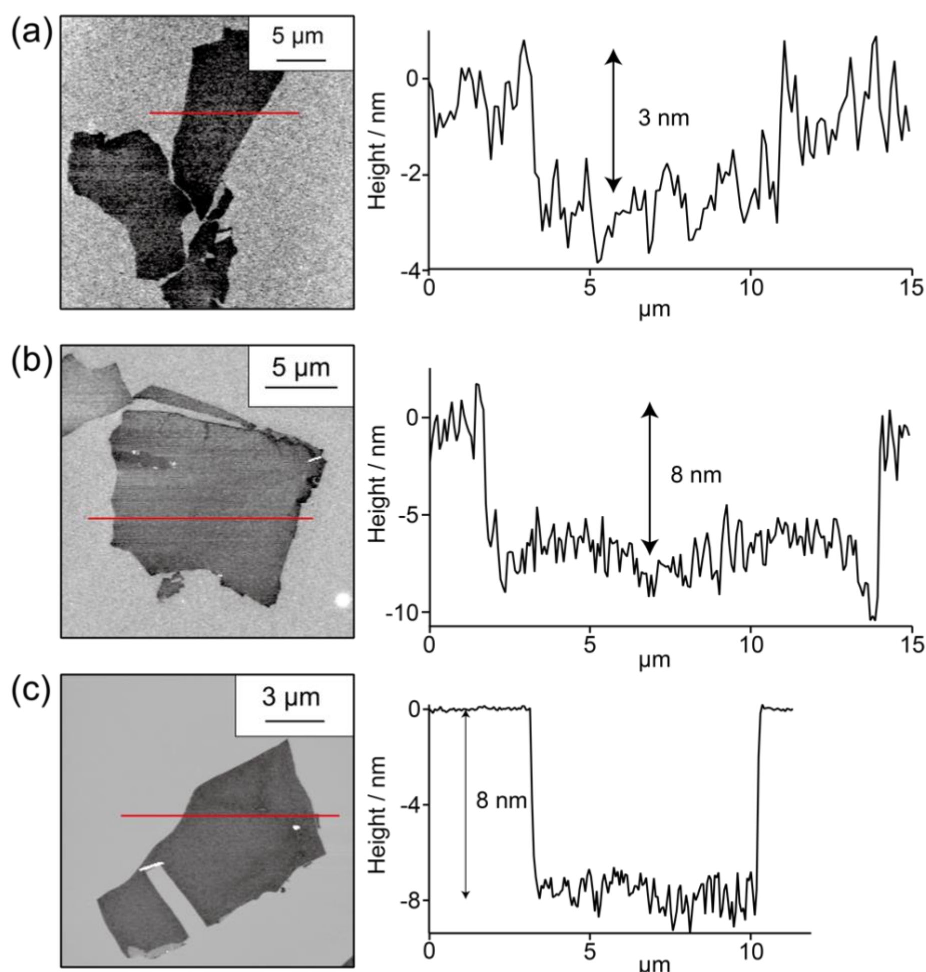

Figure 2-2 AFM topographic images and cross-sectional profiles along the lines of GO-loaded silicon substrate after 16 hour etching. The molar concentration of the etchant was (a) [HF]:[H_2O_2]=7.8:7.3, (b) [HF]:[H_2O_2]=18:3.6, and (c) [HF] =29 (mol L^{-1}).

In the case of metal-assisted silicon etching in HF-H_2O_2 solution, the etching process is often represented by electrochemical and chemical reactions[49,50]. It is widely accepted that H_2O_2 is reduced at the noble metal particles and that electrons are transferred to the silicon substrate through the noble metal particles. Then, silicon is oxidized and dissolved via HF. In the case of GO-assisted Si etching, similar reactions can occur. Many studies reported nanocarbon materials as catalysts for oxygen reduction reaction (ORR) in fuel cell.[51,52]. Furthermore, Song et al. reported that carboxyl-modified graphene oxide possesses peroxidase-like activity, and GO catalyzes the reduction of H_2O_2[30]. Nanocarbon materials have some defects, edges, or heteroatoms (nitrogen, sulfur, oxygen, etc.), and these regions alter the local density of the π-electrons and increase the chemical reactivity.[42,53] In the case of N-doped graphene application to the catalyst for ORR, the oxygen molecule is first adsorbed at the carbon next to the pyridinic nitrogen atom as the initial step of the ORR.[54] There are edges or defects in GO sheets, and these active sites might be related to H_2O_2 reduction reaction and promote the etching reaction.

Of note, large GO sheets are disadvantageous from the viewpoint of the diffusion of the etchant and reaction products. Thus, the etching rate in one GO sheet can be heterogeneous. Actually, the edge area of GO sheet is etched deeper than the center of the sheet. There are two explanations for the high etching rate around edge areas. One is that the edge area has higher catalytic ability than that of the center which some researchers reported. The other is that the basal planes of the sheets are more disadvantageous than the edges of the sheets in terms of the diffusion of the reactants and reaction products. However, there was little difference in the etching rate in the basal planes of one GO sheet. This may be due to the existence of pores in GO sheets. Several studies examined the nanoscale structure of GO using transmission electron microscopy (TEM) or scanning tunneling microscopy (STM)[55,56]. Erickson et al. previously reported that there are some

pores with an average size of 5 nm^2 on GO sheets[55]. During the GO synthesis process, graphite is strongly oxidized by $KMnO_4$, concentrated sulfuric acid, and nitric acid, which causes many defects or pores on GO sheets, and these pores can aid in the diffusion of etchant and reaction products. The geometric and chemical structures of GO may be related to the enhanced etching of silicon.

It may be possible that the oxygen functional groups on GO sheets can oxidize the silicon, which results in enhancing the etching reaction. Furthermore, GO can be damaged and its catalytic properties can deteriorate. XPS analysis of samples was performed to confirm these hypotheses. The XPS C 1s spectra of samples before and after etching are shown in Figure 2-3. Furthermore, C 1s spectra were deconvoluted to 6 peaks, i.e., sp^2 C=C at 284.4 eV, sp^3 C-C at 285.0 eV, C-OH at 286.2 eV, C-O-C at 286.9 eV, C=O at 287.9 eV, and COOH at 289.1 eV[47]. Comparing Figure 2-3(a) with 2-3(b), peaks derived from C-O-C and C-OH significantly decreased after etching for 1 hour. The possible hypothesis is that oxygen functional groups decorated on GO sheets were transferred to hydrogen-terminated silicon (H-Si) and the formed Si-O was removed by HF. In the previous report[57], when GO sheets were spread onto H-Si(111), C=O and C-O-C moieties on GO sheets decreased according to XPS C1s spectra, suggesting that the C-O-Si bond was formed between GO and Si, and oxygen functional groups were eliminated from GO due to the high reactivity of H-Si(111) surface. In addition, there was little difference between the 1 hour and 16 hours etching samples (Figure 2-3(b) and (c)), suggesting that the GO sheets were not altered during the enhanced etching stage. This indicates that reduced GO sheets have the potential to enhance the etching reaction.

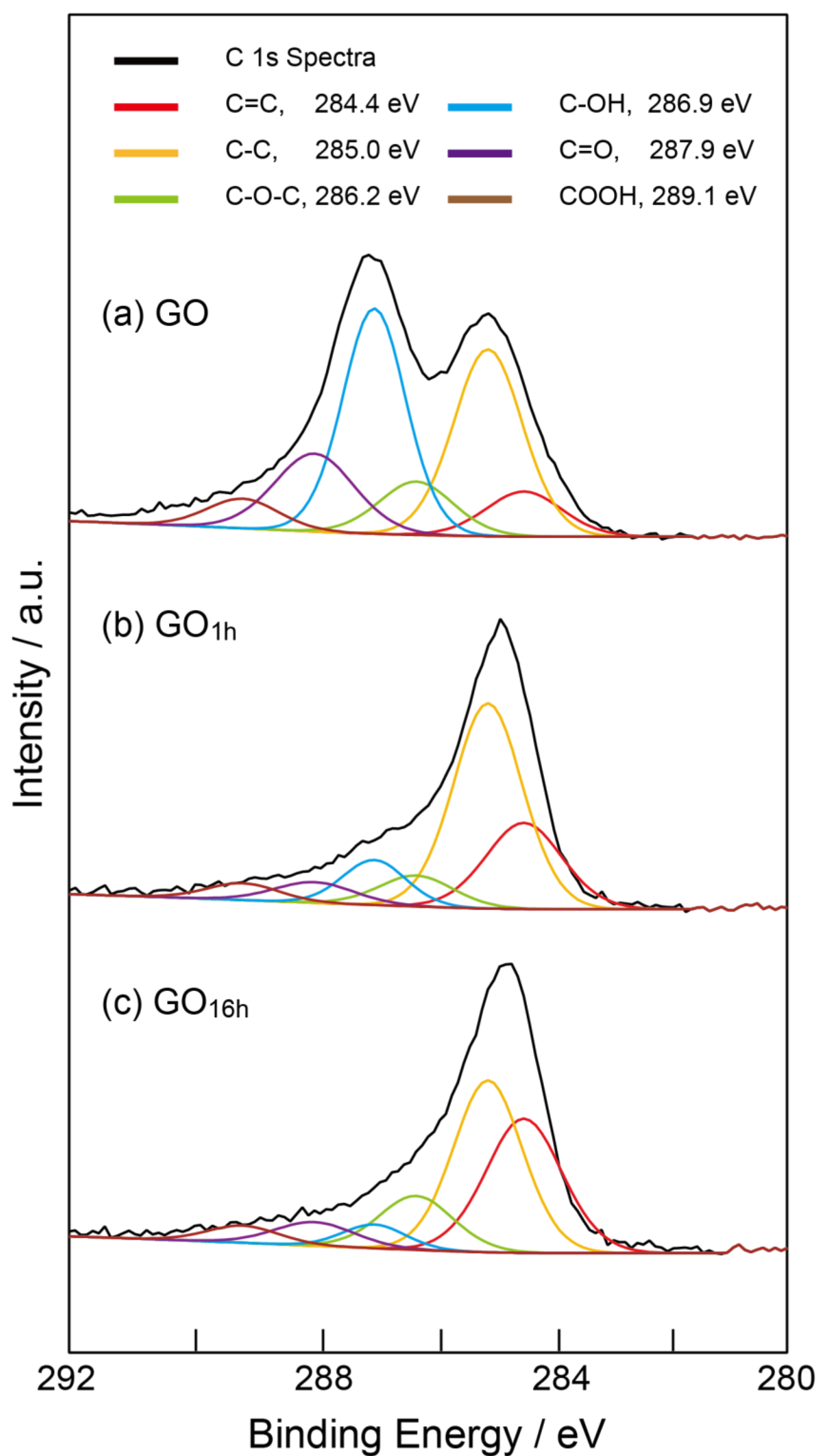

Figure 2-3 XPS C 1s spectra of samples (a) before and after (b) 1 hour or (c) 16 hours of etching. The spectra were calibrated to the Si 2p peak at 99.8 eV. Each spectrum was deconvoluted to six peaks as shown in the figure.

2.3.2 Chemical etching of silicon assisted by graphene oxide in HF-HNO_3

In this section, only CGO was applied for the catalyst of assisted etching. The etching of GO-coated silicon substrates under different etchant compositions was carried out to evaluate the catalytic activity of GO towards the etching reaction. Figure 2-4 shows the surface morphology and the cross-sectional profiles of the silicon substrate after the etching process observed by 3D laser microscopy. The etching temperature was kept at 25°C. When the concentration of the HNO_3 was high (the molar concentration of HF to HNO_3 was 1.5:15 (mol L^{-1})), the area covered by GO sheets was around 100 nm higher than the bare parts (Figure 2-4(a)). This result means that GO sheets prevent the etching reaction in the HNO_3-rich etchant. On the other hand, when the GO-coated substrate was immersed in the etchant of which the concentration of HF to HNO_3 was 29: 3.2×10^{-2} (mol L^{-1}) (30 mL HF and 60 μL HNO_3), a lot of circular pores were formed under GO sheets, as shown in Figure 2-4(b). However, the etched surface was not homogeneous, and the morphology was heavily roughened. This etchant condition is not suited for practical application. This result may be because the gases produced in the etching process stuck on the backside of GO sheets and prevented the diffusion of the reactants. Next, the concentration of HNO_3 was decreased to restrict produced gases. Figures 2-4(c) and (d) show the samples after etching for 4 and 16 minutes each in the etchant of which the concentration of HF to HNO_3 was 29:5.3×10^{-3} (mol L^{-1}) (30 mL HF and 10 μL HNO_3). In this etchant condition, the GO-sheet-like pores were formed on the substrate surface, and the etching depth was almost proportional to the etching time despite of the slower etching rate compared with that of Figure 2-4(b). This result means that GO sheets promoted the etching reaction by utilizing the optimized etchant.

The silicon etching reaction in HF-HNO_3 etchant is frequently described by a series of HNO_3 reduction, silicon oxidation, and dissolution[58–62]. The reaction equations are as

follows,

Silicon oxidation

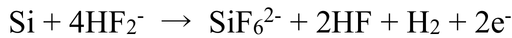

$$Si + 4HF_2^- \rightarrow SiF_6^{2-} + 2HF + H_2 + 2e^-$$

HNO_3 reduction

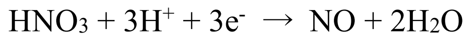

$$HNO_3 + 3H^+ + 3e^- \rightarrow NO + 2H_2O$$

It has been generally known that the etching of silicon in HF-HNO_3 system is isotropic because the etching reaction is so fast that the diffusion of the reactants or products restricted the etching reaction. However, the etching behavior can be reaction-limited by reducing the concentration of HF or HNO_3. In this situation, the concentration of HF and HNO_3 changes the rate-determining step in this etching process. In the high HNO_3 compositions, HF diffusion and silicon dissolution should determine the etching rate[60]. On the other hand, when the HF concentration of the etchant is high, HNO_3 diffusion or its reduction reaction should restrict the etching reaction[62]. Based on this tendency, it would be concluded that GO sheets work as the mask in HNO_3-rich etchant because the GO prevents the rate-limited step, that is, the diffusion of HF_2^- or SiF_6^{2-} around the silicon under the GO. Furthermore, GO sheets enhance the etching reaction in HF-rich conditions since GO sheets assist the HNO_3 reduction reaction, which can be the rate-determining step in HF-rich etchant. The higher etching rate in the HF-rich HF-HNO_3 solution with higher HNO_3 solution also supports that the HNO_3 reduction restricts the whole etching reaction in the HF-rich HF-HNO_3 solution, comparing the result of Figures 2-4(b) and (d).

In HF-HNO_3 system, GO can be oxidized and damaged by the HNO_3. The chemical condition of GO before and after the etching process is essential to confirm whether GO sheets are damaged or not. Figure 2-5 shows the XPS C 1s spectra of GO before and after etching. Although a peak around 287 eV derived from oxygen functional groups was detected on the GO sheets before etching (Figure 2-5(a)), this peak disappeared after 4

minute etching also in HF-HNO_3 solution. Furthermore, there was little difference between the spectrum after etching for 4 minutes and 16 minutes, shown in Figures 2-5(c) and (d). These results prove that the catalytic ability of GO has not deteriorated during the etching process. The etching rate in HF-HNO_3 solution was higher than that in HF-H_2O_2 solution. There are two possible mechanisms to explain this etching rate difference. One is that the dissolution rate of silicon in each solution affects the etching rate under GO sheets. It is well-known that HF-HNO_3 solution can dissolve silicon faster than that of HF-H_2O_2. The other is the difference in GO catalytic activity towards each oxidant reduction reaction although the detailed mechanism is still unclear.

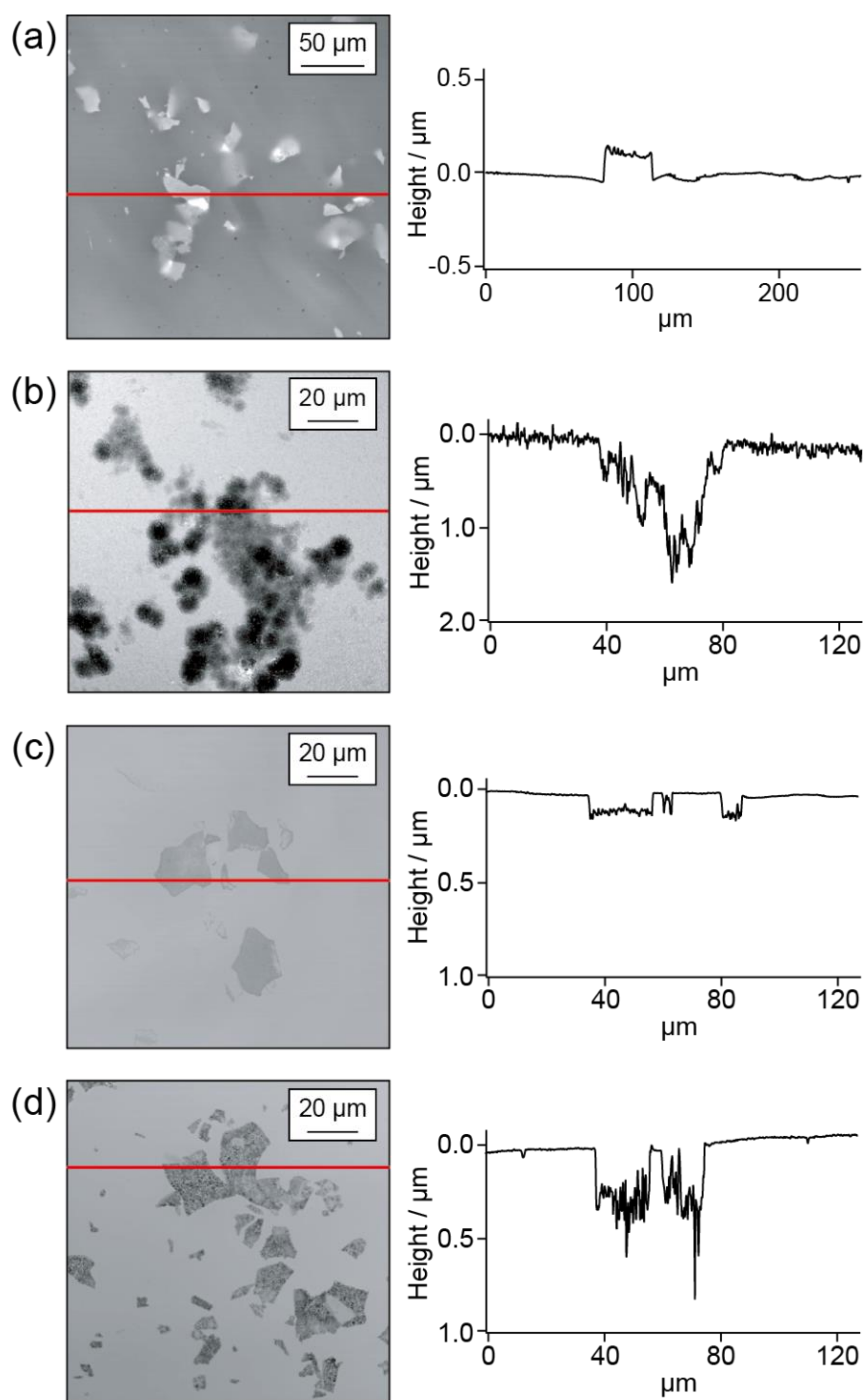

Figure 2-4 3D laser microscope topographic images and cross-sectional profiles along the lines of silicon substrate loaded with GO sheets after etching at 25 °C. The etchant concentration of [HF]:[HNO_3] was (a) 1.5:15 (mol L^{-1}), (b) 29:3.2×10^{-2} (mol L^{-1}), and (c, d) 29:5.3×10^{-3} (mol L^{-1}). The etching time was (a, b, d) 16 minutes and (c) 4 minutes.

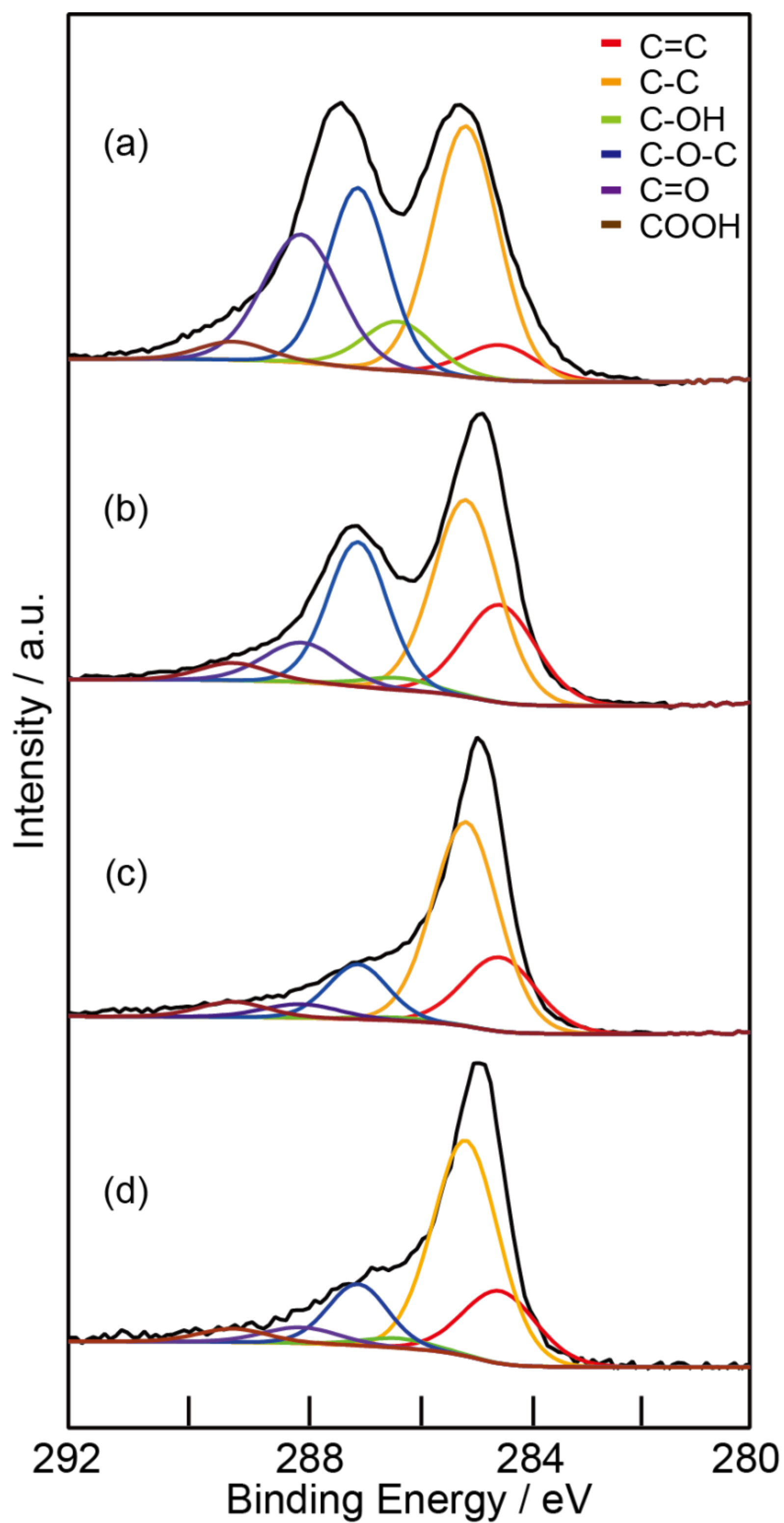

Figure 2-5 XPS C 1s spectra of silicon substrates loaded with CGO sheets (a) before etching and after etching for (b) 1 minute, (c) 4 minutes, and (d) 16 minutes.

2.4 Reaction kinetics of GO-assisted silicon etching in HF-HNO_3 solution

The previous section implied that GO sheets promoted the HNO_3 reduction reaction, which caused the enhancement of the silicon etching reaction under GO sheets. For elucidating the mechanism of the GO-assisted etching reaction, the temperature dependence of the etching rate was evaluated using Arrhenius equation[63],

$$k = A\exp\left(-\frac{E_a}{k_B T}\right)$$

where k, k_B, and T represent the reaction rate, Boltzmann constant, and temperature, respectively. E_a is the activation energy and A is the pre-exponential factor which is generally interpreted as the parameter depending on the collision frequency of the reactants.

Figure 2-7 shows the temperature dependence of the etching rate on the GO-covered parts and the bare silicon parts. The etchant concentration was the same as in Figure 2-4(c), and the etching time was 4 min. The etching rate of bare silicon was calculated by measuring the weight change of a 2×2 cm^2 silicon substrate in an etching process,

$$v = \frac{\Delta w}{\rho \times S} \times \frac{1}{t} \times \frac{3}{5}$$

where v is the etching rate (cm min^{-1}), Δw is the weight change of the substrate in the etching process (g), ρ is the silicon density (2.33 g cm^{-3}), S is the area of the substrate (4 cm^2), and t is the etching time (4 minutes). The etching rate should be calculated with the consideration of the fact that the etchant dissolved both sides of the substrate. The etching ratio for one side was calculated by floating the substrate on the etchant. The ratio of the etching rate of the polished-side to the backside was 3:2. Then, in order to compare the bare silicon areas with the GO-covered area, the etching rate of the bare substrate was

estimated to be 60% of the total because the GO sheets were loaded on the polished side of the silicon wafer. However, the total etching depth on the polished-side and backside was larger than the etching depth of the substrate, which was fully immersed in the etchant. This may be because HF vapor can etch silicon surfaces that are not in direct contact with the etchant[23]. A factor of 3/5 was used in the etching rate equation based on this experimental result.

First, the etching rate increased as the etchant temperature increased for both systems. If the diffusion of the etchant limited the etching reaction, the etching rate does not depend on the etchant temperature apparently. This result indicates that the etching reaction in this system was reaction-limited. Next, the activation energy(E_a) on the bare silicon part was estimated to be 0.39±0.04 eV and that on GO was estimated to be 0.45±0.06 eV, respectively. Both E_a values agree with the previous report of silicon etching in the mixture of HF-HNO_3[63] and there was little difference in their activation energy. On the other hand, the intercept of this Arrhenius plot, which was correlated to the pre-exponential factor (A) on GO parts, was around ten times larger than that on the bare silicon part.

As discussed in the previous section, the etching of silicon in HF-HNO_3 solution is caused by HNO_3 reduction and silicon oxidation, and the HNO_3 reduction should be enhanced on the surface of GO sheets. Many researchers reported the mechanism of HNO_3 reduction and explored the effective catalyts[64,65]. Groot et al. reported the detailed process of HNO_3 reduction on platinum electrode[64]. At low HNO_3 concentration, the HNO_3 reduction proceeds through a series of reactions as follows,

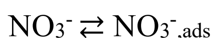

$NO_3^- \rightleftarrows NO_{3,ads}^-$

$NO_{3,ads}^- + 2H^+ + 2e^- \rightarrow NO_{2,ads}^- + H_2O$

$NO_{2,ads}^- + 2H^+ + e^- \rightarrow NO_{ads} + H_2O$

In this process, the reduction of nitrate to nitrite is considered to be the rate-determining step. Furthermore, the amount of the adsorbed nitrate also controls the reaction rate at low concentrations of nitrate. GO is also an effective catalyst for the oxidant reduction reaction, such as O_2[66], H_2O_2[30,67], and HNO_3[32]. When GO or other nano-carbon materials are utilized as catalysts, intrinsic defects, edges, or heteroatoms on those materials are supposed to play a central role in the catalytic activity[42]. These regions alter the charge or spin distribution of π electrons, enabling those oxidants to adsorb easily and increase chemical reactivity. This result implies that defect sites on GO sheets work as adsorption sites for nitrate and they serve as the catalytic active sites.

In the GO-assisted etching of silicon, the pre-exponential factors between silicon parts and GO parts were different, whereas their activation energy was within the variation in the measurement. These results imply that each nitrate reduction reaction path on GO sheets and bare silicon is not different. The difference in the etching rate is due to the amount of the adsorbed reactive intermediates on each surface, shown in Figure 2-6.

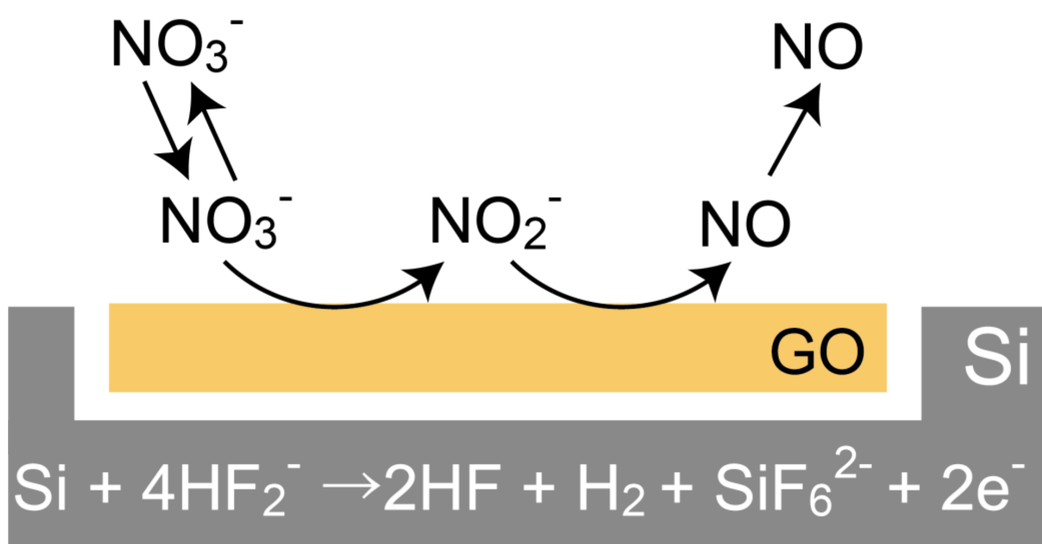

Figure 2-6 A schematic illustration of GO-assisted silicon etching in HF-HNO_3.

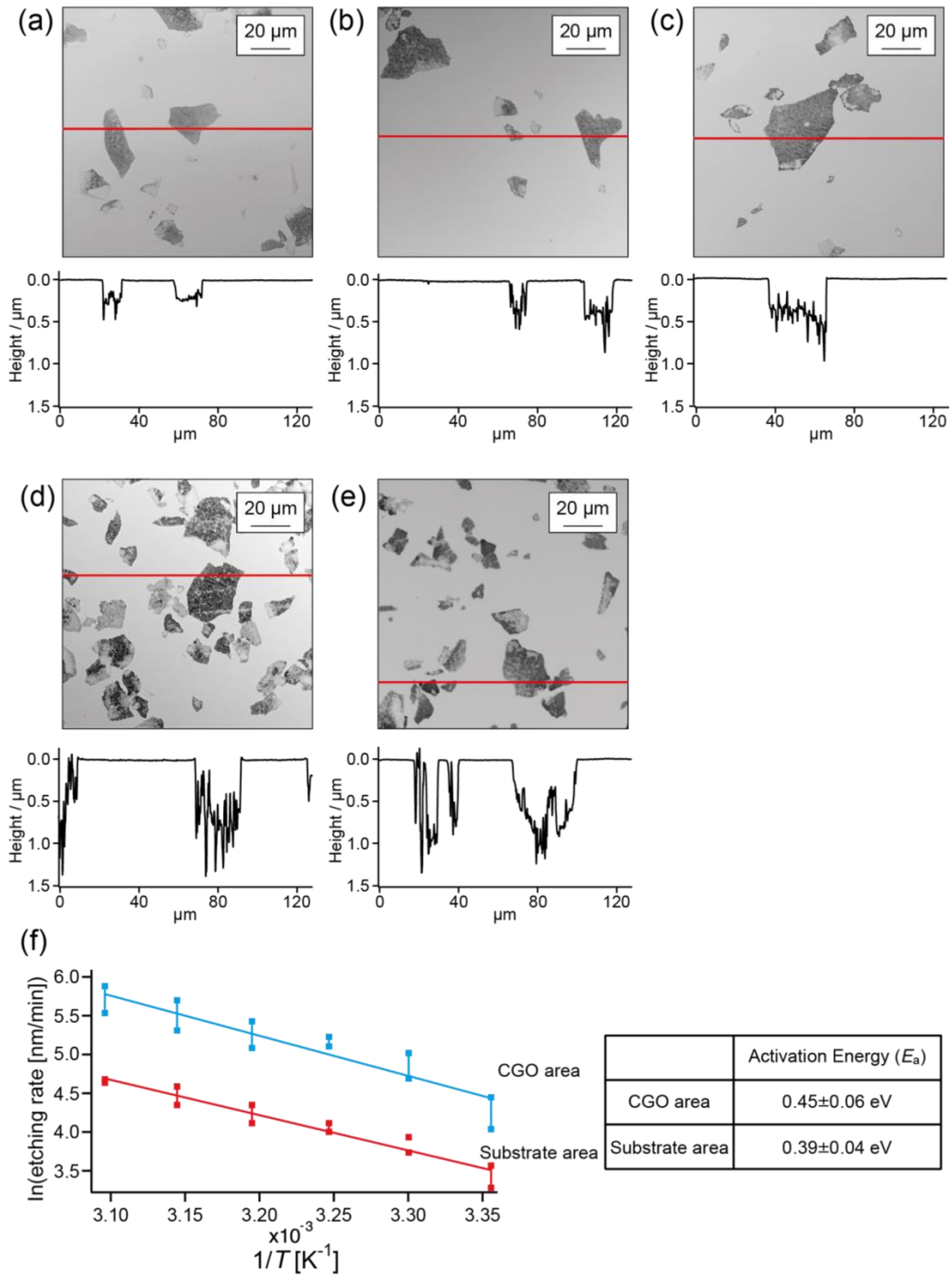

	Activation Energy (E_a)
CGO area	0.45±0.06 eV
Substrate area	0.39±0.04 eV

Fig. 2-7 3D laser microscope topographic images and cross-sectional profiles along the lines of a silicon substrate loaded with CGO sheets, after 4 min etching. The etchant concentration of [HF]:[HNO_3]=29:5.3×10^{-3} (mol L^{-1}). Etchant temperature at (a) 30°C, (b) 35°C, (c) 40°C, (d) 45°C, and (e) 50°C. (f) Arrhenius plot of the etching rate under CGO sheets and bare areas of silicon.

2.5 Catalytic mechanism of GO-assisted silicon etching

In the previous section, the catalytic mechanism of GO-assisted etching was proposed. Because heteroatoms do not decorate GO sheets utilized in these experiments, defects on GO sheets are supposed to work as active sites towards nitrate reduction. The relationship between the catalytic ability and the number of defects on GO sheets was demonstrated to prove this hypothesis. Then, two types of GO with different defects density are utilized as the catalyst for the silicon etching reaction.

Figure 2-8 shows the chemical and structural analysis of both GO. To simplify the effects of their sheet size, CGO was fractured by sonication for 2 hours so that it had a similar size as EGO. Typical AFM topographic images of the silicon sample coated with crushed CGO and EGO before etching are shown in Figures 2-8(a) and (b). The sizes of both GO sheets were approximately 5 μm and they had a thickness of about 1 nm, indicating monolayer sheets. Chemical and structural analyses were conducted by XPS and μRS. Figures 2-8(c) and (d) show the XPS spectra for both types of GO, from which it was ascertained that the main oxygen functional group on CGO was epoxide, while hydroxyl was the main group on EGO. Figures 2-8(e) and (f) show Raman spectra of both types of GO. Two peaks were focused: D peak at around 1300 cm^{-1} and G peak at around 1600 cm^{-1}. D peak derives from the breathing mode of six-atom rings, which is affected by defects in the graphitic structure. G peak derives from the graphitic lattice. Comparing the spectra of both types of GO, there are slight differences in both spectra. D peak of EGO is sharper than that of CGO, and the G peak position of EGO is red-shifted compared with that of CGO, which was reported in a previous paper[68]. Generally, when the defects in a GO sheet are repaired, all of the peaks become sharp, G peak increases, and D peak decreases. However, it was reported that the intensity of the D peak decreases when the defect density of GO increases and the distance between defects decreases to less than 5

nm[68]. These results suggest that EGO sheets have a more ordered structure than CGO sheets. Further analyses of both GO sheets and their electrical conductivity is discussed in the Appendix.

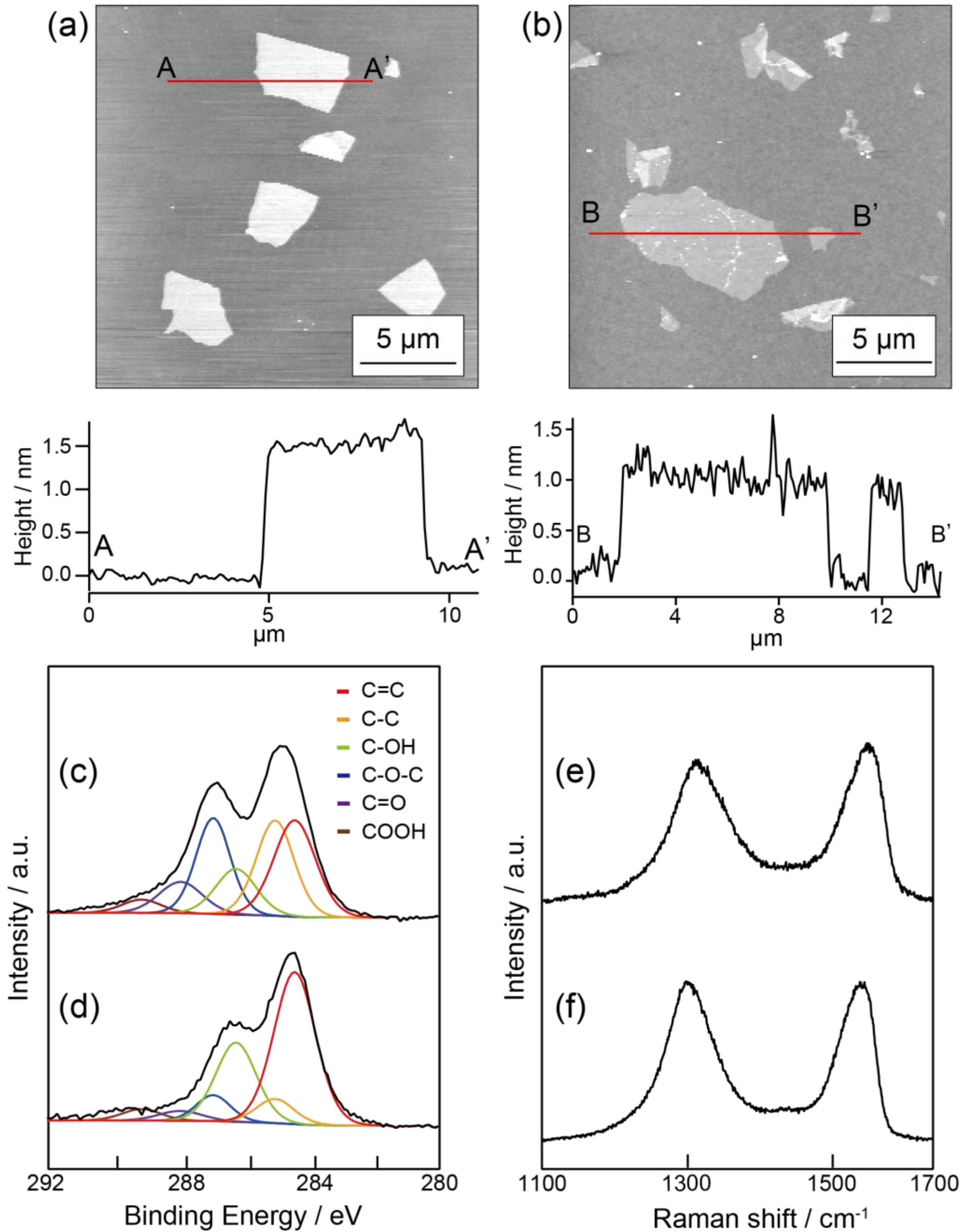

Figure 2-8 Comparison of chemical and structural characteristics of both types of GO sheet. AFM topography and line profiles along lines of (a) CGO and (b) EGO, XPS C1s spectra of (c) CGO and (d) EGO, and Raman spectra of (e) CGO and (f) EGO.

Figure 2-9 shows 3D laser microscope topographic images and cross-sectional SEM images of the silicon loaded with crushed CGO and EGO, respectively. Both the samples were etched for 16 min. First, holes in the shape of crushed CGO sheets were formed on the substrate after etching and these depths were around 400 nm (Figure 2-9(a)). This etching rate was the same as a result of not-crushed GO, suggesting that the mass transport of the reactants or products is enough so that the sheet size has little influence on the etching rate. It was reported that a lot of pores with a size of 5 nm^2 were formed on CGO sheets in the synthesis process[55]. Thus, it would be possible that the reactants or products are transferred from the side of the sheets and these pores, and their diffusion does not restrict the etching rate. Next, the etching rate of EGO was slower than that of CGO, as shown in Figures 2-9(a) and (b), which illustrates that the catalytic activity of EGO is inferior to that of CGO. In general, EGO has fewer defects than CGO because EGO is synthesized by a moderate graphite oxidation process[44]. Strong oxidant such as $KMnO_4$ and nitric acid is utilized to oxidize the graphite in the synthesis process of GO which is known as Hummers' method. On the other hand, EGO is synthesized by graphite anodization without a strong oxidant, which causes less damage to the graphitic structure of EGO sheets. Combining the etching results and the structural analyses of both GO, defects on GO sheets play an essential role in enhancing the etching reaction.

In the nitrate reduction process, the adsorbed nitrate on a specific surface is one of the most critical factors for the reaction rate[64]. The relationship between the adsorption energy of reactants and their catalytic activity on various types of alloy materials was reported. The more the adsorption energy of nitrate ions on a certain alloy surface is, the more active the alloy material is[69,70]. Furthermore, several researchers reported the catalytic activities of nano-carbon materials towards various types of oxidant reduction reactions in terms of both experiments and calculation and pointed out that it is more

stable for the reactants to be adsorbed on the inhomogeneous parts, such as defects, heteroatoms, or edge parts, than on the homogeneous part[32,71]. At this time, the main inhomogeneous parts on GO were its defects. In GO-assisted etching, structural defects on GO can work as the central sites of nitrate reduction, enhancing the etching reaction, shown in Figure 2-10.

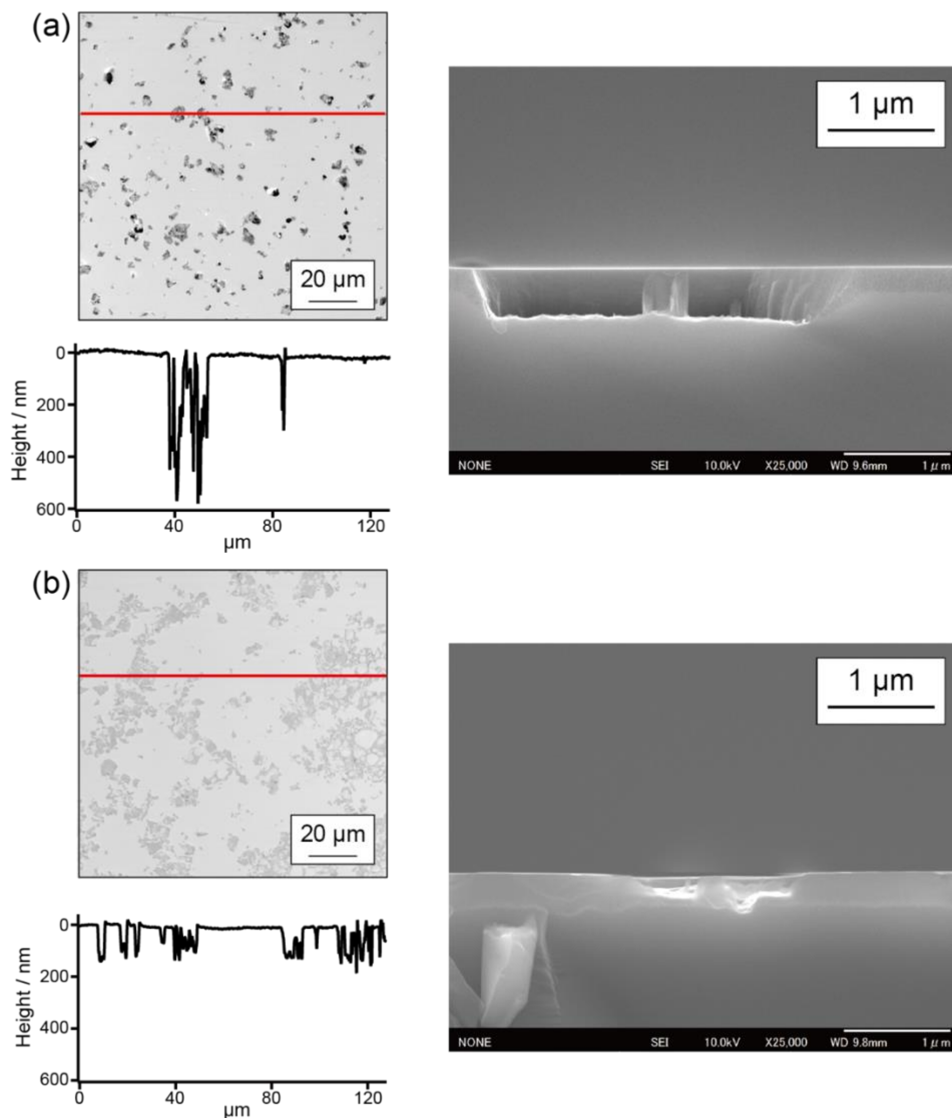

Fig. 2-9 3D laser microscope topographic images, cross-sectional profiles along lines, and cross-sectional SEM images of silicon substrate loaded with two types of GO sheets after 16 minute etching. The deposited GO sheets were synthesized by (a) modified Hummers' method (CGO) and (b) electrochemical exfoliation (EGO).

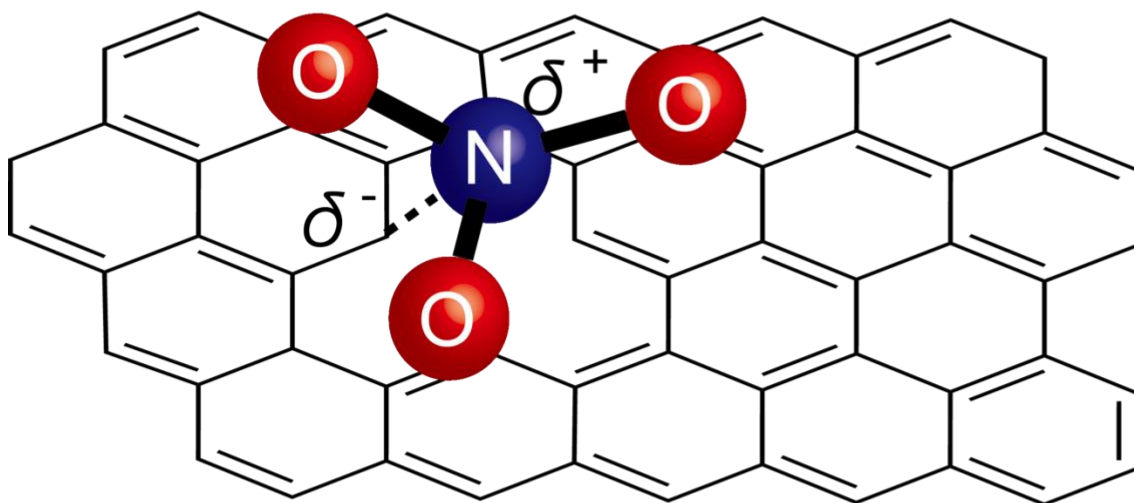

Figure 2-10 A schematic illustration of GO-assisted silicon etching in HF-HNO_3 solution.

2.6 Conclusion

In this chapter, the selective etching process of silicon substrates was conducted by applying GO sheets as a catalyst for the silicon wet etching reaction. GO enhances the silicon etching reaction, especially the oxidant reduction reaction, in an optimized solution, and the etching rate under GO was faster in HF-HNO_3 than that in HF-H_2O_2. Furthermore, kinetic analyses were performed for a deeper understanding of this process. By measuring the temperature dependence of the etching rate, the activation energies of the etching reaction on both the silicon surface and under the GO sheets were calculated and were found to be almost the same, although their pre-exponential factors were different. From this difference, the mechanism of GO-assisted etching was determined. GO sheets function as adsorption sites for the nitrate, thereby increasing the reaction frequency relative to the bare silicon areas.

Furthermore, the origin of the catalytic activity of GO was ascertained by applying two types of GO with different defect densities. GO sheets with more defects were shown to have higher catalytic activities for the etching reaction, suggesting that the reactants are more likely to be adsorbed on the defects of GO sheets. This discovery may be helpful for catalytic research of other nano-carbon materials.

Chapter 3 Vapor phase chemical etching of silicon assisted by graphene oxide

3.1 Introduction

In the previous section, it was revealed that GO enhances the silicon etching reaction in the liquid phase and the etching rate was improved by utilizing the optimized etching solution. However, two obstacles appeared for the practical application of GO-assisted silicon etching in the solution process shown in Figure 3-1.

1. The pealing of GO sheets due to the produced gases during the etching process.
2. Porous structure formation on the surface of silicon.

To resolve the obstacles of assisted etching in the solution process, Hildreth developed a novel assisted etching process with a vapor phase to overcome the premise of the utilization of an etching solution[72]. In vapor phase etching, any gaseous products are rapidly removed from the silicon surface and bubbles do not form between catalysts and the silicon surface during the etching process, thereby preventing the peeling of catalysts. Furthermore, vapor phase etching did not generate a porous layer; however, the underlying mechanism remains unclear.

In this section, the chemical etching of silicon assisted by GO sheets with a vapor phase process was demonstrated. To the best of my knowledge, one research group applied carbon materials to the assisted etching of silicon in a vapor phase[23]. Although their findings proved that carbon particles enhanced the etching reaction, the etching direction was not strictly controlled, and carbon particles etched the silicon in random directions. This may have been due to the applied graphite particles being in contact with the silicon surface in a multi-plane and etching proceeding in all contact directions. This behavior is sometimes observed in the Mac Etch process[73]. GO was proposed as a solution to the

issue of random etching directions. GO is a two-dimensional material with a thickness of ~ 1 nm, and GO sheets are in contact with silicon in one direction when they are loaded on the silicon surface, which results in a vertical etching direction of GO-assisted etching.

Moreover, the control of etching areas with a combination of GO micro-contact printing (μCP) was attempted[74,75]. μCP is a bottom-up method to build ordered structures with a micro-nano scale[76]. In the μCP process, after precursors are attached to the polymer substrate with a minute relief, referred to as a 'stamp', the 'stamp' is pressed to the substrate to transfer the precursors. μCP is suitable for the rapid fabrication of uniform minute structures on a large scale. By combining the μCP of GO with silicon etching in a vapor phase, the formation of μm-sized pores in the desired areas was attempted.

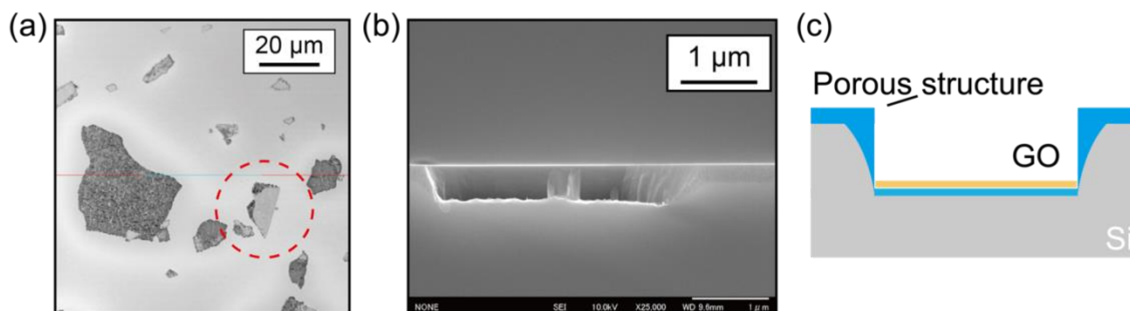

Figure 3-1 (a) A surface topography, (b) a cross-sectional image, and (c) a schematic illustration of silicon after GO-assisted etching in the solution process.

3.2 Experimental procedure

3.2.1 Vapor phase GO-assisted silicon etching

GO was synthesized using a modified Hummers' method described in the previous section[43]. To confirm whether GO enhanced the etching reaction in the vapor phase, the silicon substrate on which GO sheets were randomly loaded was prepared as the etching sample. A single-side polished p-type silicon ((100), 1–10 Ω cm, boron-doped, Electronics and Materials Corp.) substrate was cleaned by sonication in acetone, ethanol,

and ultrapure water in succession. The substrate was then subjected to a treatment with a Xe excimer lamp (wavelength: 172 nm, 10 mW cm^{-2}, Ushio Inc.) to remove organic contamination. GO sheets were then loaded on the substrate by spin-coating GO dispersion in water (500 rpm for 15 s and 2000 rpm for 150 s). Figure 3-2 shows a schematic illustration of the vapor phase GO-assisted etching of silicon. The GO-loaded silicon substrate and a PFA beaker with an etching solution were sealed in a large PFA container. The container was heated in an electric furnace so that the etching solution became a vapor source for etching substrates at the desired temperature. The etching solution was a mixture of HF (50 wt%, for the semiconductor industry, Morita Chemical Industry Corp.) and H_2O_2 (30 wt%, analytical grade, Fuji Film Wako Pure Chemical Corp.) or HNO_3 (70 wt%, for the electrical industry, Fuji Film Wako Pure Chemical Corp.) and its volume was 5 mL. The surface structure of the sample obtained was observed by 3D laser microscopy and SEM. The chemical condition of the sample was analyzed by XPS. Detailed information on these apparatuses is described in the previous section.

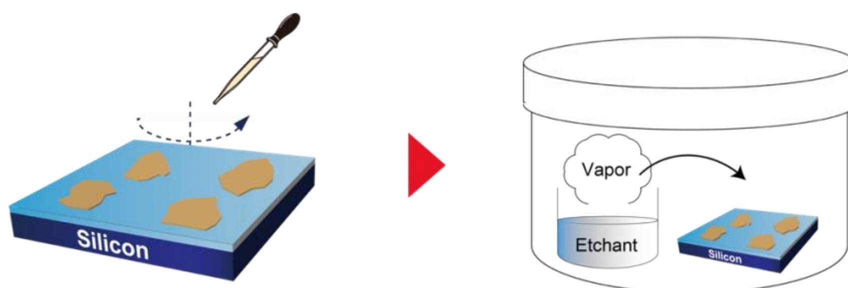

Figure 3-2 A schematic illustration of the vapor phase GO-assisted etching of silicon.

3.2.2 Micro-contact printing of GO

Circle-patterned GO was transferred onto a silicon substrate by µCP (Figure 3-3(a)-(c)), which was partially based on previous studies[77,78]. In this method, patterned convex silica was formed on a smooth polymer substrate, which was used as the 'stamp'. A

cycloolefin polymer (COP) substrate (ZF16-188, ZeonorFilm, Zeon Corp.) was cut into 2×2 cm^2 as a stamp substrate. The COP substrate was then irradiated with a Xe excimer lamp for 10 min in 10^3 Pa dry air via a circle-patterned photomask to form patterned circle hydrophilic areas with a diameter of 5 μm. The irradiated COP substrate was then sealed in the PFA container with a mixture of 10 mL ethanol (99.5%, Nacalai Tesque) and 5 mL 2,4,6,8-tetramethylcyclotetrasiloxane (TMCTS, 99%, Alfa Aesar) and heated at 80°C for 24 hours. TMCTS molecules were only deposited on the hydrophilic areas of the COP substrate. The COP substrate was then irradiated with a Xe excimer lamp for 50 minutes under 10^3 Pa to change the deposited TMCTS into silica (SiOx) and etch the non-covered areas to form convex structures. This stamp was then loaded with GO with a sheet size of ca. 500 nm by spin-coating GO dispersion. GO loaded on the COP stamp was pushed against a cleaned silicon substrate with a load of 400 N for 1 hour to transfer the GO circle pattern on the silicon substrate. The silicon substrate was exposed to the vapor etchant as described in the previous section. The surface structure of the sample was observed by SEM and AFM and its chemical condition was analyzed by XPS and μRS.

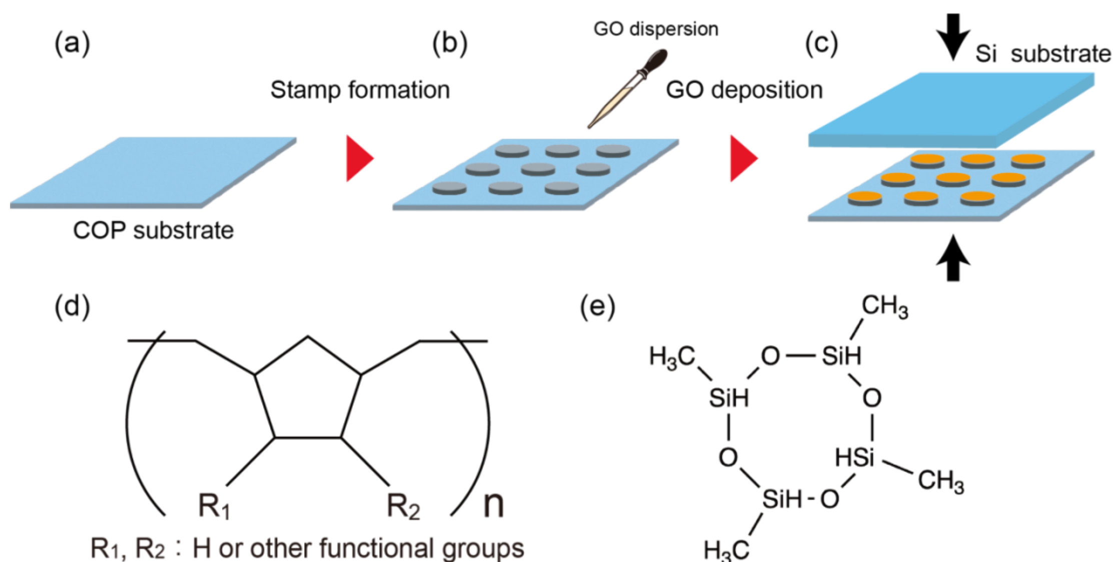

Figure 3-3 (a)-(c) A schematic illustration of μCP. (d),(e) Chemical structures of (d) COP and (e) TMCTS.

3.3 Etching behavior with various types of etching compositions

Figure 3-4 shows surface and cross-sectional SEM images of silicon substrates loaded with GO after vapor phase etching for 2 hours with various compositions of etching solutions as the vapor source. In vapor phase etching, the temperature of the etching solution was kept at 50°C. In each etchant composition, GO sheet-like pores formed on the silicon substrate, which indicated that GO enhanced the etching reaction in the vapor phase. Although the silicon under GO sheets was etched deeper with higher oxidant concentration conditions, the surface is also rougher in higher oxidant concentrations. When the silicon substrate was exposed to HF-rich HF-HNO_3 vapor (Figure 3-4(a)), a nanoscale porous structural layer formed around GO sheets. In addition, such a porous structure also formed on all of the areas not covered with GO in the case of HNO_3-rich HF-HNO_3 vapor (Figure 3-4(b)) or H_2O_2-rich HF-H_2O_2 vapor (Figure 3-4(d)). The formation of these porous structures was not suitable for silicon processing. On the other hand, as shown in Figure 3-4(c), a smooth morphology was obtained both inside and outside of the GO-covered region, indicating that an obvious porous structure was not formed after vapor phase etching in the HF-rich HF-H_2O_2 system. Figure 3-5 shows surface topographic images of samples after vapor phase etching with each etchant composition. When the GO-loaded silicon substrate was exposed to vapor from an HF solution (Figure 3-5(a)), GO-covered areas were etched deeper than non-covered areas. However, the etching rate was slower than etched samples with a mixture of HF and oxidants. Furthermore, etching results with other etchant concentrations were shown in Figures 3-5(b)-(e), which resulted in non-uniform etching or the roughening of GO areas or substrate areas.

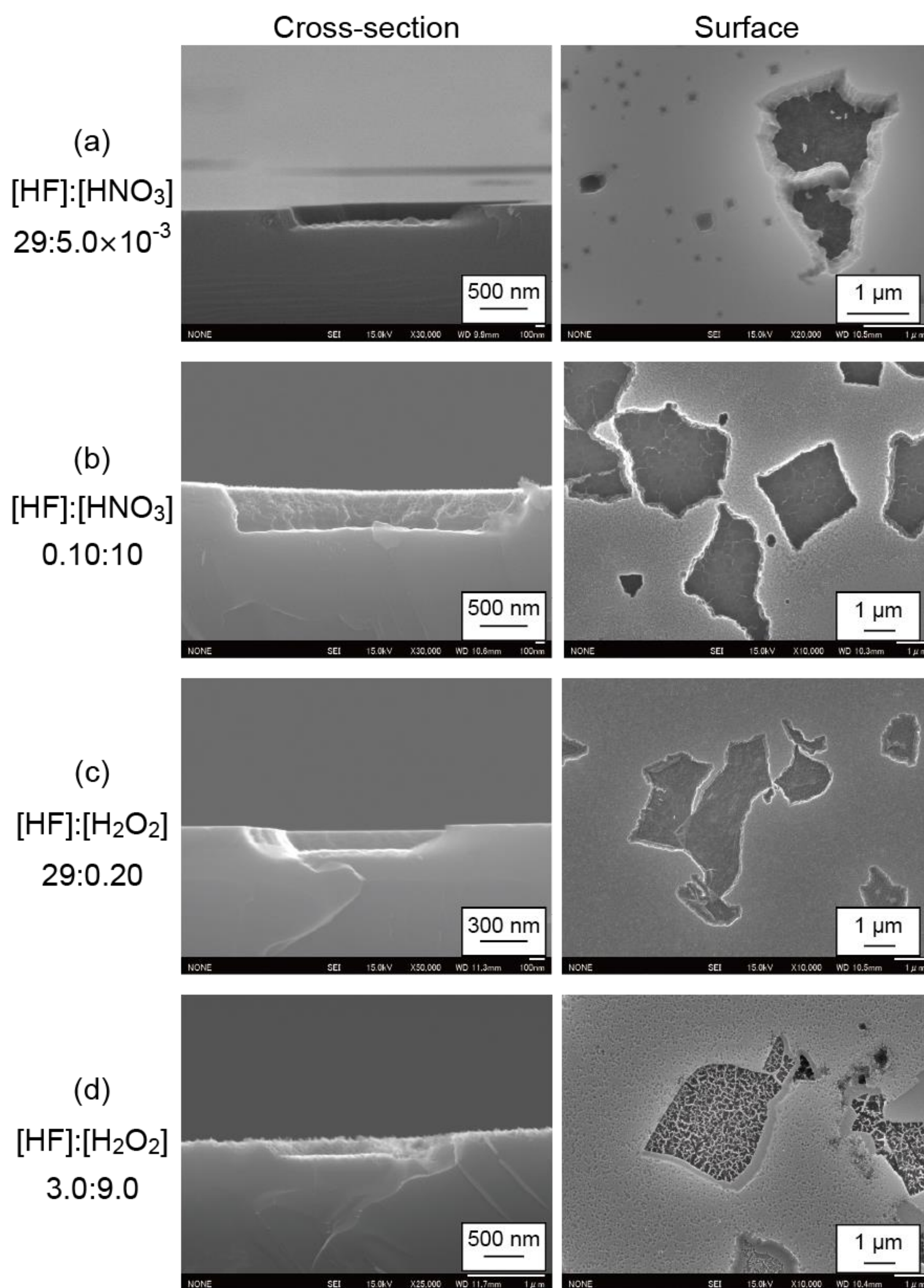

Figure 3-4 Cross-section and surface SEM images of GO-coated silicon substrates after vapor phase etching at 50℃ for 2 hours. The molar concentrations of etching solutions were (a) $[HF]:[HNO_3]=29:5.0\times10^{-3}$, (b) $[HF]:[HNO_3]=0.10:10$, (c) $[HF]:[H_2O_2]=29:0.20$, and (d) $[HF]:[H_2O_2]=3.0:9.0$ (mol L^{-1}).

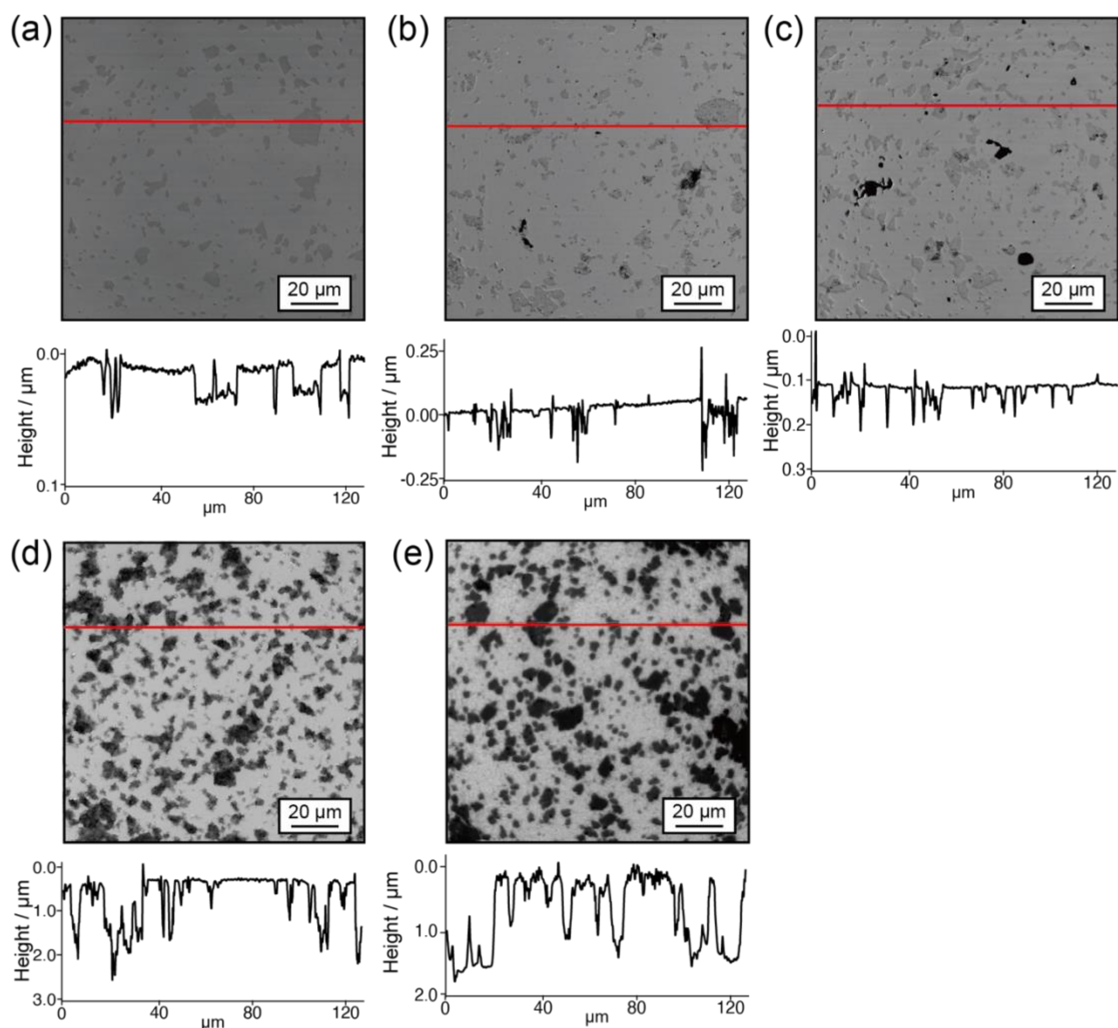

Figure 3-5 3D laser microscope topographic images and cross-sectional profiles along lines of silicon substrates loaded with GO sheets after vapor phase etching at 50°C for 1 hour. The molar concentration of the etching solutions were (a) [HF]=29, (b) [HF]:[H_2O_2]=26:1.0, (c) [HF]:[H_2O_2]=0.60:2.0, (d) [HF]:[HNO_3]=2.6:1.6, and (e) [HF]:[HNO_3]=0.29:12 (mol L^{-1}).

The composition of the etching solution in GO-assisted silicon etching in the vapor phase was optimized and it was revealed that the HF-rich HF-H_2O_2 solution was suitable for the micro-nano processing of silicon. Then, the relationship between the etching depth and etching time was evaluated to confirm the deterioration of GO sheets during the

etching process. Figure 3-6 shows surface topographic images of samples after vapor phase etching for each etching time. The etching depth under each GO sheet is sometimes a little different which may be due to the size difference of each GO sheet described later. The error bar contains the etching results of GO with a sheet size larger than 5 μm. The etching depth was approximately proportional to the etching time (ca. 60 nm h^{-1}) until 16 hours of etching. This result indicates that GO sheets did not deteriorate in the etching reaction timescale. The chemical conditions of GO sheets before and after etching were also analyzed by XPS, as shown in Figure 3-7. Oxygen moieties on GO sheets were removed at the beginning of the etching process. This behavior was consistent with the findings described in the previous chapter[79,80], and indicates that a strong oxidant, H_2O_2 or HNO_3, in the vapor etchant did not oxidize GO sheets, but was consumed in the etching reaction.

It was confirmed that the etching depth under each GO sheet was sometimes a little different. Therefore, the relation between GO size and etching depth was confirmed, as shown in Figure 3-8. The etching condition was 50℃ for 2 hours with the etching solution of [HF]:[H_2O_2]=29:0.20. It was confirmed that smaller GO sheets enhance the etching reaction more. Small GO sheets have an advantage in terms of both the increase of edge areas which is well-known as catalytical active sites and the mass transport of reactants and byproducts, which results in a high etching rate. This result agrees with the previous report of GO-assisted Ge etching by Hirano[29].

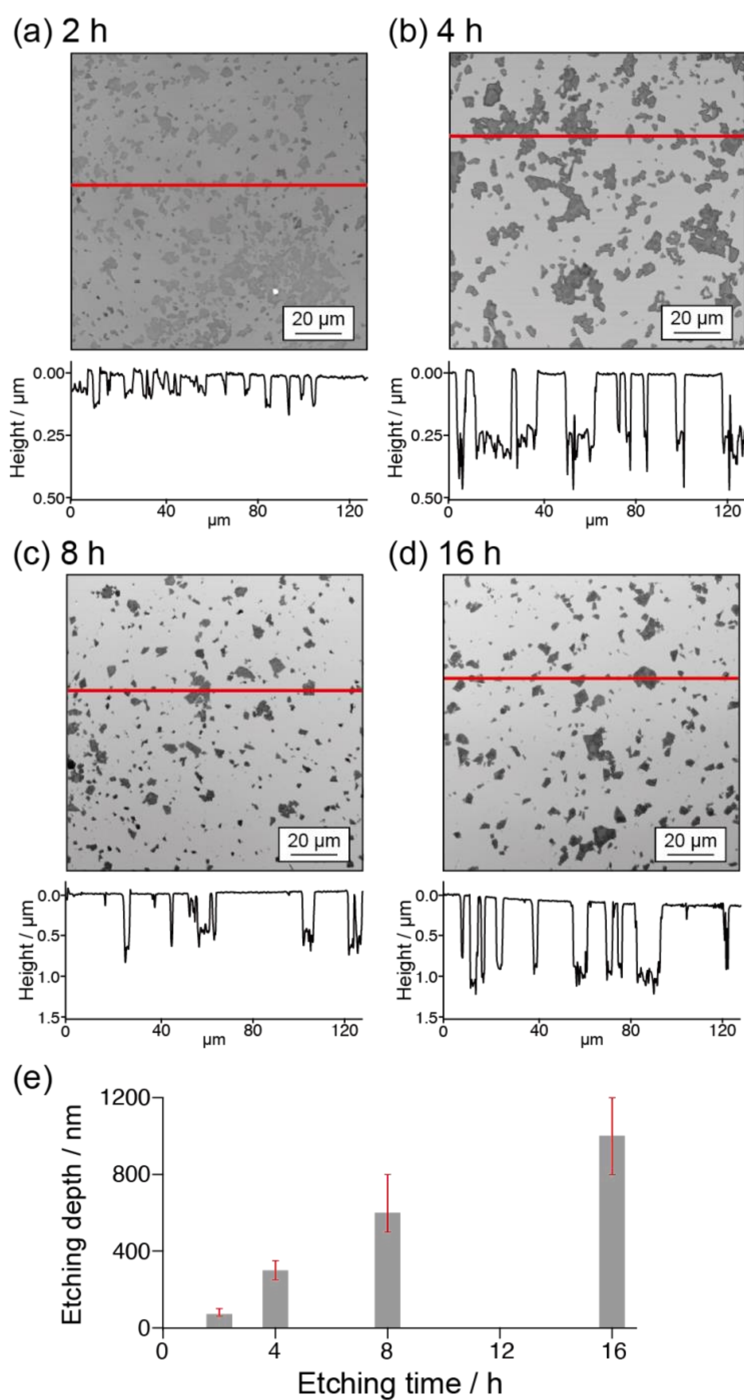

Figure 3-6 3D laser microscope topographic images and cross-sectional profiles along lines of GO-loaded silicon substrates after vapor phase etching at 50°C for (a) 2 hours, (b) 4 hours, (c) 8 hours, and (d) 16 hours. The molar concentration of the etching solution was [HF]:[H_2O_2]=29:0.20 (mol L^{-1}). (e) The relation between etching depth and etching time.

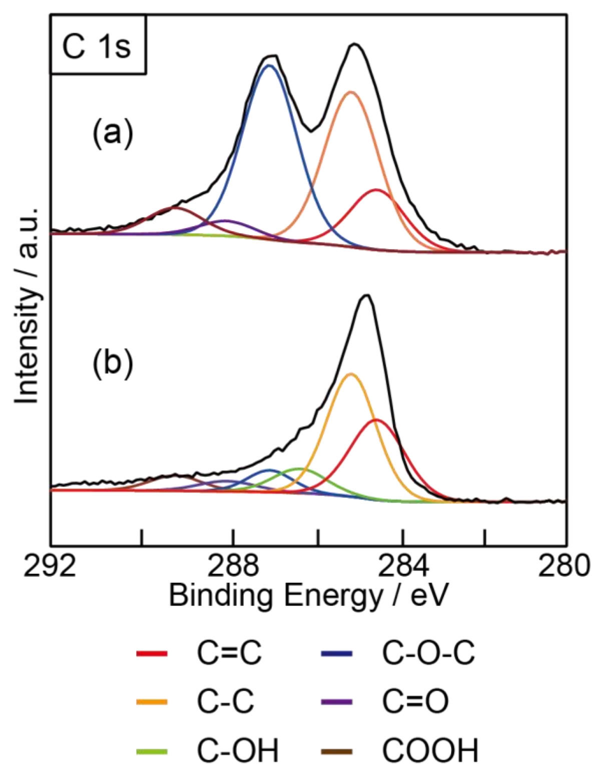

Figure 3-7 XPS C 1s spectra of the GO-loaded silicon substrate (a) before and (b) after vapor phase etching at 50°C for 1 hour with the mixture of HF and H_2O_2. The molar concentration of the etching solution was [HF]:[H_2O_2]=29:0.20 (mol L^{-1}).

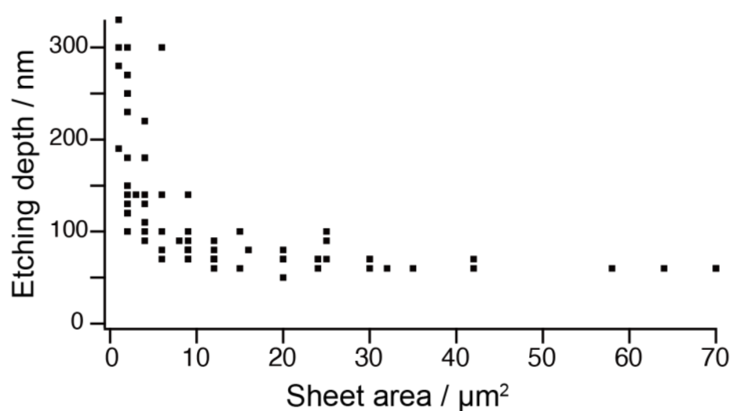

Figure 3-8 The relation between GO sheet size and etching depth in vapor phase etching. The etching condition was 50°C for 2 hours, and the molar concentration of the etching solution was [HF]:[H_2O_2]=29:0.20 (mol L^{-1}).

3.4 The mechanism of vapor phase etching of silicon assisted by GO

To clarify the mechanism underlying the formation of the porous structure, the surface condition of silicon after vapor phase etching was analyzed by XPS. Figure 3-9 shows the XPS Si 2p spectra of samples after vapor phase etching with each etchant composition. When the concentration of the oxidant was low, only one peak at approximately 99.8 eV derived from Si-Si was observed as shown in Figures 3-9 (b) and (d). On the other hand, when the concentration of the oxidant was high, a peak at approximately 103.5~103.9 eV derived from Si-O was confirmed[81,82], indicating that a larger oxide layer formed on the silicon surface within the XPS sampling depth. These surface conditions after etching samples play an important role in the formation of a porous structure on bare silicon areas.

Previous studies reported the vapor phase etching of silicon assisted by metal or carbon materials; however, the underlying mechanisms remain unclear[23,72,83]. Kim et al. reported titanium nitride-assisted silicon etching in a vapor phase and discussed the mechanism responsible for changing the experimental conditions[83]. When the silicon substrate was heated to the etchant temperature during the vapor phase etching process, the etching reaction proceeded without the formation of a condensed water layer on the substrate. The experimental conditions in this chapter were similar to those used by Kim. However, a previous study reported the presence of an adsorbed water layer, the thickness of which depended on the relative humidity, on the silicon substrate[84]. In the etching system, the aqueous solution composed of HF and oxidants was heated with the silicon substrate in a shielded container, and, thus, relative humidity in the container during vapor phase etching was expected to be high. This implies that the adsorbed water layer forms on the silicon substrate in the etching process, and reactants or products will diffuse through the adsorbed water layer.

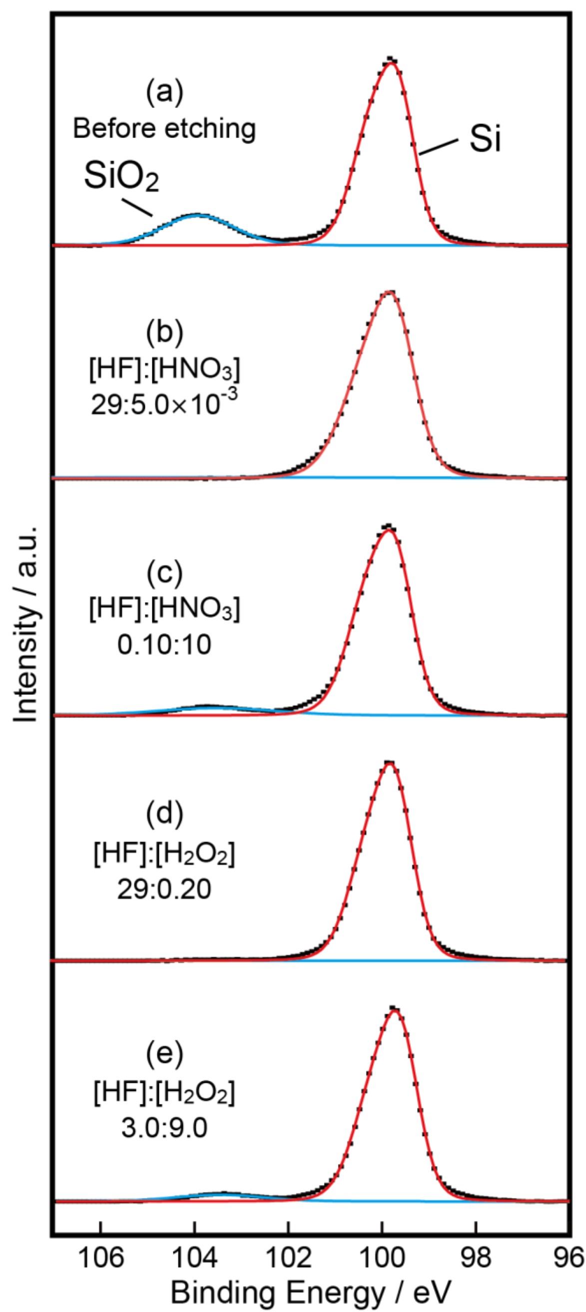

Figure 3-9 XPS Si 2p spectra of the Si substrate (a) before and (b)-(e) after vapor phase etching at 50°C for 2 hours with each etching solution. The molar concentrations of etching solutions were (b) $[HF]:[HNO_3]=29:5.0\times10^{-3}$, (c) $[HF]:[HNO_3]=0.10:10$, (d) $[HF]:[H_2O_2]=29:0.20$, and (e) $[HF]:[H_2O_2]=3.0:9.0$ (mol L^{-1}).

Etching reaction equations in the vapor phase etching of silicon are described as follows[85–87]:

Si oxidation

$$Si + 4HF \rightarrow SiF_4 + 4H^+ + 4e^-$$

or

$$Si + 2H_2O \rightarrow SiO_2 + 4H^+ + 4e^-$$

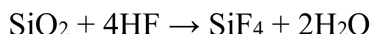

$$SiO_2 + 4HF \rightarrow SiF_4 + 2H_2O$$

Oxidant reduction

$$HNO_3 + 3H^+ + 3e^- \rightarrow NO + 2H_2O$$

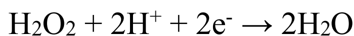

$$H_2O_2 + 2H^+ + 2e^- \rightarrow 2H_2O$$

In most cases of the assisted etching of silicon, catalysts promote the oxidant reduction reaction. In the case of GO-assisted silicon etching, GO also enhances oxidant reduction reactions because it has been shown to function as a catalyst for the reduction of H_2O_2 and HNO_3[30,32]. When GO works as a catalyst for those oxidant reduction reactions, the location of the catalytical active sites is often discussed. Inherent edges, defects, and heteroatoms (such as nitrogen and sulfur) on GO sheets function as active sites because these parts alter the local density of π-electrons[42]. In the previous section, the relationship between GO structures and the etching rate was discussed and it was proved that defects on GO contributed to its catalytic property in liquid phase etching[80].

The surface chemical condition of silicon after vapor phase etching depends on the composition of the etching solution prepared; however, GO-covered areas were etched faster than non-covered areas under all conditions in my experiments. With a high oxidant concentration etchant, a silicon oxide layer formed on the silicon surface. In this case, positive holes produced by the oxidant reduction were scattered into silicon to such an extent that the surface was heterogeneously oxidized, which resulted in undesirable

etching and roughening on the bare silicon surface[88]. On the other hand, the silicon oxide layer was not detected when the HF concentration was high in the prepared etching solution. These results indicate that oxidant reduction is the rate-determining step and the non-uniform oxide layer did not form on bare silicon areas.

In contrast, an obvious porous structure was not formed after vapor phase etching with HF-rich HF-H_2O_2 etching solution. Some papers about Mac Etch process suggest the mechanism of porous structure formation[20,48,83,89–91]. When the assisted-etching reaction is limited by mass transport, unconsumed charges produced by the oxidant reduction reaction diffuse through the interface between catalyst and silicon to the inside of the silicon, and the charges are consumed to oxidize silicon where catalysts are not covered, which results in porous structure formation. In my experiment with the etching solution of HF-rich HF-H_2O_2, not mass transport but charge production by the oxidant reduction is the rate-determining step, and surplus holes are not scattered into silicon, which results in preventing porous structure formation. However, a porous structure formed on silicon around the pores formed by GO-assisted etching with an HF-rich HF-HNO_3 solution, as shown in Figure 3-4(a). If all of the holes produced by the HNO_3 reduction reaction are not consumed at silicon under GO sheets, excess positive holes scatter to silicon around GO sheets. Scattered holes are utilized for silicon oxidation and the formation of the porous structure. Another reason for porous structure formation is due to the stain etching by HF-HNO_3. The stain etching by HF-HNO_3 is explained by the increase of intermediates concentration in the concave. However, the porous structure only formed around GO sheets. Porous structure formation needs a silicon dissolution reaction and the dissolution consumes positive holes. Considering these discussions, porous structure formation with HF-HNO_3 etching solution occurs by combining the stain etching of HF-HNO_3 and the excessive positive hole scattering.

In the HF-H_2O_2 system, the GO-assisted silicon etching rate in the vapor phase (60 nm h^{-1}) is larger than that in the solution process (1 nm h^{-1})[79], and deeper etching at the edges of GO sheets than at the center was seen in the solution process. This behavior suggests that the GO-assisted etching reaction in the HF-H_2O_2 solution is limited by the diffusion of the products to some extent. The vapor phase is more advantageous than the liquid phase in terms of mass transport, which results in a higher etching rate than that with the solution process[83]. A number of hypotheses have been proposed for why the vapor phase is more advantageous than the liquid phase in terms of mass transport; however, it remains unclear. The etch rate decreases in the HF-HNO_3 system when the vapor phase is utilized. In the HF-HNO_3 system, the etching rate is controlled by the intermediate reactant of HNO_2 or NO^+ [64]. The concentration of intermediates on the silicon surface may be lower in the vapor phase than in the liquid phase because the vapor phase has an advantage over the liquid phase in terms of the mass transport of gaseous molecules. This decrease in the concentration of intermediates on the silicon surface results in the restriction of the etching rate in the vapor phase.

In both the oxidants, silicon under GO was etched faster than the not-covered area with the oxidant-rich etchants. This phenomenon can not be explained by the mechanism of catalyst-assisted etching because the oxidant reduction reaction is not the rate-determining step. Fan et al. reported site-selective etching of SiO_2 under 2D material of graphene and MoS_2 by exposing HF vapor[92,93]. SiO_2 etching reaction produces water, and other papers reported that the SiO_2 etching reaction by the vapor is accelerated by the adsorbed water layer[94,95]. Fan concluded that produced water can not diffuse away easily under the 2D materials, and the SiO_2 etching was accelerated only under the 2D materials. Figure 3-10 shows a GO-loaded 300 nm SiO_2/Si substrate after exposure to HF vapor at 40℃ for 1 minute. It was confirmed that the SiO_2 vapor etching reaction was enhanced

under GO, indicating that the phenomenon reported by Fan et al. occurs in the case of GO. The possible mechanism of vapor phase GO-assisted silicon etching with the oxidant-rich etchants can be explained as follows; the silicon surface was covered by SiO_2 because the silicon oxidation reaction was faster than the SiO_2 etching reaction. Then, SiO_2 etching can be accelerated only under GO due to the disadvantage of water diffusion, which resulted in the formation of the hollow with the shape of GO sheets even in the vapor etching with the oxidant-rich etchants.

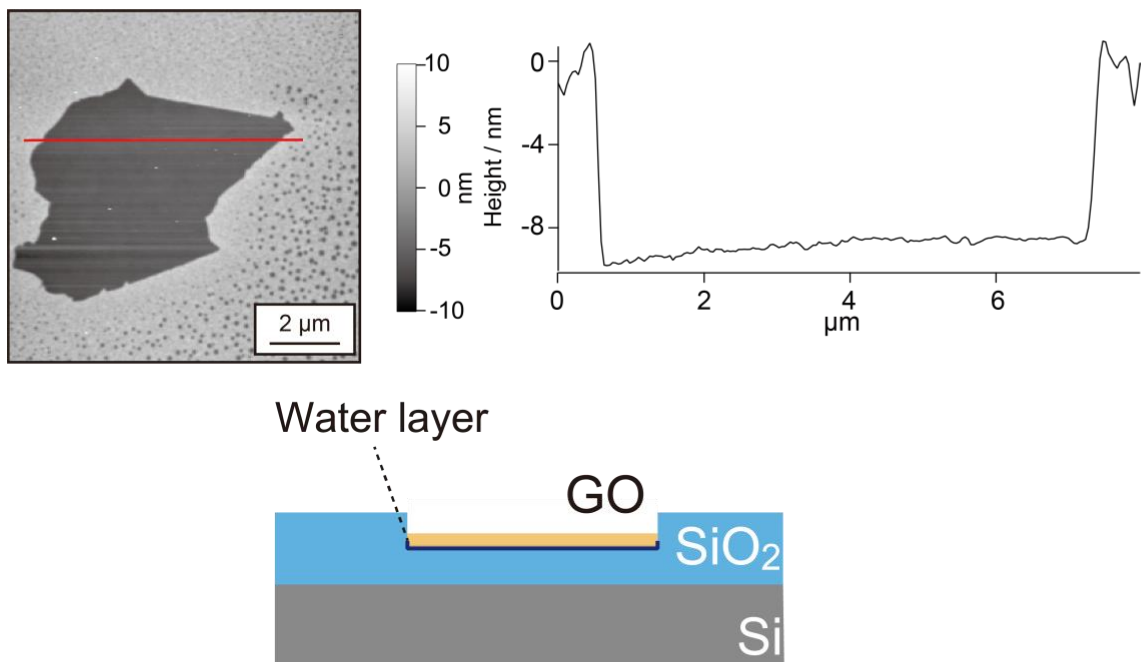

Figure 3-10 An AFM topographic image, a cross-sectional profile, and a schematic illustration of GO-loaded SiO_2/Si substrate after vapor phase etching at 40℃ for 1 min. The molar concentration of the etchant was [HF]=23 (mol L^{-1}).

Reaction kinetics are generally controlled by the Arrhenius equation when the reaction is not limited by the diffusion of products or reactants[63]. In the Arrhenius equation, the reaction rate increases with elevations in the reaction temperature until the reaction rate is limited by mass transport. To obtain a more detailed understanding of GO-assisted silicon etching in the vapor phase, the temperature dependency of the etching rate was examined. Figure 3-11 shows topographic images of silicon substrates after GO-assisted etching in the vapor phase at each temperature for 2 hours. Considering the sheet size effect on the etching rate, the etching rate of GO sheets with a size larger than 10 μm^2 was evaluated. With elevations in the etching temperature to 60°C, increases were observed in the etching rate (ca. 80 nm h^{-1}). However, the etching rate was saturated as the etching temperature increased to 60 or 70°C. This behavior suggests that the rate-determining step changed at approximately 60°C. An elevation in the etching temperature increased the partial pressure of HF and oxidants or the reaction rate. These changes may contribute to an increased etching rate. However, the etching rate was saturated even when the etching temperature was increased to higher than 60°C. This implies that the reaction rate at an etching temperature higher than 60°C was so fast that the diffusion of products or reactants restricted the etching rate. The XPS Si 2p spectra shown in Figure 3-9(d) confirmed that silicon oxide layers did not form on the sample after vapor phase etching in this system, which implies an insufficient supply of H_2O_2 or the inadequate diffusion of SiF_4.

A marked increase in the etching rate was not confirmed and the etching behavior of GO-covered areas was not uniform at a higher concentration of H_2O_2 (shown in Figure 3-5). This means that the amounts of oxidants supplied did not markedly affect the etching rate of GO-covered areas, but significantly contributed to the roughening of both bare silicon areas and GO-covered areas.

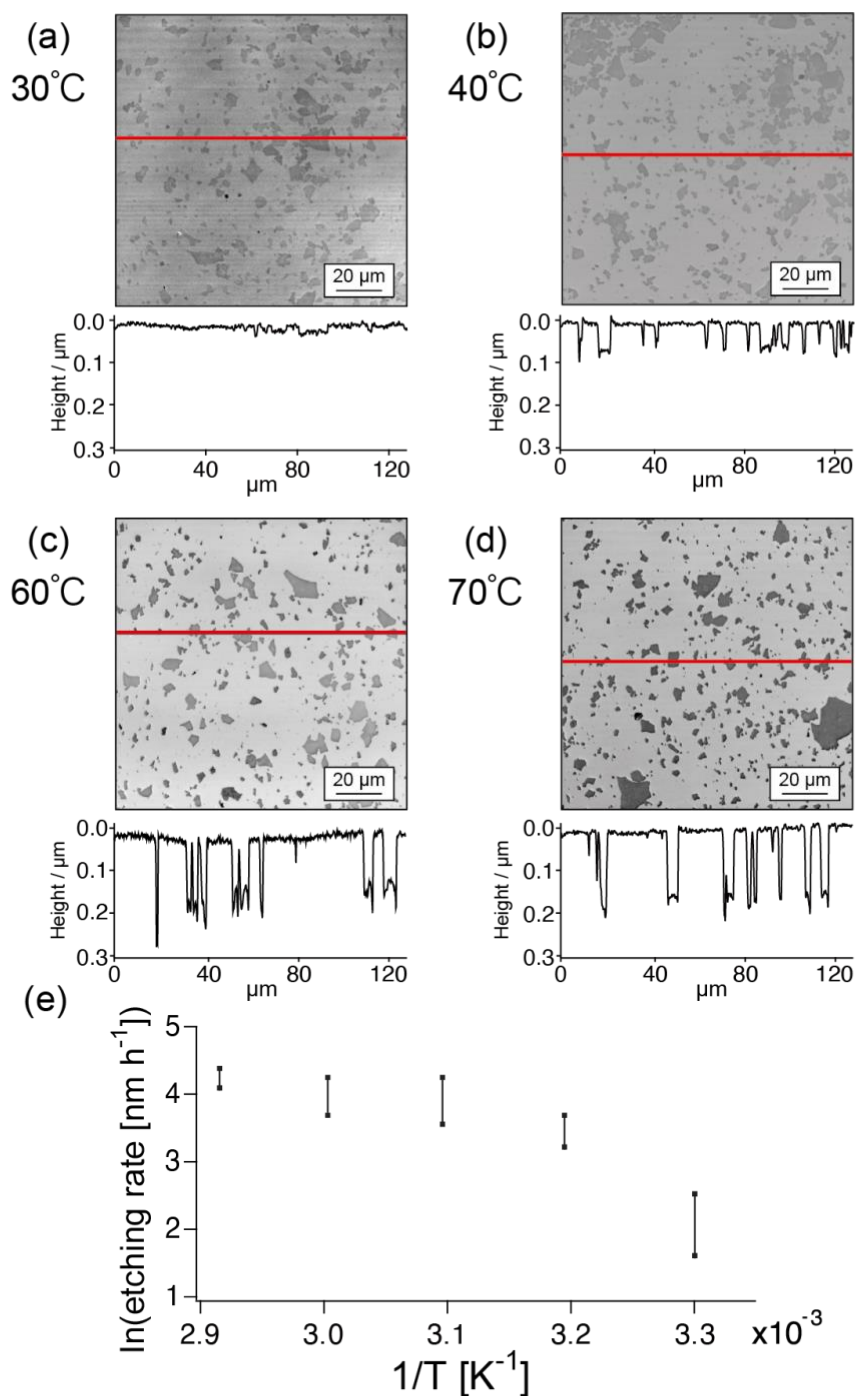

Figure 3-11 3D laser microscope topographic images and cross-sectional profiles along lines of silicon substrates loaded with GO sheets after vapor phase etching for 2 hours. The temperatures of the etching solutions were (a) 30°C, (b) 40°C, (c) 60°C, and (d) 70°C. The molar concentration of the etching solution was [HF]:[H_2O_2]=29:0.20 (mol L^{-1}). (e) The relation between the etchant temperature and the etching rate.

3.5 Pattern etching of silicon assisted by patterned GO by combining μCP

The vapor phase GO-assisted etching of silicon and optimized etching conditions were demonstrated in the previous section. Then, the pattern etching of silicon combining vapor phase etching with the μCP of GO sheets was conducted. Figures 3-12 (a) and (b) show AFM topographic images of the COP stamp before and after a load of GO through spin-coating. The circle convex parts with a height of *ca.* 140 nm were formed on the COP surface, and obvious roughening of the convex surface was not observed after a load of GO. This implies that GO sheets were loaded on the COP stamp without aggregation.

Figure 3-12(c) shows an AFM topographic image of the silicon substrate after stamping. There were circle patterns with a thickness of 4 nm on the substrate. Figure 3-12(d) shows the Raman spectra obtained inside and outside of the circle patterns on the silicon substrate. One sharp peak at approximately 520 cm^{-1} and a broad band at approximately 950 cm^{-1} derived from silicon were observed outside circle patterns[96]. In contrast, two additional peaks at approximately 1300 and 1600 cm^{-1} were observed inside circle patterns. These peaks originated from the GO structure, which indicated that the transferred circle patterns included GO sheets[97]. These transferred circle patterns were thicker than monolayer GO sheets because the silica convex of the stamp may be stuck on GO sheets or multi-layer GO sheets were transferred on the silicon substrate.

Figures 3-13(a) and (c) show schematic illustrations of the COP stamp and its pressing process. The COP substrate was etched with Xe excimer lamp irradiation[98]. The synthesized COP stamp had protrusions that were composed of a SiOx layer and bulk COP[77]. After the GO-loaded COP stamp was pressed onto a silicon substrate, circle

patterns with a thickness of 4 nm formed, which was thicker than monolayer GO sheets, as shown in Figure 3-12(c). This was due to the adhesion of a SiOx layer or multi-layer of GO sheets. The transfer of SiOx layer was confirmed when the COP stamp without GO sheets was pressed onto a silicon substrate. Figure 3-13(b) shows an AFM topographic image of the silicon substrate after pressing the COP stamp without GO sheets with a load of 400 N for 1 hour. Circle patterns with a thickness of *ca.* 4 nm formed on the silicon substrate. This result implies that when the COP stamp with GO sheets was pressed on the silicon substrate, GO sheets and the SiOx layer were both simultaneously transformed to the substrate (shown in Figure 3-13(c)). Moreover, the chemical conditions of the transferred structures on the silicon substrate were confirmed by XPS, as shown in Figure 3-13(d) and (e). A peak from a native oxide layer on the silicon substrate and from silica transferred from SiOx/COP stamp were not separated from the peak derived from Si-O of XPS Si 2p spectra, when the silicon substrate with the transferred structures was analyzed. In this experiment, the native oxide layer on the silicon substrate was removed by 5 wt% HF solution before the SiOx/COP stamp was pressed. The silicon substrate without the native oxide layer before stamping analyzed in this experiment was kept in the air for 1 hour to arrange the condition of the sample after stamping. A peak around 103 eV, which was derived from Si-O components, was confirmed on the silicon with transferred structures. This result indicates that silica can also be transferred by the stamping process.

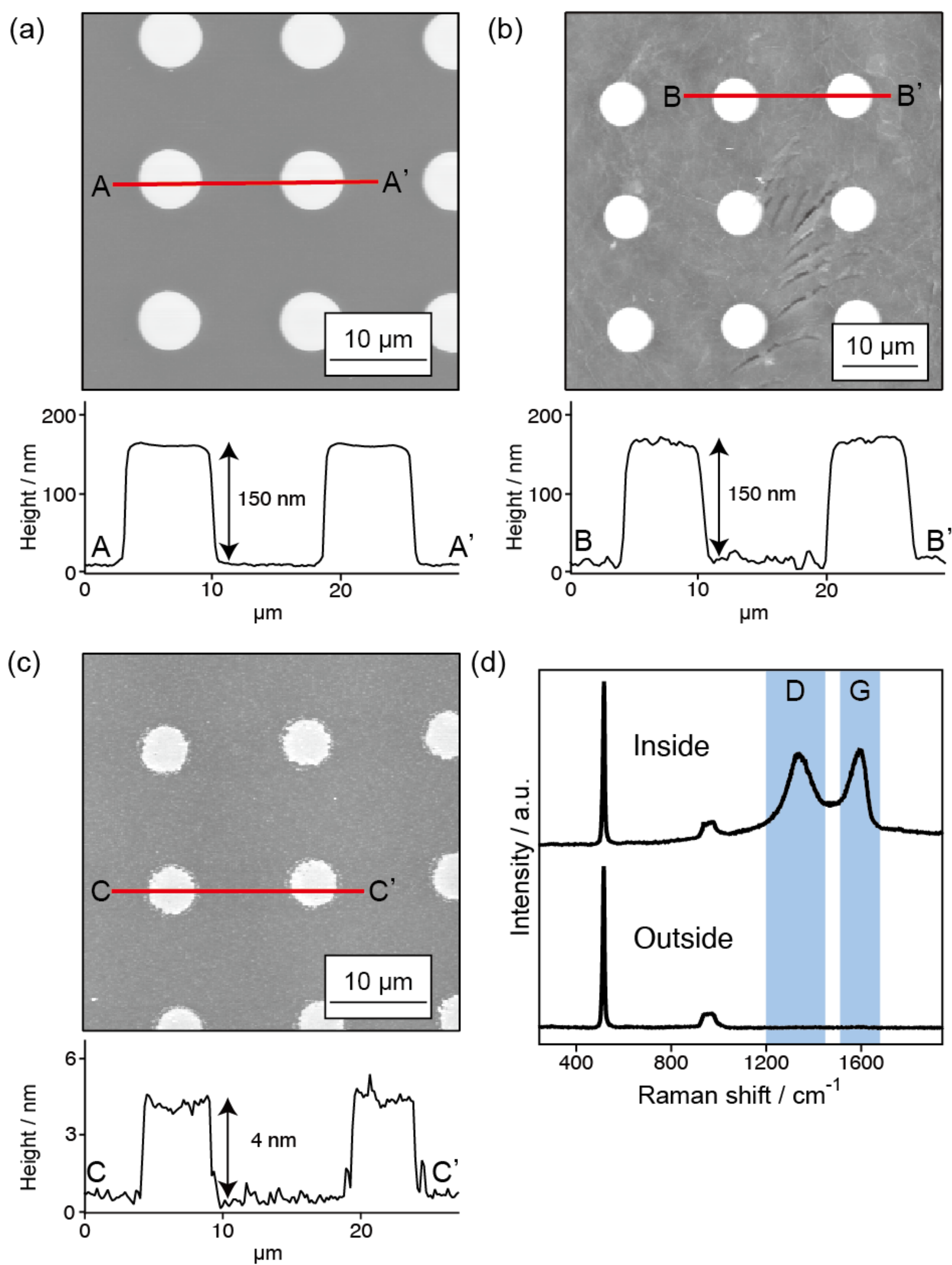

Figure 3-12 AFM topographic images, and cross-sectional profiles along lines of (a) a COP stamp, (b) a COP stamp after GO sheets were loaded, and (c) a silicon substrate after the µCP of GO patterns. (d) Raman spectra of the stamped silicon obtained from inside and outside the circle pattern.

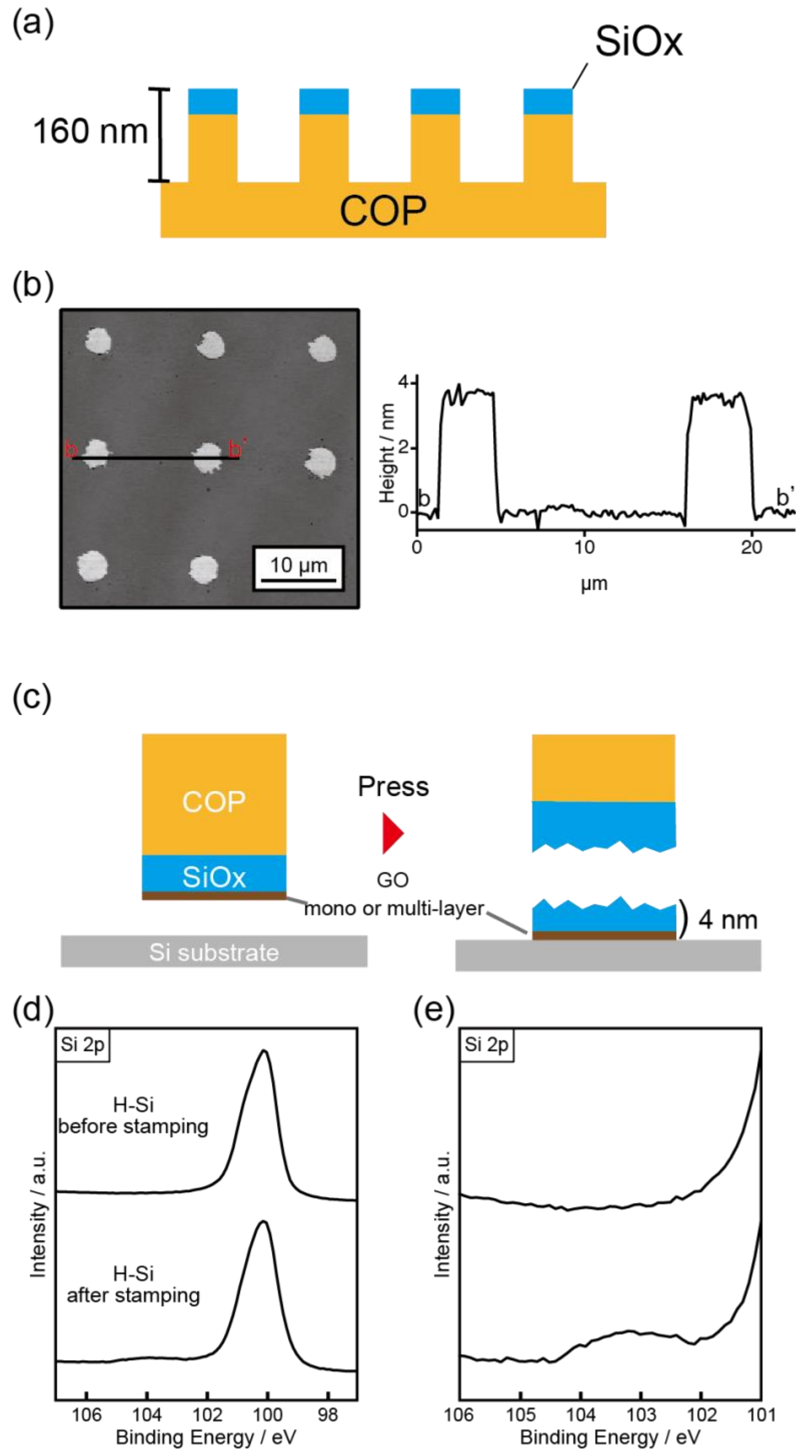

Figure 3-13 (a) A schematic illustration of the COP stamp. (b) An AFM topographic image after pressing the COP stamp without loading GO sheets. (c) Schematic illustrations of the COP stamp before and after pressing. (d) XPS Si 2p spectra and (e) focused spectra of hydrogen-terminated silicon before and after stamping for 1 hour.

Figures 3-14(a) and (b) show a topographic image by 3D laser microscopy and a cross-sectional SEM image of the silicon after pattern etching in the vapor phase at 50°C for 16 hours with a solution of HF-H_2O_2 (the molar concentration of the etching solution is [HF]:[H_2O_2]=29:0.20). The transferred areas were etched at approximately 1 μm deeper than the outside of the circle, which indicates that GO sheets etch the desired silicon surface by combining μCP. The etching depth using GO loaded through μCP was slightly lower than that using spin-coated GO sheets. This may be because silica transferred along with GO sheets hinders etching at the beginning of the etching process or multi-layer GO sheets enhance the etching reaction less than the mono-layer GO sheet.

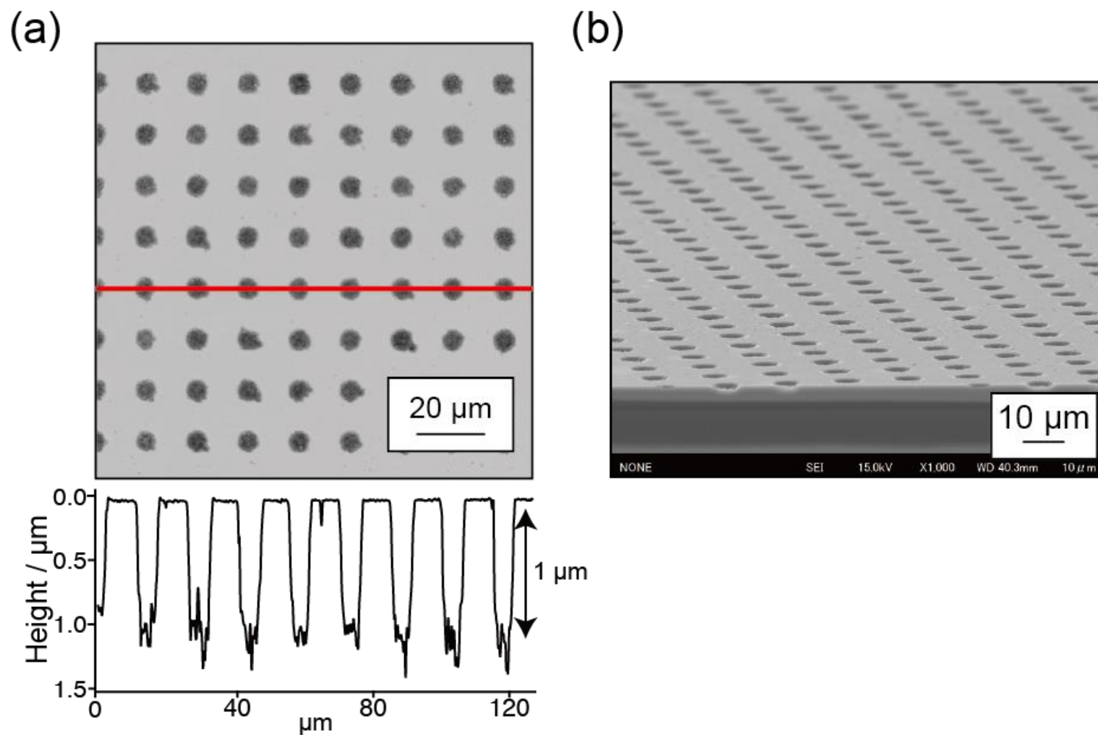

Figure 3-14 (a) A 3D laser microscope topographic image, a cross-sectional profile along a line, and (b) SEM image of silicon substrates loaded with GO sheets after vapor phase etching at 50°C for 16 hours. The molar concentration of the etching solution was [HF]:[H_2O_2]=29:0.20 (mol L^{-1}).

3.6 Conclusion

In this chapter, the catalytic performance of GO sheets towards etching reactions in the vapor phase was confirmed, and the μm-order processing of silicon surfaces was successfully performed by optimizing etching conditions without the formation of a porous structure, which is conventionally formed in catalyst-assisted silicon etching. In addition, the difference in etching behaviors between the liquid phase and vapor phase was discussed. The rate-determining step in the etching reaction plays an important role in both the etching rate on GO sheets and the roughening of bare silicon areas. The elucidation of the etching mechanism will provide a more detailed understanding of the catalyst-assisted etching of a number of semiconductor surfaces.

Furthermore, by combining vapor phase GO-assisted silicon etching and the μCP process, the pattern etching of silicon was demonstrated to process the desired areas. By optimizing photolithography, the stamping process, or stamp materials, etching accuracy in the horizontal direction may be improved.

The aspect ratio of GO-assisted etching is still very low compared with Mac Etch. To solve this problem, it is necessary to improve both the catalytic activities of GO and the accurate nanofabrication of GO. The former problem can be solved by heteroatom doping or structural defects engineering on GO[42]. The latter problem can be addressed by other nanofabrication methods such as a general lithographic method[99], laser processing[100], plasma etching[101], etc.

Chapter 4 Chemical etching of InP assisted by graphene oxide

4.1 Introduction

In this section, GO application to the catalyst for the InP etching reaction was demonstrated. InP is established as an important material for optoelectronics and high-frequency devices due to its high carrier mobility and low surface recombination velocity compared with other III-V semiconductor materials. Moreover, some researchers attempted to apply InP nanostructures to next-generation devices such as Fin FET[102], high-efficiency solar cells[103], etc. Recently, metal-assisted chemical etching was applied to the InP surface for the fabrication of its nanostructure[17,18,104]. However, metal catalysts enhance the etching reaction on the non-covered areas, not under the catalysts, and its mechanism is still an open question. In this report, the expansion of the application of GO-assisted chemical etching and a deeper comprehension of assisted etching of InP were attempted by investigating the relationship between the etching behaviors with different etchant compositions and the surface conditions of the InP surface after etching.

4.2 Experimental procedure

GO was synthesized by a modified Hummers' method described in the previous section[43]. To confirm whether GO enhances the InP etching reaction, the InP substrate on which GO sheets were randomly loaded was prepared as the etching sample. Figures 4-1(a)-(c) show schematic illustrations of the etching process. A single-side polished n-type InP substrate (S-doped, (100), $\rho=3.5\times10^{-3}$ Ω cm, MTI Corp.) was utilized as an etching sample. The InP substrate was washed by immersion in acetone, ethanol, and ultrapure water (with resistivity of 18.2 MΩ cm). The synthesized GO was randomly loaded on the

InP substrate by spin-coating its dispersion(500 rpm for 15 s and 2000 rpm for 150 s). The GO-loaded InP substrate was immersed in the etching solutions composed of sulfuric acid (H_2SO_4, 96 wt%, for electronics industry, Fuji Film Wako Pure Chemical Corp.) or hydrochloric acid (HCl, 35 wt%, for electronics industry, Fuji Film Wako Pure Chemical Corp.) as the acid and hydrogen peroxide (H_2O_2, 30 wt%, analytical grade, Fuji Film Wako Pure Chemical Corp.) or nitric acid (HNO_3, 1 mol L^{-1}, analytical grade, Fuji Film Wako Pure Chemical Corp.) as the oxidant at 25℃. The samples after etching were observed by 3D laser microscopy and analyzed by XPS. The spectra obtained were calibrated to the In 3d peak at 444.8 eV[105], and analyzed using the Casa XPS software package[106].

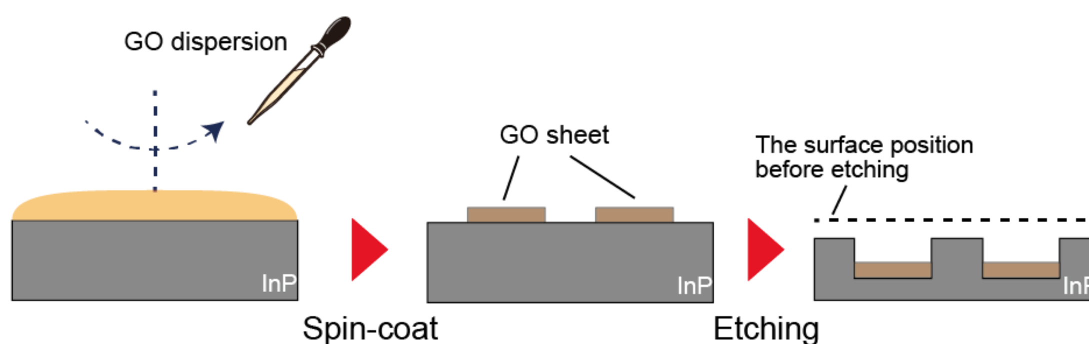

Figure 4-1 Schematic images of the GO loading on an InP substrate and GO-assisted InP etching.

4.3 Etching behavior with various types of etching compositions

Figure 4-2 shows a typical AFM topographic image of the InP sample loaded with GO sheets. Judging from the cross-sectional profile, the thickness of GO was around 1 nm, which is in good agreement with a single layer of GO. The sheet size of GO was typically several μm. Figures 4-3(a)-(d) show topographic images of the GO-loaded InP substrate after etching for 4 hours at 25°C in each etching solution, obtained by a 3D laser microscope. As the etching solution, H_2SO_4 or HCl was utilized as an acid solution because it is well-known that they can dissolve InP[107]. As the oxidant of the etchant, H_2O_2[30] or HNO_3[32] was utilized due to the catalytic ability of GO towards these oxidant reductions. The molar concentrations of the etching solution were (a) $[H_2SO_4]$:$[H_2O_2]$= 17:0.90 (b) $[H_2SO_4]$:$[HNO_3]$=19:5.0×10^{-3}, (c) [HCl]:$[H_2O_2]$=2.2:2.0, and (d) [HCl]: $[HNO_3]$=2.2:5.0×10^{-2} (mol L^{-1}), respectively. Figures 4-3(a)-(c) show GO-sheet-like convex structures, indicating that the etching rate of the GO-covered areas was slower than that of the non-covered areas. That is, the GO sheets worked as masks when the substrate was etched by the H_2SO_4-containing solutions or the HCl-H_2O_2 solution. In contrast, GO-covered areas were etched deeper than non-covered areas in the HCl-HNO_3 solution, shown in Figure 4-3(d). These results indicate that GO enhances the InP etching reaction with the optimized HCl-containing solution.

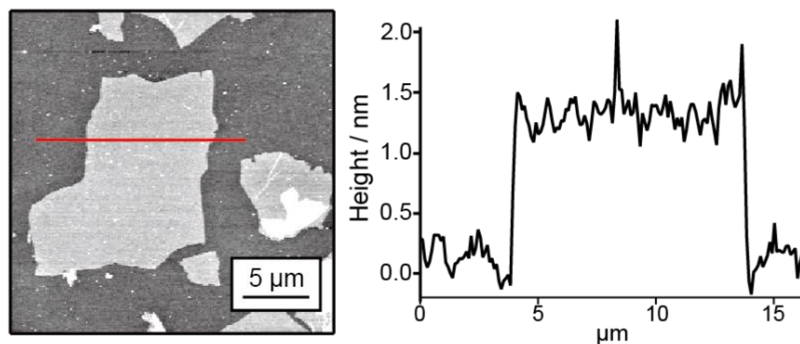

Figure 4-2 An AFM topographic image of GO sheets on an InP substrate and a cross-sectional profile obtained along the line.

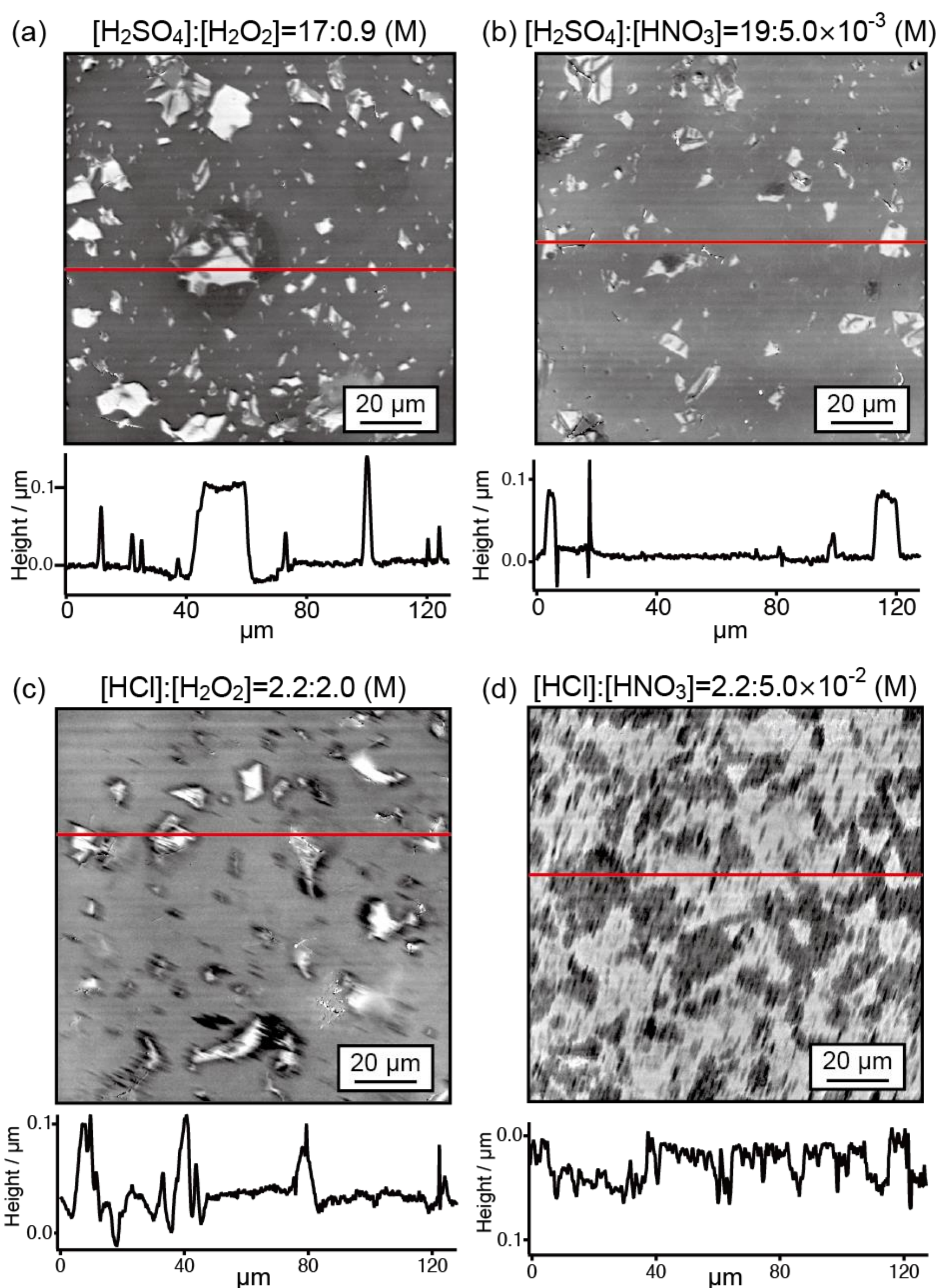

Figure 4-3 3D laser microscope topographic images and cross-sectional profiles along the lines of the InP substrates loaded with GO sheets after etching at 25°C for 4 hours. The molar concentration of the etching solution was (a) $[H_2SO_4]$:$[HNO_3]$=17:0.90 (b) $[H_2SO_4]$:$[H_2O_2]$=19:5.0×10^{-3}, (c) [HCl]:$[H_2O_2]$=2.2:2.0, and (d)[HCl]:$[HNO_3]$=2.2:5.0× 10^{-2} (mol L^{-1}), respectively.

It may be possible that GO can be oxidized by the oxidants in the assisted-etching process. Therefore, the chemical condition of GO was evaluated by XPS. Figures 4-4(a) and (b) show XPS C1s spectra of the samples after etching in each solution. The spectra were deconvoluted to 6 peaks, i.e., sp^2 C=C at 284.4 eV, sp^3 C–C at 285.0 eV, C–OH at 286.2 eV, C–O–C at 286.9 eV, C=O at 287.9 eV, and COOH at 289.1 eV. Peaks derived from oxygen functional groups decreased after the etching process, indicating that the oxygen functional groups on GO were removed after etching in each etching solution. However, the peak derived from oxygen functional groups, mainly from the epoxy group, remained especially in the case of samples after the immersion in the H_2SO_4-containing solution. The removal of oxygen functional groups in the etching process, that is GO reduction reaction, may come from a pair reaction of the InP oxidation reaction. It was reported that GO can be electrochemically reduced by applying negative vias. In our system, GO can be reduced as the pair reaction of InP oxidation. In this reduction, it is necessary to attach GO to the bare InP surface. In the etching process with the H_2SO_4-containing solution, the InP surface was covered with the InP oxide layer and this oxide layer prevented attaching GO to the bare InP surface and suppressed the GO reduction compared with the sample after the etching in the HCl-containing solution. In this discussion, it is possible that the GO reduction is the origin of the GO-assisted InP etching because the GO reduction enhance the InP oxidation which cause the promotion of the InP etching reaction under GO. However, in the HCl-H_2O_2 solution, GO did not enhance the etching reaction although GO was reduced in the immersion in the HCl-H_2O_2 solution. This means that GO reduction did not contribute to the GO-assisted InP etching reaction. This behavior is consistent with the chapter 2 and 3, and indicates that a strong oxidant, H_2O_2 or HNO_3, did not oxidize GO sheets, but was consumed in the etching reaction.

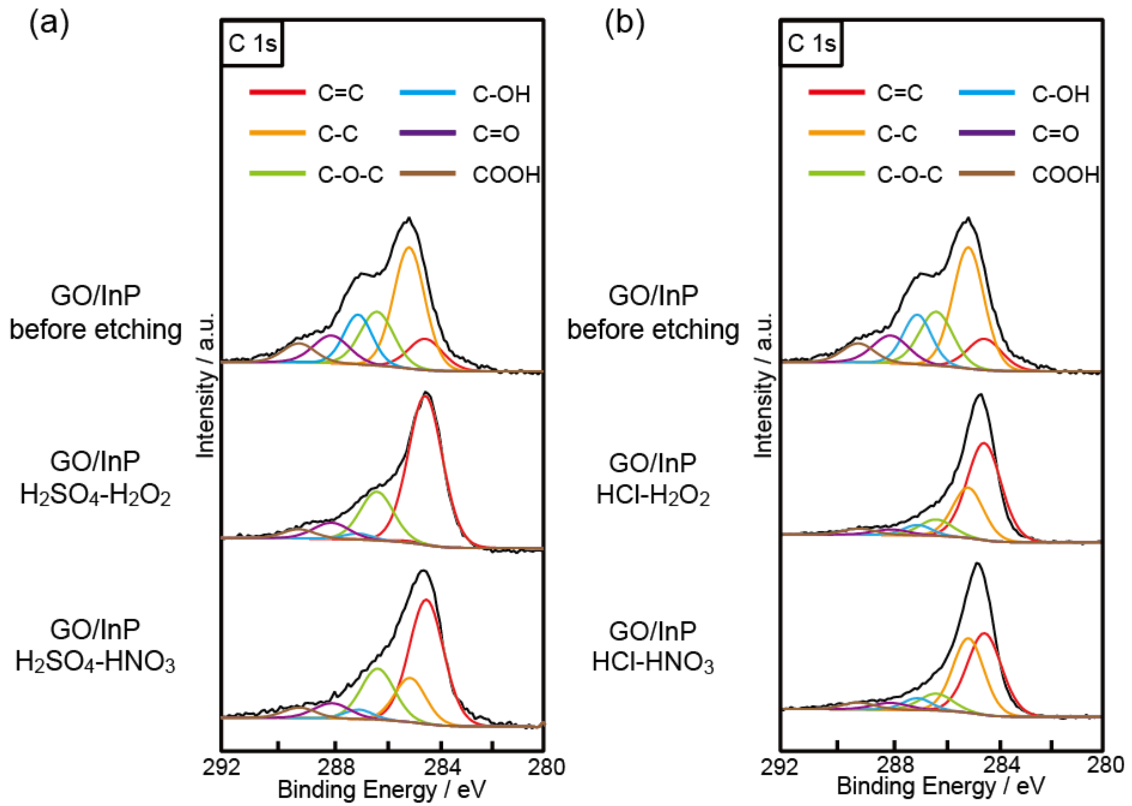

Figure 4-4 XPS C 1s spectra of the GO-loaded InP samples before and after etching for 2 hours in (a) H_2SO_4-containing solution and (b) HCl-containing solution. The molar concentrations of the etching solution were the same as described in Figure 4-3.

For a deeper comprehension of GO-assisted InP etching, chemical conditions of the InP samples before and after etching were analyzed by XPS. Figures 4-5(a) and (b) show In 3d spectra of InP samples before and after etching in each etching solution of which concentration is described in the previous paragraph. The spectra were deconvoluted to 2 peaks, i.e. InP at 444.8 eV and oxide bonding states such as $InPO_4$, $In_2(SO_4)_3$, etc. at 446.4 eV. R_{oxide} described in Figure 4-5 was the percentage of the area of the oxide peak. The peak derived from oxide bonding states newly appeared when the InP substrate was immersed in the H_2SO_4-containing solutions, indicating the InP oxide layer formation[108]. Moreover, these peaks from the GO-loaded InP were larger than those of the substrate without GO sheets although the spectra of GO-loaded samples included the information of the uncoated portion.. This result means that a thicker oxide layer formed under the GO sheets than on non-covered areas. On the contrary, the peaks derived from the oxide layer were not confirmed from the InP substrate after etching in HCl-containing solutions, as shown in Figure 4-5(b).

Reaction equations of InP etching in the acids and the oxidants are described as follows,

Oxidant reduction

$$HNO_3 + 3H^+ + 3e^- \rightarrow NO + 2H_2O$$

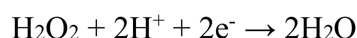

$$H_2O_2 + 2H^+ + 2e^- \rightarrow 2H_2O$$

InP oxidation[109]

$$InP + 4H_2O \rightarrow InPO_4 + 8H^+ + 8e^-$$

or

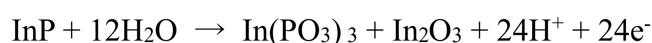

$$InP + 12H_2O \rightarrow In(PO_3)_3 + In_2O_3 + 24H^+ + 24e^-$$

InP oxide dissolution by the acids

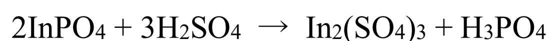

$$2InPO_4 + 3H_2SO_4 \rightarrow In_2(SO_4)_3 + H_3PO_4$$

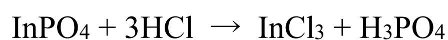

$$InPO_4 + 3HCl \rightarrow InCl_3 + H_3PO_4$$

The oxidation of InP was explained by two reaction paths. In the GO-assisted InP etching, the exact oxidation reaction path can not be decided only from the XPS In 3d spectra. The difference in the surface conditions after etching can be explained by the stability of the byproducts formed on the InP surface during the etching process. It was reported that $In_2(SO_4)_3$ can form on the InP surface during the etching process with the H_2SO_4-containing solution[110], and the $In_2(SO_4)_3$ can be stable in the etching solution utilized in these experiments. XPS P 2p and S 2p spectra of the InP samples after etching in the H_2SO_4-containing solutions were analyzed and most of the InP oxide on the surface derived from $In_2(SO_4)_3$, not from $InPO_4$, shown in Figure 4-6. However, the $In_2(SO_4)_3$ itself is generally soluble in water. In the etching result of the H_2SO_4-containing solution at Figure 4-3, the H_2SO_4 concentration was very high, and there was little water in the etchant. Therefore, there was not enough water to dissolve $In_2(SO_4)_3$, which resulted in the remaining $In_2(SO_4)_3$ on the InP surface. Another possibility of $In_2(SO_4)_3$ insolubility is due to the high viscosity of the H_2SO_4-containing solution. The area under GO is disadvantageous in terms of mass transport, and the higher ion concentrations such as In^{3+} or SO_4^{2-} under GO than that on the bare InP should decrease the $In_2(SO_4)_3$ dissolution rate under GO. There was a smaller peak derived from $In_2(SO_4)_3$ on the InP surface after etching with diluted H_2SO_4, shown in Figure 4-6, indicating that $In_2(SO_4)_3$ dissolved slower in the H_2SO_4-containing solution with a higher concentration of H_2SO_4. Figure 4-7 shows the GO-loaded InP substrate after 4 hour etching in the H_2SO_4-containing solution with a low H_2SO_4 concentration. In this case, the height of areas covered with mono-layer GO was about 10 nm, which is smaller than Figure 4-3(a) and (b) of ca. 100 nm with etching solution containing 17 M H_2SO_4. GO can work as mask at both H_2SO_4 concentration in the etching solution, but the obtained height is lower at diluted H_2SO_4. Therefore, the InP etching reaction under GO was restricted less in the diluted H_2SO_4

etchant. From these results, the reaction rate of $In_2(SO_4)_3$ dissolution in the H_2SO_4-containing solution affected the etching behavior. In the case of the HCl-containing solutions, on the other hand, $InCl_3$ forms on the surface, and the $InCl_3$ can be soluble in the acidic solution[111]. From these results, the stability or the dissolution rate of these intermediate formed on the InP surface during the etching process plays an important role on the behavior of GO-assisted InP etching.

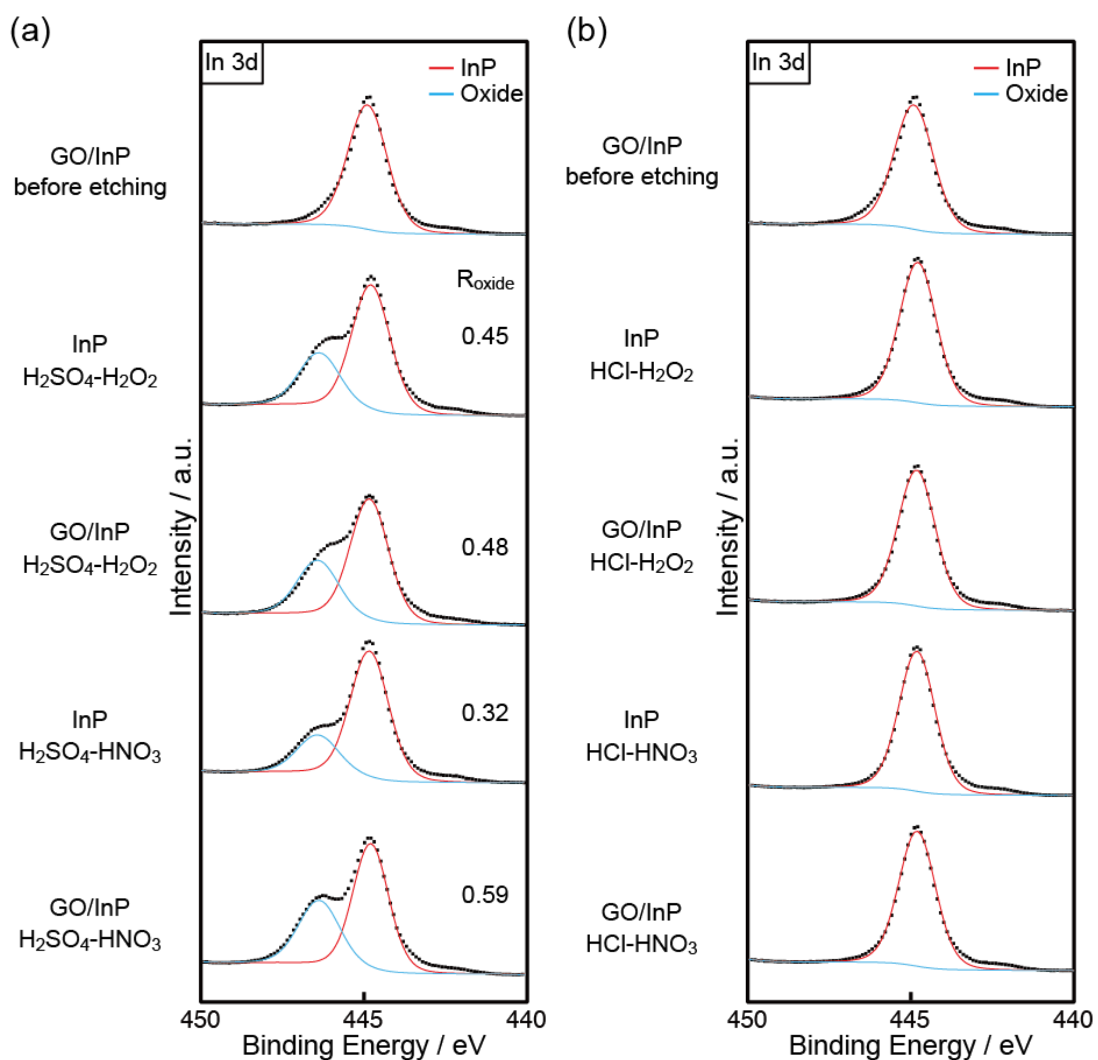

Figure 4-5 XPS In 3d spectra of the InP samples before and after etching for 2 hours in (a) H_2SO_4-containing solution and (b) HCl-containing solution. The molar concentration of the etching solution were the same as described in Figure 4-3.

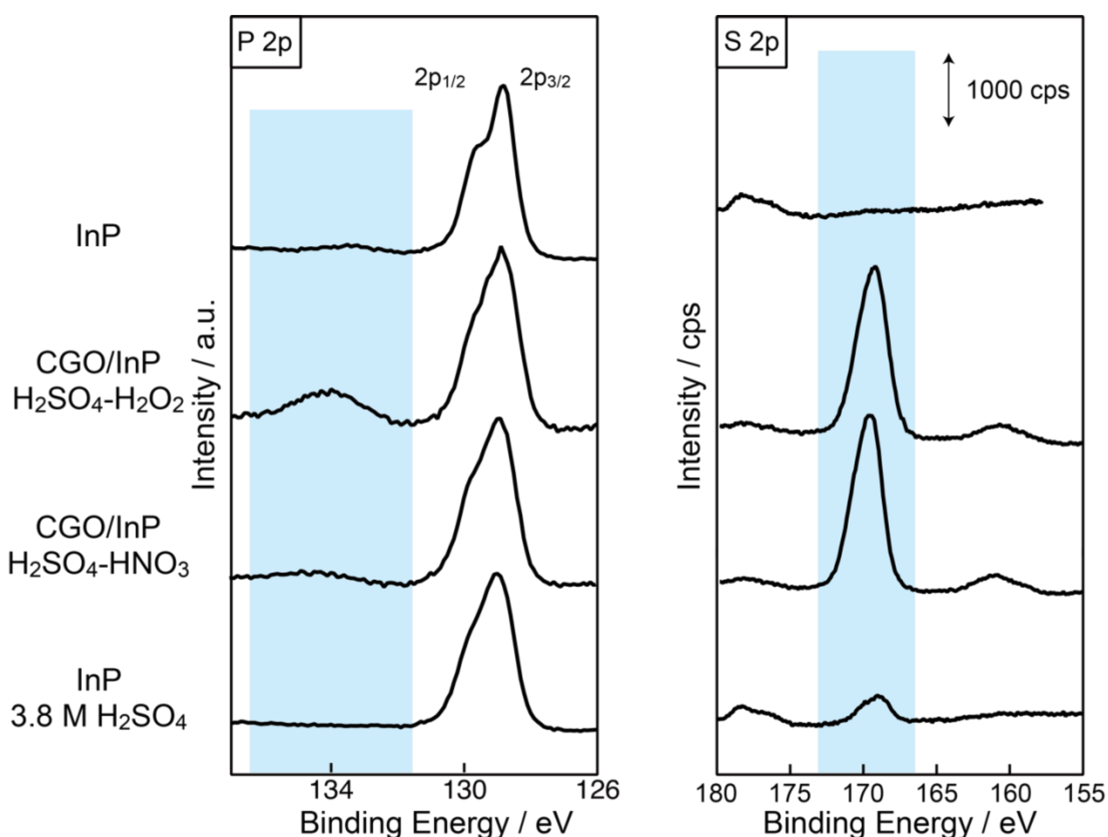

Figure 4-6 XPS P 2p and S 2p spectra of the InP samples before and after etching for 2 hours in H_2SO_4-containing solution. The molar concentration of the etching solution were described in this figure or the same as described in Figure 4-3.

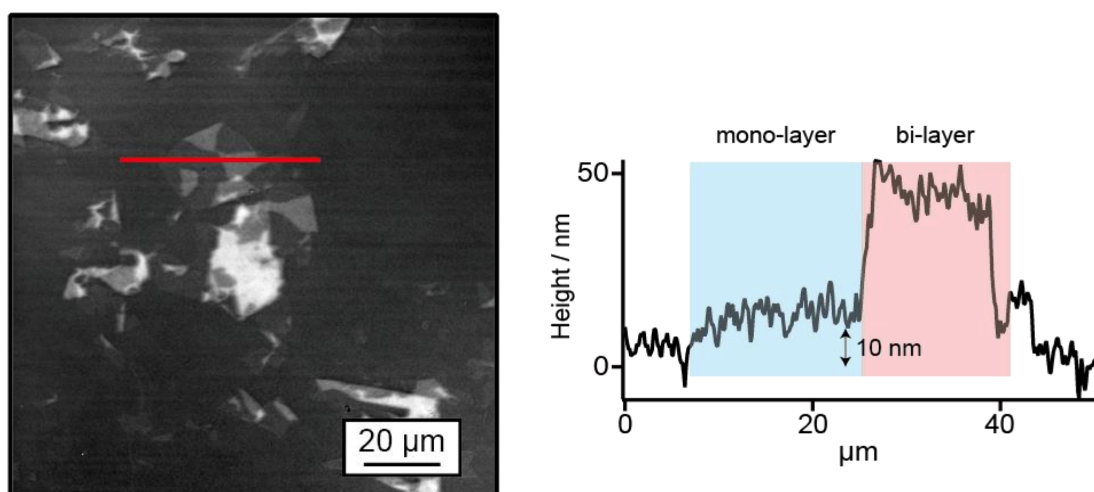

Figure 4-7 A 3D laser microscope topographic image and a cross-sectional profile along the line of the InP substrate loaded with GO sheets after etching at 25°C for 4 hours. The molar concentration of the etching solution was $[H_2SO_4]$:$[HNO_3]$=1.6:1.0 (mol L^{-1})

To the best of my knowledge, two research groups reported metal-assisted chemical etching of InP. Asoh et al. reported the chemical etching of InP assisted by Au, Pd, and Pt in H_2SO_4-H_2O_2 solutions and the effect of ultraviolet (UV) light irradiation during the etching process[17]. Although a shallow groove formed around the loaded metal without UV irradiation, all of the non-covered areas were etched and its etching rate was drastically accelerated with UV irradiation. They suggested that the noble metal catalyst acted as an active center of an electron collector and prevented the recombination of electron-hole pairs created by UV irradiation. In such a condition, the ample holes were able to be consumed by InP oxidation before recombination, which accelerated the InP dissolution in the non-covered areas. Kim et al. reported Pt or Au-assisted InP etching in H_2SO_4-H_2O_2 solutions without UV light irradiation and the XPS surface analysis of the sample after the etching process[18]. They reported that the etching reaction was enhanced only on the non-covered areas, and the inhibition of the etching under the metal catalyst depended on the formation of insoluble oxide at the metal catalyst/InP interface. Furthermore, side etching which was derived from the crystal orientation-dependent anisotropic etching occurred under metal catalysts. They achieved the InP nanofin array formation by utilizing this side etching and by optimizing the etching time precisely.

Combining the GO-assisted etching behaviors and the surface analyses by XPS, a possible mechanism of GO-assisted InP etching in each etchant composition is suggested, shown in Figure 4-8. InP etching reaction with a mixture of an acid and an oxidant is often explained by oxidant reduction and oxidation/dissolution of InP. In the H_2SO_4-containing solution, the oxide layer remained on the sample after etching, indicating that the InP oxide dissolution was the rate-determining step. GO-covered areas generally have a disadvantage in terms of the diffusion of InP oxide compared with non-covered areas and GO worked as a mask in the etching process with the H_2SO_4-containing solutions.

This behavior was also seen in the previous report of GO-assisted silicon etching with HNO_3-rich HF-HNO_3 solution since dissolution or diffusion of byproducts was the rate-determining step[80]. The formation of the thicker InP oxide layer under GO sheets indicated by the XPS analyses also supports the disadvantage of the oxide dissolution under GO sheets. In contrast, the oxide layer was not confirmed when the InP substrates were etched by HCl-HNO_3 solution. This suggests that the oxidant reduction reaction is the rate-determining step in the etching process with the HCl-containing solution. It was reported that GO works as a catalyst for HNO_3 reduction reaction[32]. Because GO enhances the rate-determining step reaction of HNO_3 reduction, InP oxidation and dissolution which occurs simultaneously with HNO_3 reduction is enhanced under the GO-covered area. On the other hand, GO worked as a mask in the etching with the HCl-H_2O_2 solution even though the oxide layer formation was not confirmed from the sample after etching. This may be due to the difference in the catalytic ability of GO towards the oxidant reduction. In the previous chapter, GO-assisted silicon etching in the mixture of HF and oxidants was discussed, and HF-HNO_3 solution dissolved silicon beneath GO sheets faster than HF-H_2O_2 solution which may be due to the catalytic activity towards the oxidant reductions[79,80]. The result of GO-assisted InP etching in this chapter supports this hypothesis that the catalytic activity of GO determines the etching rate under GO sheets and the etching rate was slower under GO sheets than that in the non-covered areas in the case of HCl-H_2O_2 solution. Because GO had lower catalytic activity for H_2O_2 than for HNO_3 reduction, InP etching reaction under the GO sheets was not enhanced in the HCl-H_2O_2 solution significantly, indicating that the disadvantage of byproducts diffusion affects more than GO enhancement of the etching reaction under GO sheets. Further study about the catalytic activity of GO towards oxidant reductions may help further comprehension of the catalytic mechanism of GO-assisted chemical etching of

semiconductor materials. Note that oval etch pits with the size of several μm were seen on the InP surface after etching in HCl-containing solutions, shown in Figures 4-3(c) and (d). The etch pits were oriented parallel to one direction. This is due to the non-uniform etching on the surface dislocation[112]. It was reported that the surface roughening during the etching process can be restricted by lowering the HCl concentration.

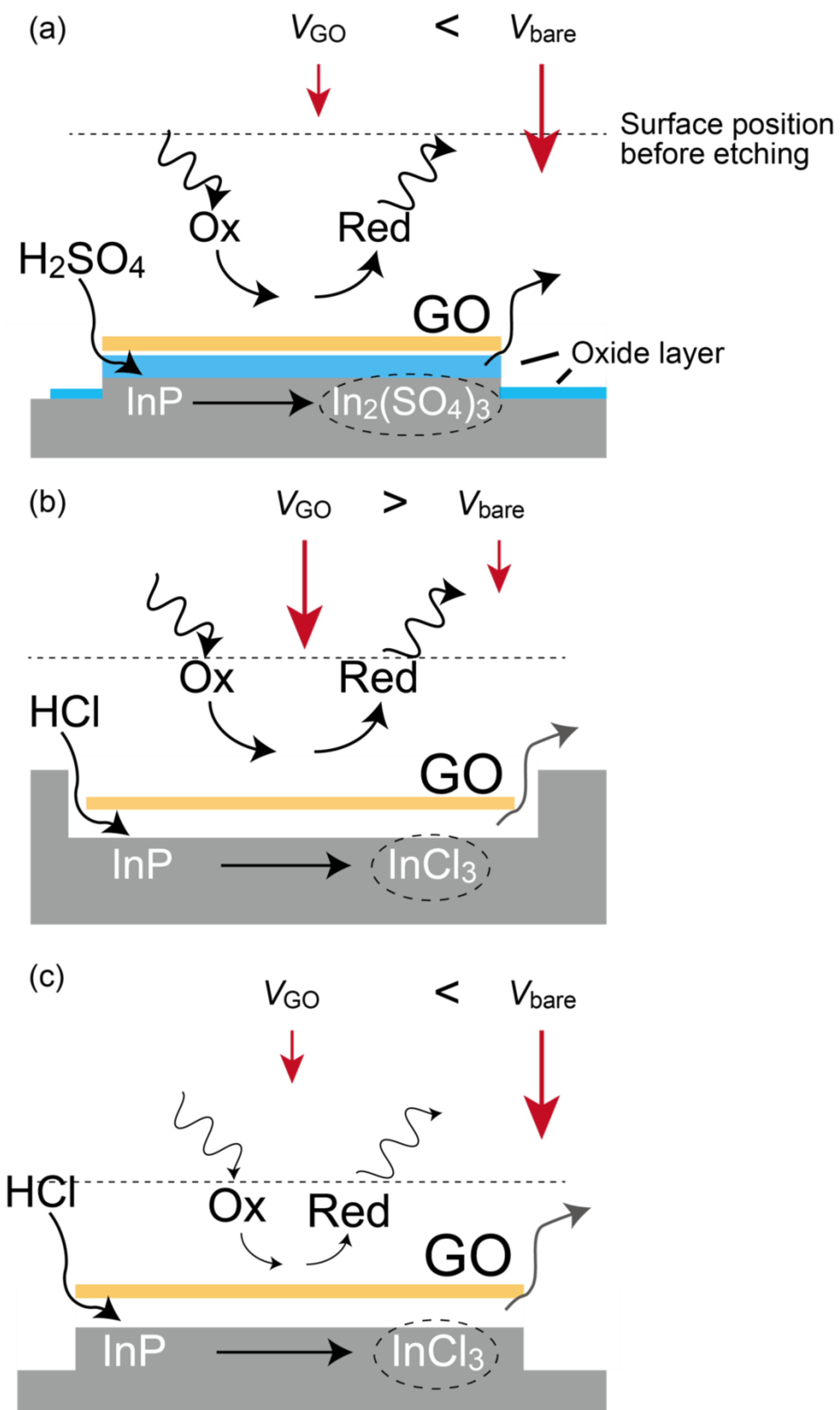

Figure 4-8 Schematic illustrations of GO-assisted InP etching in (a) H_2SO_4-containing solution, (b) HCl-HNO_3 solution, and (c) HCl-H_2O_2 solution.

4.4 Conclusion

In this chapter, the etching behavior of GO-loaded InP substrate in various types of etching solutions was reported. It was revealed that the insoluble oxide layer formed on the InP surface in the H_2SO_4-containing solutions, and the dissolution of the oxide layer was the rate-determining step of the InP etching reaction in the H_2SO_4-containing solutions. Because the area under GO had a disadvantage in the dissolution of the InP oxide layer, the etching reaction under GO was inhibited. On the other hand, the oxide layer was not confirmed on the InP sample after etching in the HCl-containing solutions, which means that the oxidant reduction is the rate-determining step. Furthermore, the etching behavior can be controlled by the kind of oxidants, and the catalytic activity of GO for the oxidant reductions also affects the etching behavior. By choosing HNO_3 as the oxidant, the etching reaction under GO sheets was enhanced. Further optimization of the etching condition is necessary for improving the etching rate and restricting the surface roughening after the etching process.

Chapter 5 Conclusion and outlook

In this thesis, the potential of GO for the catalyst towards the etching reaction of semiconductors was explored, and the mechanism of the etching reaction was discussed.

In chapter 2, GO was applied to the assisted etching of silicon in the liquid phase which is generally reported in the case of metal-assisted chemical etching process. It was revealed that GO promoted the etching reaction of silicon and that its etching rate was different in the solution containing a different oxidant. Then, the reaction mechanism of GO-assisted silicon etching was investigated utilizing an HF-HNO_3 etchant, and a catalytic mechanism for GO-assisted silicon etching was proposed, in which oxidants are more easily adsorbed on the GO structural defects than on the silicon surface, and this difference in adsorption frequency generates a difference in etching rate between the GO-covered and bare areas, resulting in the enhancement of the etching under the GO.

In chapter 3, a vapor phase etching process was applied to the GO-assisted silicon etching. It was shown that the etching reaction under GO was enhanced without the formation of a porous structure by using an appropriate solution as a vapor source. In order to investigate the reaction mechanism in the vapor phase method, the temperature dependence of the reaction rate was confirmed. It was found that the etching rate was saturated at 60°C, suggesting that mass transfer contributed to the rate-limiting process in the vapor phase method. Furthermore, a site-selective etching was demonstrated by combining μCP as a position control of GO. Pattern etching on the order of μm was achieved by vapor phase etching of silicon substrates on which GO patterns were transferred by μCP.

In chapter 4, the chemical etching of InP assisted by GO was demonstrated, and a possible mechanism of GO-assisted InP etching was suggested by combining XPS

analyses. The solubility of the InP oxide layer towards the etching solution affected the rate-determining step of the InP etching reaction. When the oxidant reduction reaction catalyzed by GO was the rate-determining step, the etching reaction under GO was enhanced. Furthermore, the etching behavior was different in utilizing different oxidants, which means that the catalytic activity of GO for the oxidant reduction also affects the etching behavior.

The conclusions of GO-assisted etching of semiconductors discussed in this paper are summarized as follows,

1. When the etching reaction of semiconductors proceeds with oxidant reduction, semiconductor oxidation and those dissolution, GO enhances the etching reaction by adjusting the etchant in which the oxidant reduction is the rate-determining step in the etching reaction.
2. Dissolution behavior of intermediates produced by oxidizing semiconductors in the GO-assisted etching process affects its rate-determining step, and the influence of GO towards the rate-determining step decides its etching behavior.
3. The oxidant utilized as the etchant of GO-assisted etching affects the etching behavior due to the difference in the catalytic activity of GO towards oxidant reduction reaction.

As an outlook of GO-assisted etching of semiconductors, directions for the improvement of this process are suggested as follows,

1. Improvement of catalytic activity of GO by heteroatom doping

Many studies reported the utilization of GO as a catalyst for various types of reactions, and most of them have focused on the enhancement of catalytic activity by doping heteroatoms on GO[42]. In these studies, various reaction processes and catalytic mechanisms of heteroatoms-doped GO were discussed. It is claimed that the electronic state of the heteroatoms-doped GO can easily adsorb and desorb reactive species due to

the disorder in the electronic state of the heteroatoms. As mentioned in this thesis, it was suggested that the structural defects on GO act as active sites and that the reactive species are adsorbed more frequently on the GO than on the silicon substrate. These results suggest that the adsorption sites are expected to increase for heteroatoms-doped GO, and thus this method is useful for improving the etching rate of the assisted etching process.

2. GO-assisted etching of wide-gap semiconductors with the enhancement of anodization or photo-irradiation

Wide-gap semiconductors are applied to power devices with high breakdown voltage and low on-resistance, but their high chemical stability makes their processing difficult. Recently, a photoelectrochemical etching, which combines electrochemistry and light irradiation, has attracted much attention as a wide-gap semiconductor processing[21,113–115]. This process suggested that the production of hole-electron pairs helps the etching reaction of wide-gap semiconductors which hardly occurs only by immersing in the mixture of acids and oxidants. The driving force of anodization or photo-irradiation will enable the assisted etching of wide-gap semiconductors. The advantage of GO compared with other metal materials is that GO can control its own band structures by adjusting its structures[116]. The charge transfer from the etchant through GO into the semiconductor is necessary for enhancing the etching reaction with oxidant reduction and semiconductor oxidation. The control of GO band structure enables the charge transfer so that GO can enhance the etching reaction easier than metal materials.

Appendix Local current mapping of electrochemically-exfoliated graphene oxide by conductive AFM

A.1 Introduction

Graphene is drawing much attention due to its outstanding properties of high electrical conductivity[117], mechanical strength[118], thermal conductivity[119], and so on. Many researchers have been making efforts not only to reveal its physical and chemical properties for several applications, for example, bio-sensor[40], transparent conductors[120], and supercapacitors[39], but also to produce it on a large scale cost-effectively. For the synthesis of graphene, there are various types of methods such as mechanical exfoliation, chemical vapor deposition (CVD)[121], epitaxial growth[122], and reduction of graphene oxide (GO)[123]. In the case of CVD or epitaxial growth, high-quality graphene can be synthesized. However, it is inevitable for the graphene synthesized by the CVD process or epitaxial growth to transfer to the desired substrates[124] and it is not suitable for the mass production of graphene. On the other hand, GO can be fabricated by graphite oxidation, and, moreover, GO sheets can be dispersed in water or some organic solvents owing to epoxide, hydroxyl and carboxyl groups on GO sheets[37]. Hence GO can be directly loaded on the substrate by a simple and inexpensive solution process. As a method of GO reduction, many methods are suggested, such as chemical reduction by strong reductant of hydrazine, thermal reduction, and photochemical reduction. In the previous report, Tu suggested GO reduction process by vacuum ultraviolet irradiation in a high vacuum ($<10^{-3}$ Pa) condition and the reaction mechanism. This photochemical reaction process has some merits for practical application because

Although the oxygen functional groups on GO sheets are removed after VUV reduction process, the reduced GO has lower electrical conductivity than reduced GO by other

processes such as thermal reduction or chemical reduction and the reason for this low electrical conductivity is still unclear.

The electrical property of reduced GO is inferior to that of graphene synthesized by other processes because there are many defects on the GO sheets formed during the oxidation process, and these defects in the GO sheets can not be repaired easily by the reduction process, which deteriorates the performance of reduced GO.

Recently, a new method to synthesize GO has been focused on, that is, the exfoliation of graphite by anodization. When the positive voltage was applied to graphite in the electrolyte of some aqueous solution of sulfates[44,125–127], alkali halide[128] or ionic liquid[129], ions or water molecules were inserted into the graphite layers, and then graphite was exfoliated into multi or mono-layer GO sheets by the gas pressure produced by intercalated species decomposition. In this process, it takes less than 1 hour for the graphite exfoliation, so GO can be synthesized rapidly. Furthermore, there are fewer defects on electrochemically-exfoliated GO (EGO) than that synthesized by a chemically oxidized process, for example, Hummers method because graphite is moderately oxidized without strong oxidant in a short reaction time.

The electrical property of graphene-like materials is very important for their practical application in electronics. It is often reported that oxygen functional groups or defects on the GO sheet degrade its electrical property by the chemical and structural analysis of the X-ray photoelectron spectroscopy[130] or Raman spectroscopy[131] and the sheet resistance of stacked GO films. However, by these instruments, the obtained information is spatially averaged and the local electrical property can not be measured directly. Scanning probe microscopy proved to be useful for studying local properties. As the micro/nano-scale electrical measurement, conductive atomic force microscopy (C-AFM) has been developed to evaluate the electrical properties of semiconductor materials[132] or carbon

nanomaterials such as carbon nanotube[133,134] and reduced graphene oxide[135136]. In this method, local electrical conductivity can be evaluated by mapping the local current with the voltage-applied AFM cantilever.

In this chapter, the C-AFM measurement was applied to EGO or EGO reduced by the irradiation of VUV light for the observation of its electrical property. Additionally, associated with the analysis by XPS and μRS, the relationship between EGO structure and the electrical property is discussed and the possible mechanism of VUV reduction is suggested.

A.2 Experimental procedure

A.2.1 Synthesis of electrochemically-exfoliated GO and reduction by vacuum ultraviolet light irradiation in high vacuum condition

Electrochemically-exfoliated GO was synthesized referred to Cao's report, which is a two-step electrochemical exfoliation process[44]. Figure A-1(a) shows the schematic image of the electrochemical apparatus. Galvanostatic charging was applied to graphite foil (99.8%, Alfa Aesar, 0.5 mm thickness) in a two-electrode cell with a platinum wire as cathode and concentrated H_2SO_4 (97 %, Nacalai Tesque) as the electrolyte. The charging current was kept at 100 mA for 20 min. For the second electrochemical step, the graphite foil was removed in the first electrolyte and potentiostatic charging was applied to the foil in a two-electrode cell with a platinum wire as cathode and 0.1 M $(NH_4)_2SO_4$ (99%, Fujifilm Wako Pure Chemical Corp.) aqueous solution as the electrolyte. The charging voltage was kept at 10 V for around 10 min to exfoliate completely. Then the exfoliated graphite flakes were sonicated for 5 min and centrifuged for 10 min to remove the impurity including $(NH_4)_2SO_4$. After purification, the dispersion was maintained for 24

hours to precipitate and remove any aggregations.

The obtained CGO and EGO sheet was loaded on the silicon substrate by spin-coating. Then the GO-coated substrate was irradiated by VUV light (Ushio) in a high vacuum (<10^{-4} Pa) for 64min.

A.2.2 Conductive AFM measurement

AFM and C-AFM measurements were performed under ambient conditions using MFP-3D (Oxford Instruments). Rh-coated Si cantilevers (Hitachi High-Tech, SI-DF3-R, spring const. 1.6 N m^{-1}) were employed for current mapping in contact mode. Al-backside-coated Si cantilevers (Hitachi High-Tech, SI-DF40, spring const. 35 N m^{-1}) were used for amplitude modulation (AM) AFM topographic imaging. During C-AFM measurement, a force of 35 nN was maintained, and -1 V was applied to the cantilever. For an electrode to connect the sheet, Au/Ti film (100 nm Au and 10 nm Ti) was deposited on a part of the GO-coated substrate as shown in Figure A-1(b).

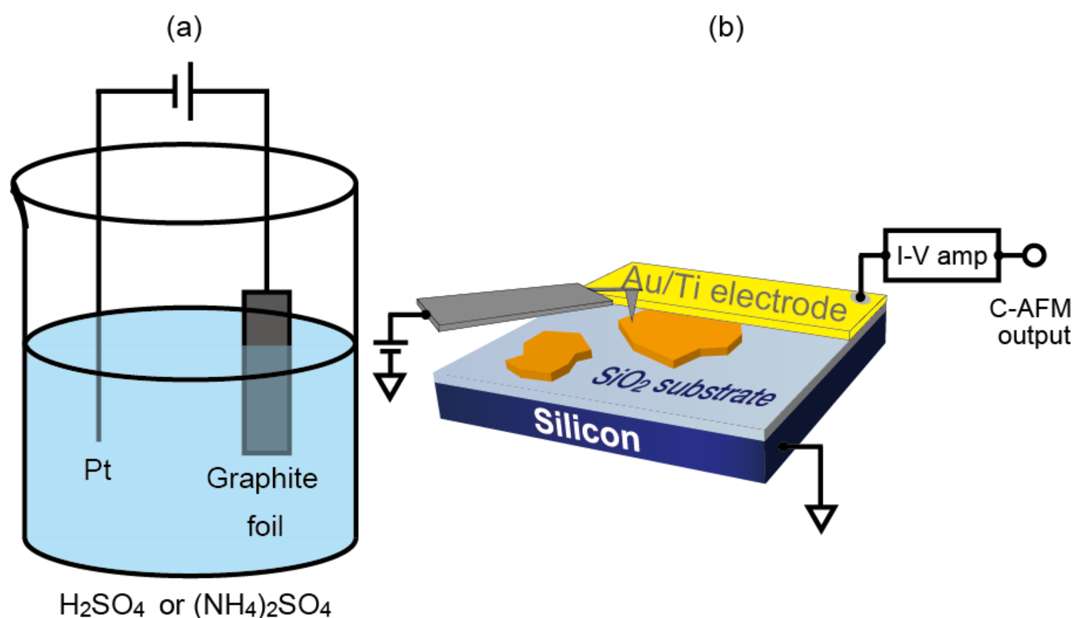

Figure A-1 Schematic images of (a) the electrochemical exfoliation of graphite and (b) the C-AFM measurement.

A.3 Results and discussion

A.3.1 Characterization of electrochemically-exfoliated GO

Figure A-2(a) and (b) show the graphite products after each step of anodization. After the first step of the anodization (100 mA for 20 min in concentrated H_2SO_4), the immersed part of the graphite foil was expanded, which implies that sulfates were intercalated between layers of graphite. After the second step of anodization (10 V in 0.1 M $(NH_4)_2SO_4$), the graphite intercalated compounds were peeled into small flakes as shown in Figure A-2(b). Notably, the solution after electrochemical exfoliation was transparent. After the second step of the electrochemical treatment, the solution with flake-like products was sonicated. Figure A-2(c) shows the solution after sonication and then kept for 1 day. Unlike just after electrochemical processes, the color of the supernatant has changed into brown by the sonication. This color change suggested the existence of dispersed GO sheets. The EGO sheet loaded on the silicon substrate was observed by AFM to confirm the number of layers and the size of EGO sheet, as shown in Figure A-2(d). The thickness was 1 nm, which means that EGO sheet was mono-layer[47].

Several researchers have reported the one-step synthesis of electrochemically-exfoliated GO in different conditions[126,127,129]. In these graphite anodization processes, the high positive voltage of around 10 V is applied in the aqueous solution of sulfate to insert the anions into the graphite layers and to produce gases by water decomposition to oxygen simultaneously. The obtained GO sheets after these anodization processes are usually multi-layer because graphite is exfoliated before sufficient sulfate intercalation. By the two-step anodization, sulfate was adequately inserted into graphite at the first step of anodization in concentrated sulfuric acid without water decomposition, and these graphite intercalated compounds were further anodized in the aqueous solution of ammonium sulfate for the exfoliation. Remarkably, the graphite could not be separated

into GO sheets immediately after anodization, as shown in Figure A-2(b), which means that the role of two-step anodization was broadening the distance and weakening the interaction between each graphite layer, and the obtained graphite products were physically exfoliated by sonication.

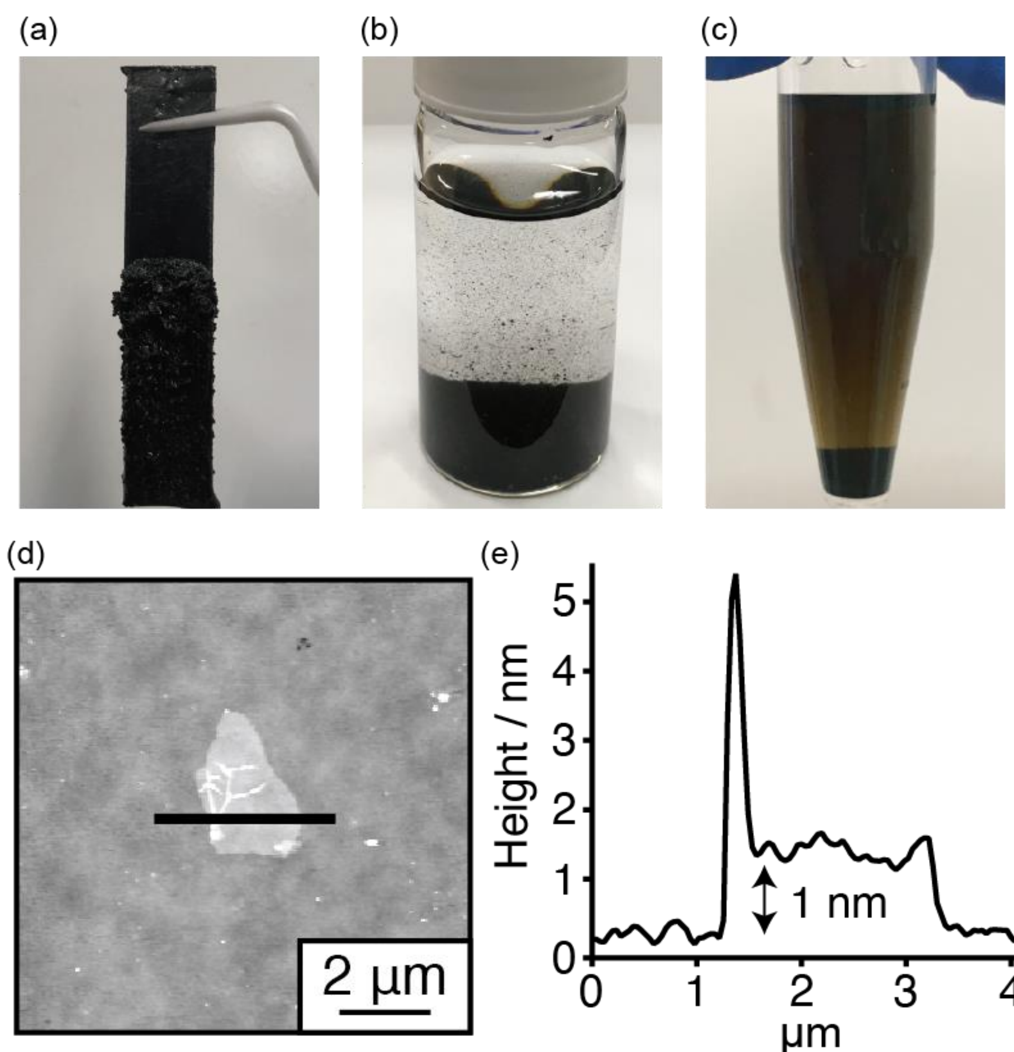

Figure A-2 The photographs of graphite products (a) after the first anodization (100 mA for 20 min in concentrated H_2SO_4), (b) after the second anodization (10 V for 10 min in 0.1 M $(NH_4)_2SO_4$), and (c) after sonication. (d) AFM topographic image and (e) the cross-sectional profile along the line of the EGO sheet on the SiO_2/Si substrate.

The difference in chemical conditions and oxygen functional groups attached to each GO sheet was determined by the XPS analysis. Figure A-3(a) shows the XPS C 1s spectra obtained from each GO sheet. The spectra were calibrated to the Si 2p peak at 103.5 eV derived from the Si-O bond. Furthermore, C 1s spectra were deconvoluted to 6 peaks, i.e., sp^2 C=C at 284.4 eV, sp^3 C-C at 285.0 eV, C-OH at 286.2 eV, C-O-C at 286.9 eV, C=O at 287.9 eV, and COOH at 289.1 eV following the previous report[136]. From the peak fitting result, the percentage of the chemical moieties (P_i) and the ratio of oxygen to carbon ($R_{O/C}$) on GO sheets were shown in Table I. The $R_{O/C}$ was calculated by the equation below:

$$R_{O/C} = \frac{P_{C-OH} + \frac{1}{2}P_{C-O-C} + P_{C=O} + 2P_{COOH}}{P_{C=C} + P_{C-C} + P_{C-OH} + P_{C-O-C} + P_{C=O} + P_{COOH}} \quad (1)$$

There was little difference between the $R_{O/C}$ of ca. 0.40 for CGO and EGO. However, the main oxygen functional group on EGO was the hydroxyl group, whereas that on CGO was the epoxide group. This difference can be attributed to the oxidation and exfoliation process of each GO and may change the electrical property of each GO sheet. After VUV reduction, $R_{O/C}$ of RCGO and REGO were also almost the same. This means that oxygen functional groups on both CGO and EGO were removed by VUV irradiation in a high vacuum although the kind of oxygen functional groups on each GO was different.

Raman spectroscopy is one of the powerful tools to characterize the structure of graphene-like materials. The Raman spectra of both GO sheets were shown in Figures A-3(b) and (c). In the spectra, there were two clear peaks derived from GO sheets, one was around 1350 cm^{-1} called D peak and the other was around 1600 cm^{-1} called G peak[137]. Slight differences were found in these two spectra, such as the position of G peak and the

intensity of D peak. At first, G peak of GO sheets is the combination of two peaks, that is, G peak derived from the graphitic lattice around 1580 cm^{-1} and D' peak by the disorder-induced graphitic structure around 1610 cm^{-1} [138]. In comparison with the CGO spectrum, the peak around 1600 cm^{-1} of EGO was red-shifted due to the D' peak weakening, which means that EGO sheets had fewer defects than CGO. Next, D peak, which is derived from the breathing modes of six-atom rings, requires a defect for its activation. In the discussion about the structure of graphene-like materials by Raman spectra, the ratio of D peak and G peak intensity (I_D/I_G) and the width of peaks are common parameters. Generally, when the defects at GO sheet are repaired, all of the peaks become sharp, the intensity of G peak increase, and that of D peak decrease. However, it is reported that the intensity of D peak decreases when the defect density at GO sheets increases and the distance between defects decreases to less than 5 nm. This is due to the breakdown of the six-atom rings lattice structure area, which is the origin of D peak[68]. It is confirmed that EGO has a sharper D peak and higher I_D/I_G value than those of CGO, which indicates that EGO had a highly ordered structure. Compared with the spectra of RCGO and REGO, the difference is more apparent than the difference between CGO and EGO. D peak of REGO was sharper and the intensity of D peak was higher than that of RCGO. Furthermore, the G peak of REGO was split into two peaks called G peak and D' peak. There was less difference between CGO and EGO than that between RCGO and REGO because the oxygen functional groups on the EGO sheet prevent the activity of its graphitic structure. From these chemical analyses, EGO has an ordered structure more than CGO.

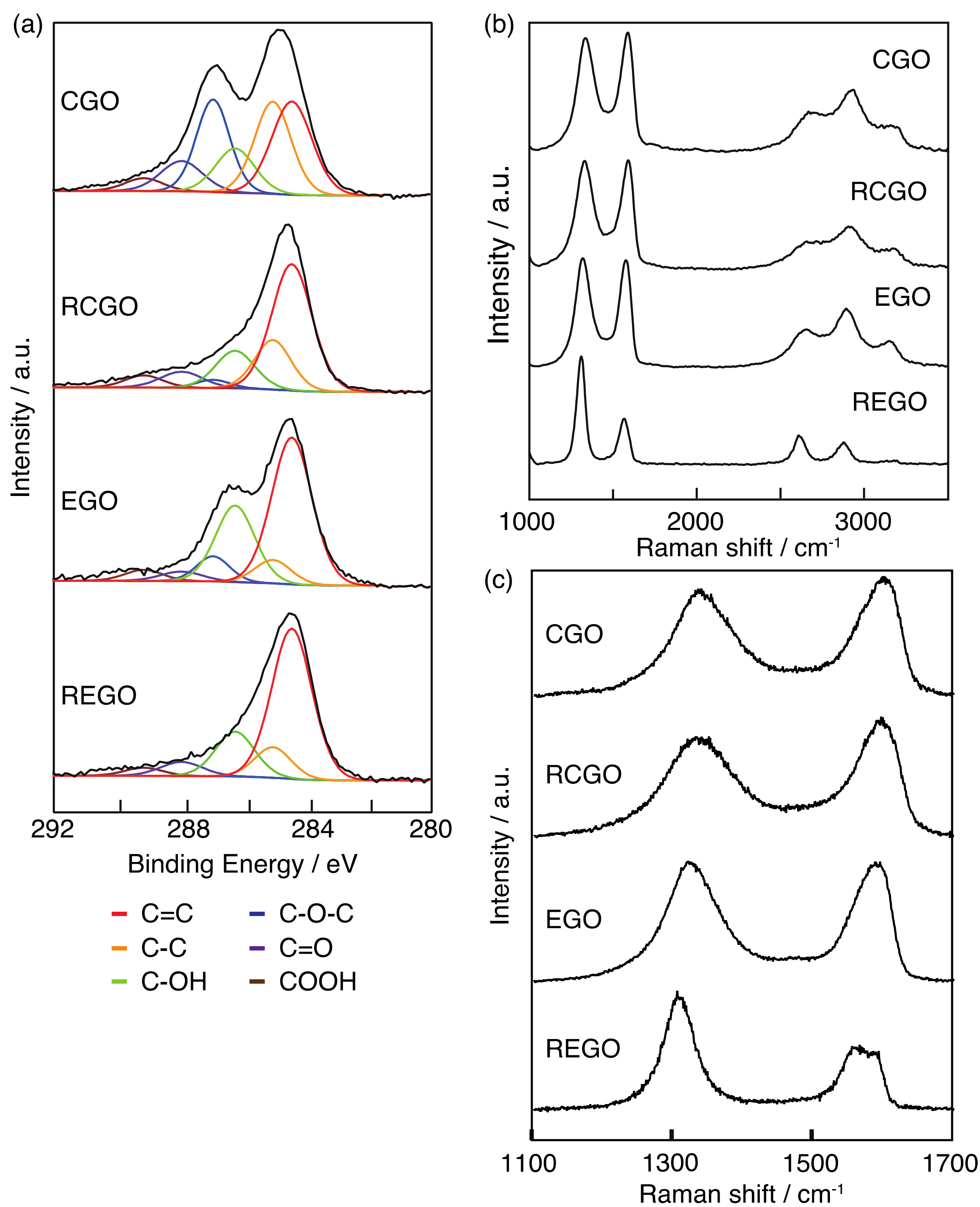

Figure A-3 (a) Comparison of chemical and structural characteristics of each GO sheet (a) XPS C1s spectra and (b)(c) Raman spectra.

A.3.2 Local current mapping of electrochemically-exfoliated GO

Local electrical conductivity of EGO and REGO was measured by C-AFM in contact mode as shown in Fig. A-4(a) and (b). EGO sheets were deposited on the thermally-grown SiO_2 (300 nm thickness) surface, which is an insulator. After the Au/Ti electrode deposition, C-AFM measurements were performed at the boundary region of the Au/Ti electrode in order to obtain the current mapping images of EGO and REGO connected to the electrode. Therefore, the C-AFM configuration in this study can detect the current flowing through the EGO sheet laterally. The upper white region in Fig. A-4(a) and (b), which showed a current of more than 20 μA, is the area of the deposited Au/Ti electrode. The black region where the current was detected as less than 1 μA can be the exposed SiO_2, the EGO sheets without connection to Au/Ti electrode, or the position in a connected EGO sheet with current below the detection limit. Most of the grey regions were GO sheets connected to the electrode. In these regions, the detected current gradually decreased as the distance from the electrode increased due to the integrated resistivity of the EGO sheet. The current signals in both GO sheets showed the variation at a certain distance from the electrode and formed domain-like parts in the current mapping image. Domain features of current mapping reflected the inhomogeneous local conductivity of GO sheets. When the probe was placed on the low-conductive domain, the current flows through the low-conductive domain at first, leading to the low-current signal. On the other hand, when the tip is contacted with the high-conductive domain, current flows only through the conductive path in the EGO sheet to the electrode, leading to a higher current signal, shown in Figure A-5. This difference resulted in the variation of the measured current in an EGO sheet, and the formation of high- and low-conductive domains in Fig. A-4(a) and (b). The low conductive domains derive from the EGO's structural feature. As shown in Fig. A-3, EGO sheets have some oxygen functional groups

and defects which were formed in the synthesis process, and those parts should have lower electrical conductivity than the graphitic domain.

Figure A-4(a) and (b) also shows the current profile and the corresponding resistance profile following Ohm's law. Judging from Fig. A-4(a) and (b), the intercept value of EGO was 90 kΩ and that of REGO was 420 kΩ, which means the contact resistance at GO-electrode and GO-probe contacts. In the previous report, the contact resistance between graphene and Cr/Au electrode was measured by 2 and 4-probe measurements. The measured contact resistance ranged from 10^3 to 10^6 Ω μm[139]. The resistance order was almost the same as the C-AFM results at this time. Furthermore, the measured current was inverse proportion to the distance from the electrode to the measured point except for the low-conductive domains, which means that current detours in order to avoid the defects as shown in Figure A-5. These results indicate that the current measurement was not restricted by the contact resistance but the detected current reflected the resistance of each GO sheet. Regarding the triangle region on EGO sheet formed by the tip and the electrode side connected with EGO sheet as the electrical conduction path, the electrical conductivity can be calculated by utilizing the relation between resistance and distance[140]. The resistance of the micro area surrounded by the dashed line in Figure A-4(c) is given by

$$dR = \rho \frac{dx}{\left\{\frac{x}{L}(W_{\mathrm{e}} - W_{\mathrm{t}}) + W_{\mathrm{t}}\right\}T} \tag{2}$$

where ρ is the resistivity of the EGO sheet, L is the distance between the tip and the electrode, T is the thickness of the sheet, W_e is the connected length between the sheet and the electrode, and W_t is the diameter of the tip contact area. The contact area of the tip and EGO sheet was estimated to be 13.3 nm^2 by following the Hertzian contact mechanics model and W_t was evaluated to be 4 nm. Then, the electrical conductivity σ of the sheet

was calculated by integrating the Eq. (2) and converting ρ as σ, that is,

$$\sigma = \frac{L}{R}\frac{\ln\left(\frac{W_e}{W_t}\right)}{T(W_e - W_t)} \tag{3}$$

By using the experimental parameters of W_e as 1.7 μm and L/R as 0.13 MΩ μm^{-1} which is approximate to the fitting result shown in Figure A-4(a) except for the low-conductive domains, the calculated electrical conductivity of the right side of EGO sheet was about 27000 S m^{-1}, which was similar to that of reduced EGO membrane in Cao's report[44]. In the previous report, the C-AFM measurement of reduced CGO demonstrated its electrical conductivity and the existence of low-conductive domains with the size of several tens to hundreds of nanometers. The calculated electrical conductivity was 0.2 S m^{-1} [47]. Despite some quantity of oxygen functional groups on EGO sheets, EGO was proved to be more conductive than reduced CGO. The same calculation was applied to REGO. By using the experimental parameters of W_e as 7.3 μm and L/R as 0.12 MΩ μm^{-1} which is approximate to the fitting result shown in Figure A-4(b) except for the low-conductive domains, the calculated electrical conductivity of the right side of EGO sheet was about 8300 S m^{-1}. which was lower than that of EGO.

From the chemical and structural characterization and the local electrical conductivity, the possible theory of the relationship between the structure and the electrical property of the GO sheet can be proposed. The main factor of the high electrical conductivity of EGO is owing to the ordered graphitic structure. EGO sheets have fewer defects than CGO, which was revealed by Raman spectroscopy. Generally, the electrical path is the sp^2 domains on the sheet, and this domain can be destroyed by strong oxidants such as $KMnO_4$ or nitric acid in the fabrication process of CGO. On the other hand, EGO was prepared by moderate oxidization of graphite and it was completely exfoliated by an electrochemical process, which leads to the ordered structure. Additionally, the types of

oxygen functional groups may affect the electrical conductivity of both GO sheets. From the XPS spectra, the species of oxygen functional groups on each GO were proved to be different although the $R_{O/C}$ was almost the same. The main oxygen functionality on CGO was epoxide which was connected to the in-plane of the sheet according to the Lerf-Klinowski model[141], hence conductive path was separated. In contrast, the main oxygen-containing group on EGO was the hydroxyl group. Ghaderi et al. reported that it is stable for the hydroxyl group to connect to the defect, disordered, or edge parts of the sheet confirmed by density functional theory simulation[142]. Because hydroxyl groups on EGO sheets do not connect to the graphitic domain which is the conduction path on the sheet, EGO sheets have higher electrical conductivity than CGO. However, the electrical conductivity of REGO was lower than that of EGO. From these results, a possible mechanism of the VUV-irradiated reduction reaction in a high vacuum. Because hydroxyl groups on EGO were connected to defect, disordered or edge parts on EGO, graphitic domains which enhance the G band of Raman scattering increased. However, even if hydroxyl groups were removed from EGO, EGO has another electrical path other than defects or disordered structures. Furthermore, by irradiating VUV light in a high vacuum condition, the adsorbed water on GO was also excited by VUV light, and OH radicals were formed, which destroyed the graphitic structures of EGO. This destruction by VUV irradiation deteriorated the electrical conductivity of EGO. Hirotomi et al. achieved the synthesis of EGO with higher electrical conductivity by the thermal-enhanced VUV reduction in a high vacuum[143]. The adsorbed water on GO sheets can decrease in higher temperature conditions, and EGO structure was not destroyed less in the case of less adsorbed water on EGO in thermal-enhanced VUV irradiation than at R.T. Their results also supported the proposed mechanism of destroying the structure by adsorbed water in the EGO sheets.

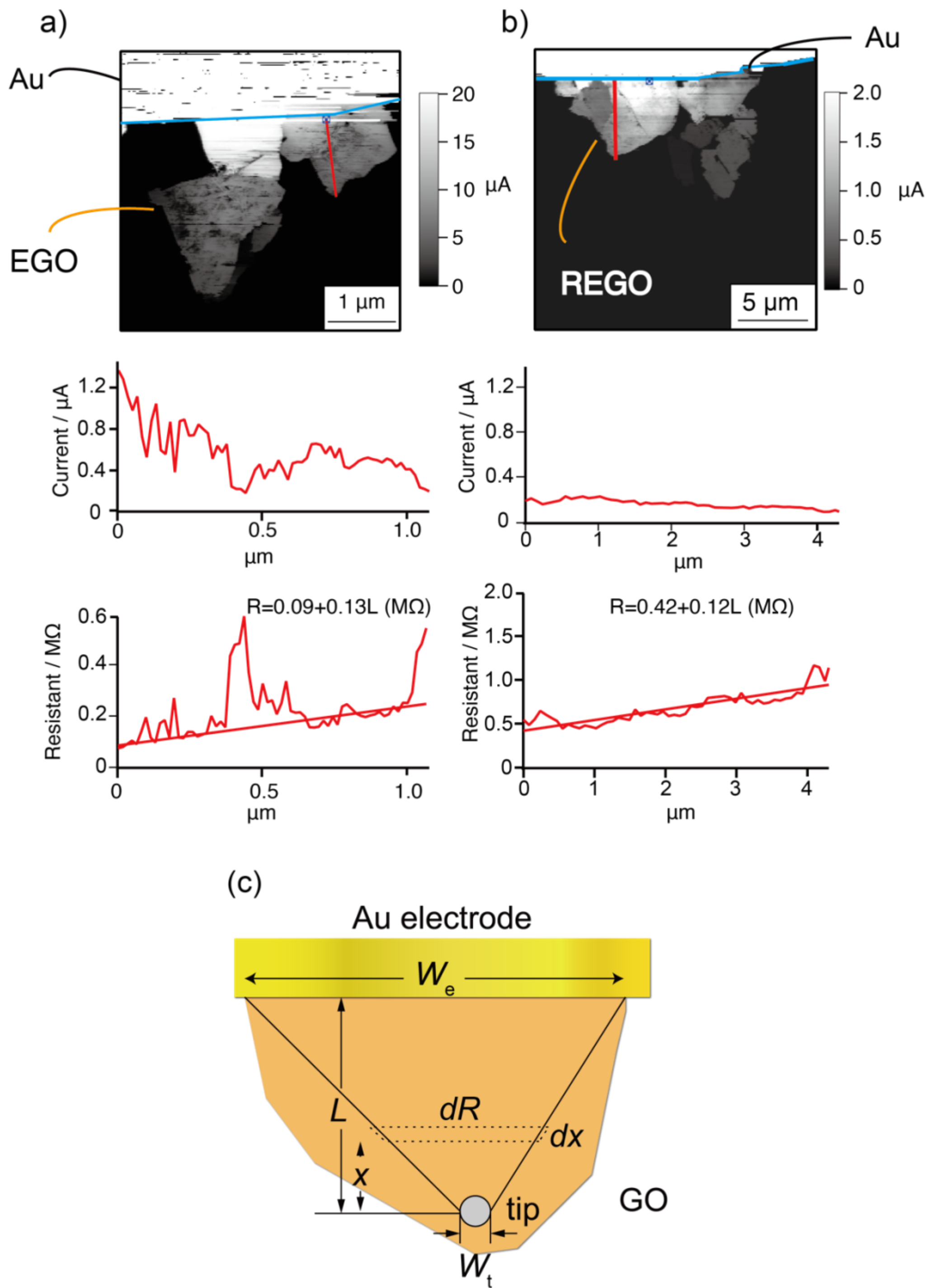

Figure A-4 Local current mapping, current and corresponding resistance profile along lines of (a) EGO and (b)REGO to the Au/Ti electrode with the tip voltage of -1 V. (c) A schematic image of C-AFM measurement for estimating the electrical conductivity of GO.

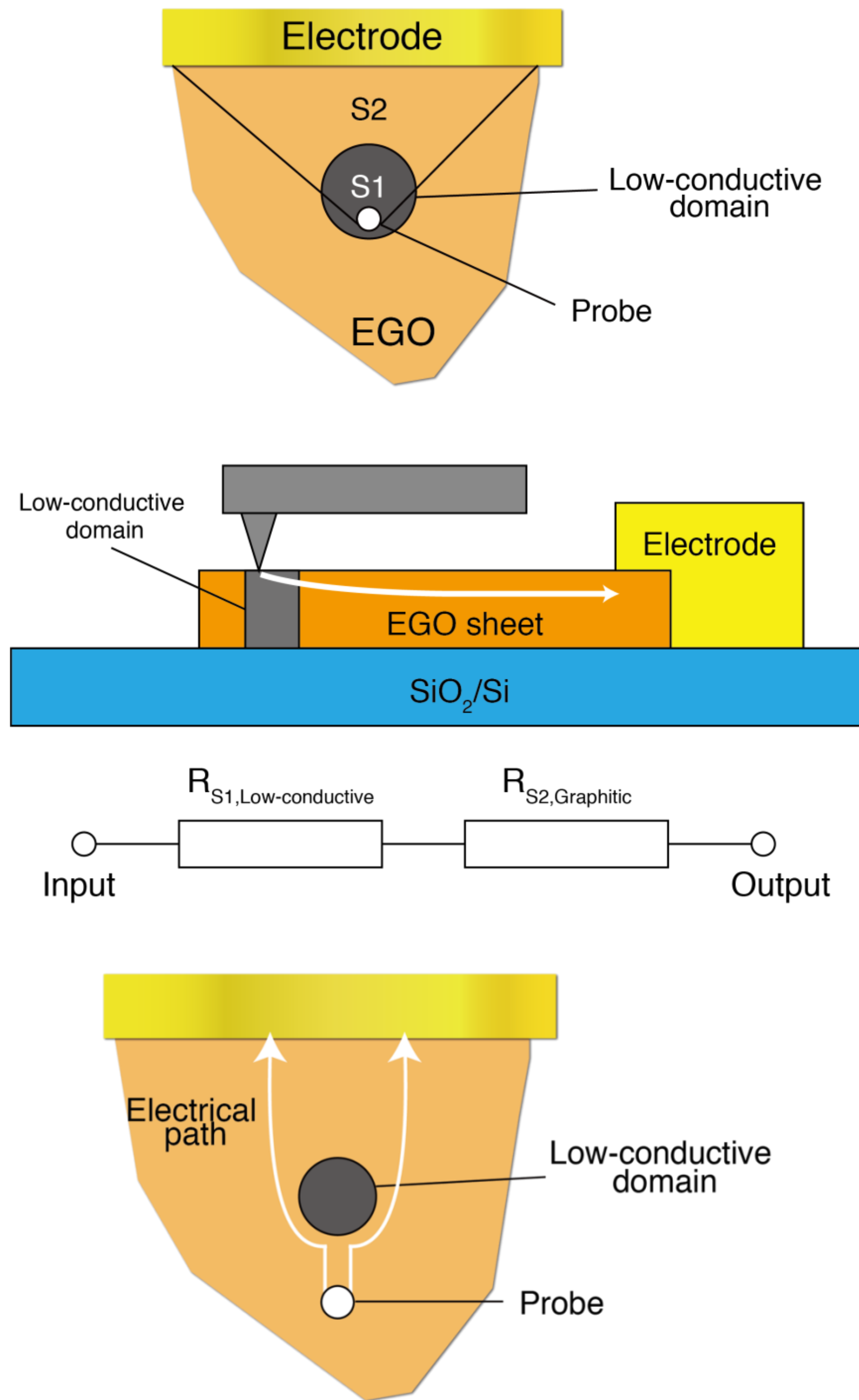

Figure A-5 Schematic images of the conduction path when the probe was placed on the low-conductive domain or the high-conductive domain.

References

(1) Bardeen, J.; Brattain, W. H. The Transistor, A Semi-Conductor Triode. *Phys. Rev.* **1948**, *74*, 230–231.

(2) Samavedam, S. B.; Ryckaert, J.; Beyne, E.; Ronse, K.; Horiguchi, N.; Tokei, Z.; Radu, I.; Bardon, M. G.; Na, M. H.; Spessot, A.; Biesemans, S. Future Logic Scaling: Towards Atomic Channels and Deconstructed Chips. In *2020 IEEE International Electron Devices Meeting (IEDM)*; IEEE, 2020; Vol. 2020-December, pp 1.1.1-1.1.10.

(3) Monzio Compagnoni, C.; Goda, A.; Spinelli, A. S.; Feeley, P.; Lacaita, A. L.; Visconti, A. Reviewing the Evolution of the NAND Flash Technology. *Proc. IEEE* **2017**, *105*, 1609–1633.

(4) Jurczak, M.; Collaert, N.; Veloso, A.; Hoffmann, T.; Biesemans, S. Review of FINFET Technology. In *2009 IEEE International SOI Conference*; IEEE, 2009; pp 1–4.

(5) Yin, X.; Yang, H.; Xie, L.; Ai, X. Z.; Zhang, Y. B.; Jia, K. P.; Wu, Z. H.; Ma, X. L.; Zhang, Q. Z.; Mao, S. J.; Xiang, J. J.; Zhang, Y.; Gao, J. F.; He, X. B.; Bai, G. B.; Lu, Y. H.; Zhou, N.; Kong, Z. Z.; Zhang, Y.; Zhao, J.; Ma, S. S.; Xuan, Z. H.; Zhu, H.; Li, Y. Y.; Li, L.; Zhang, Q. H.; Han, J. H.; Chen, R. L.; Qu, Y.; Yang, T.; Luo, J.; Li, J. F.; Yin, H. X.; Wang, G. L.; Radamson, H.; Zhao, C.; Wang, W. W.; Ye, T. C.; Li, J. J.; Du, A. Y.; Li, C.; Zhao, L. H.; Huang, W. X. Vertical Sandwich Gate-All-Around Field-Effect Transistors with Self-Aligned High-k Metal Gates and Small Effective-Gate-Length Variation. *IEEE Electron Device Lett.* **2020**, *41*, 8–11.

(6) Cui, Y.; Zhong, Z.; Wang, D.; Wang, W. U.; Lieber, C. M. High Performance Silicon Nanowire Field Effect Transistors. *Nano Lett.* **2003**, *3*, 149–152.

(7) Kim, J.; Han, H.; Kim, Y. H.; Choi, S.-H.; Kim, J.-C.; Lee, W. Au/Ag Bilayered Metal Mesh as a Si Etching Catalyst for Controlled Fabrication of Si Nanowires. *ACS Nano* **2011**, *5*, 3222–3229.

(8) He, Y.; Fan, C.; Lee, S. T. Silicon Nanostructures for Bioapplications. *Nano Today* **2010**, *5*, 282–295.

(9) Cui, Y.; Wei, Q.; Park, H.; Lieber, C. M. Nanowire Nanosensors for Highly Sensitive and Selective Detection of Biological and Chemical Species. *Science* **2001**, *293*, 1289–1292.

(10) Oh, J.; Yuan, H. C.; Branz, H. M. An 18.2%-Efficient Black-Silicon Solar Cell Achieved through Control of Carrier Recombination in Nanostructures. *Nat. Nanotechnol.* **2012**, *7*, 743–748.

(11) Wagner, R. S.; Ellis, W. C. Vapor-Liquid-Solid Mechanism of Single Crystal Growth. *Appl. Phys. Lett.* **1964**, *4*, 89–90.

(12) Jansen, H.; Gardeniers, H.; De Boer, M.; Elwenspoek, M.; Fluitman, J. A Survey on the Reactive Ion Etching of Silicon in Microtechnology. *J. Micromechanics Microengineering* **1996**, *6*, 14–28.

(13) Barillaro, G.; Nannini, A.; Piotto, M. Electrochemical Etching in HF Solution for Silicon Micromachining. *Sensors Actuators, A Phys.* **2002**, *102*, 195–201.

(14) Li, X.; Bonn, P. W. Metal-Assisted Chemical Etching in HF/H2O2 Produces Porous Silicon. *Appl. Phys. Lett.* **2000**, *77*, 2572–2574.

(15) Chen, Y.; Li, L.; Zhang, C.; Tuan, C. C.; Chen, X.; Gao, J.; Wong, C. P. Controlling Kink Geometry in Nanowires Fabricated by Alternating Metal-Assisted Chemical Etching. *Nano Lett.* **2017**, *17*, 1014–1019.

(16) Tsujino, K.; Matsumura, M. Helical Nanoholes Bored in Silicon by Wet Chemical Etching Using Platinum Nanoparticles as Catalyst. *Electrochem. Solid-*

State Lett. **2005**, *8*.

(17) Asoh, H.; Yokoyama, T.; Ono, S. Formation of Periodic Microbump Arrays by Metal-Assisted Photodissolution of InP. *Jpn. J. Appl. Phys.* **2010**, *49*, 0465051–0465055.

(18) Kim, S. H.; Mohseni, P. K.; Song, Y.; Ishihara, T.; Li, X. Inverse Metal-Assisted Chemical Etching Produces Smooth High Aspect Ratio InP Nanostructures. *Nano Lett.* **2015**, *15*, 641–648.

(19) Dejarld, M.; Shin, J. C.; Chern, W.; Chanda, D.; Balasundaram, K.; Rogers, J. A.; Li, X. Formation of High Aspect Ratio GaAs Nanostructures with Metal-Assisted Chemical Etching. *Nano Lett.* **2011**, *11*, 5259–5263.

(20) Kong, L.; Song, Y.; Kim, J. D.; Yu, L.; Wasserman, D.; Chim, W. K.; Chiam, S. Y.; Li, X. Damage-Free Smooth-Sidewall InGaAs Nanopillar Array by Metal-Assisted Chemical Etching. *ACS Nano* **2017**, *11*, 10193–10205.

(21) Michaels, J. A.; Janavicius, L.; Wu, X.; Chan, C.; Huang, H.; Namiki, S.; Kim, M.; Sievers, D.; Li, X. Producing Silicon Carbide Micro and Nanostructures by Plasma-Free Metal-Assisted Chemical Etching. *Adv. Funct. Mater.* **2021**, *31*, 2103298.

(22) Tavendale, A. J.; Pearton, S. J. Deep Level, Quenched-in Defects in Silicon Doped with Gold, Silver, Iron, Copper or Nickel. *J. Phys. C Solid State Phys.* **1983**, *16*, 1665–1673.

(23) Hu, Y.; Fu, H.; Wang, J.; Sun, R.; Wu, L.; Liu, Y.; Xu, J.; Liu, J.; Peng, K. Q. Carbon Induced Galvanic Etching of Silicon in Aerated HF/H2O Vapor. *Corros. Sci.* **2019**, *157*, 268–273.

(24) Asoh, H.; Sekido, D.; Hashimoto, H. Potential of Micrometer-Sized Graphite as a Catalyst for Chemical Etching of Silicon. *Mater. Sci. Semicond. Process.* **2021**,

121, 105327.

(25) Wilhelm, T. S.; Kecskes, I. L.; Baboli, M. A.; Abrand, A.; Pierce, M. S.; Landi, B.; Puchades, I.; Mohseni, P. K. Ordered Si Micropillar Arrays via Carbon Nanotube-Assisted Chemical Etching for Applications Requiring Non-Reflective Embedded Contacts. *ACS Appl. Nano Mater.* **2019**, *2*, 7819–7826.

(26) Kim, J.; Lee, D. H.; Kim, J. H.; Choi, S. H. Graphene-Assisted Chemical Etching of Silicon Using Anodic Aluminum Oxides as Patterning Templates. *ACS Appl. Mater. Interfaces* **2015**, *7*, 24242–24246.

(27) Ogasawara, A.; Kawai, K.; Yamamura, K.; Arima, K. Nanocarbon-Induced Etching Property of Semiconductor Surfaces: Testing Nanocarbon's Catalytic Activity for Oxygen Reduction Reaction at a Single-Sheet Level. *ECS J. Solid State Sci. Technol.* **2022**, *11*, 041001.

(28) Mikurino, R.; Ogasawara, A.; Hirano, T.; Nakata, Y.; Yamashita, H.; Li, S.; Kawai, K.; Yamamura, K.; Arima, K. Catalytic Properties of Chemically Modified Graphene Sheets to Enhance Etching of Ge Surface in Water. *J. Phys. Chem. C* **2020**, *124*, 6121–6129.

(29) Hirano, T.; Nakade, K.; Li, S.; Kawai, K.; Arima, K. Chemical Etching of a Semiconductor Surface Assisted by Single Sheets of Reduced Graphene Oxide. *Carbon* **2018**, *127*, 681–687.

(30) Song, B. Y.; Qu, K.; Zhao, C.; Ren, J.; Qu, X. Graphene Oxide : Intrinsic Peroxidase Catalytic Activity and Its Application to Glucose Detection. *Adv. Mater.* **2010**, *22*, 2206–2210.

(31) Wang, B. Recent Development of Non-Platinum Catalysts for Oxygen Reduction Reaction. *J. Power Sources* **2005**, *152*, 1–15.

(32) Kamiya, K.; Hashimoto, K.; Nakanishi, S. Graphene Defects as Active Catalytic

Sites That Are Superior to Platinum Catalysts in Electrochemical Nitrate Reduction. *ChemElectroChem* **2014**, *1*, 858–862.

(33) Kovtyukhova, N. I.; Ollivier, P. J.; Martin, B. R.; Mallouk, T. E.; Buzaneva, E. V.; Gorchinskiy, A. D. Layer-by-Layer Assembly of Ultrathin Composite Films from Micron-Sized Graphite Oxide Sheets and Polycations. *Chem. Mater.* **1999**, *11*, 771–778.

(34) Geim, A. K.; Novoselov, K. S. S. The Rise of Graphene. *Nat. Mater.* **2007**, *6*, 183–191.

(35) Zhu, Y.; Murali, S.; Cai, W.; Li, X.; Suk, J. W.; Potts, J. R.; Ruoff, R. S. Graphene and Graphene Oxide: Synthesis, Properties, and Applications. *Adv. Mater.* **2010**, *22*, 3906–3924.

(36) He, H.; Klinowski, J.; Forster, M.; Lerf, A. A New Structural Model for Graphite Oxide. *Chem. Phys. Lett.* **1998**, *287*, 53–56.

(37) Paredes, J. I.; Rodil, S. V.; Alonso, A. M.; Tascón, J. M. D. Graphene Oxide Dispersions in Organic Solvents. *Langmuir* **2008**, *24*, 10560–10564.

(38) Chua, C. K.; Pumera, M. Chemical Reduction of Graphene Oxide: A Synthetic Chemistry Viewpoint. *Chem. Soc. Rev.* **2014**, *43*, 291–312.

(39) Liu, C.; Yu, Z.; Neff, D.; Zhamu, A.; Jang, B. Z. Graphene-Based Supercapacitor with an Ultrahigh Energy Density. *Nano Lett.* **2010**, *10*, 4863–4868.

(40) Shao, Y.; Wang, J.; Wu, H.; Liu, J.; Aksay, I. A.; Lin, Y. Graphene Based Electrochemical Sensors and Biosensors: A Review. *Electroanalysis* **2010**, *22*, 1027–1036.

(41) Pyun, J. Graphene Oxide as Catalyst: Application of Carbon Materials beyond Nanotechnology. *Angew. Chemie - Int. Ed.* **2011**, *50*, 46–48.

(42) Tang, C.; Zhang, Q. Nanocarbon for Oxygen Reduction Electrocatalysis:

Dopants, Edges, and Defects. *Adv. Mater.* **2017**, *29*, 1604103.

(43) Hirata, M.; Gotou, T.; Horiuchi, S.; Fujiwara, M.; Ohba, M. Thin-Film Particles of Graphite Oxide 1: High-Yield Synthesis and Flexibility of the Particles. *Carbon* **2004**, *42*, 2929–2937.

(44) Cao, J.; He, P.; Mohammed, M. A.; Zhao, X.; Young, R. J.; Derby, B.; Kinloch, I. A.; Dryfe, R. A. W. Two-Step Electrochemical Intercalation and Oxidation of Graphite for the Mass Production of Graphene Oxide. *J. Am. Chem. Soc.* **2017**, *139*, 17446–17456.

(45) Kubota, W.; Utsunomiya, T.; Ichii, T.; Sugimura, H. Local Current Mapping of Electrochemically-Exfoliated Graphene Oxide by Conductive AFM. *Jpn. J. Appl. Phys.* **2020**, *59*, SN1001.

(46) Kusunoki, I.; Igari, Y. XPS Study of a SiC Film Produced on Si(100) by Reaction with a C2H2 Beam. *Appl. Surf. Sci.* **1992**, *59*, 95–104.

(47) Tu, Y.; Ichii, T.; Utsunomiya, T.; Sugimura, H. Vacuum-Ultraviolet Photoreduction of Graphene Oxide: Electrical Conductivity of Entirely Reduced Single Sheets and Reduced Micro Line Patterns. *Appl. Phys. Lett.* **2015**, *106*, 133105.

(48) Chartier, C.; Bastide, S.; Levy-Clement, C. Metal-Assisted Chemical Etching of Silicon in HF – H 2 O 2. *Electrochim. Acta* **2008**, *53*, 5509–5516.

(49) Huang, Z.; Geyer, N.; Werner, P.; De Boor, J.; Gösele, U. Metal-Assisted Chemical Etching of Silicon: A Review. *Adv. Mater.* **2011**, *23*, 285–308.

(50) Wang, H. P.; Lai, K. Y.; Lin, Y. R.; Lin, C. A.; He, J. H. Periodic Si Nanopillar Arrays Fabricated by Colloidal Lithography and Catalytic Etching for Broadband and Omnidirectional Elimination of Fresnel Reflection. *Langmuir* **2010**, *26*, 12855–12858.

(51) Qu, L.; Liu, Y.; Baek, J.; Ḱ, L. D. Nitrogen-Doped Graphene as Efficient Metal-Free Electrocatalyst for Oxygen Reduction in Fuel Cells. *ACS Nano* **2010**, *4*, 1321–1326.

(52) Gong, K.; Du, F.; Xia, Z.; Durstock, M.; Dai, L. Nitrogen-Doped Carbon Nanotube Arrays with High Electrocatalytic Activity for Oxygen Reduction. *Science* **2009**, *323*, 760–764.

(53) Banhart, F.; Kotakoski, J.; Krasheninnikov, A. V. Structural Defects in Graphene. *ACS Nano* **2011**, *5*, 26–41.

(54) Guo, D.; Shibuya, R.; Akiba, C.; Saji, S.; Kondo, T.; Nakamura, J. Active Sites of Nitrogen-Doped Carbon Materials for Oxygen Reduction Reaction Clarified Using Model Catalysts. *Science* **2016**, *351*, 361–365.

(55) Erickson, K.; Erni, R.; Lee, Z.; Alem, N.; Gannett, W.; Zettl, A. Determination of the Local Chemical Structure of Graphene Oxide and Reduced Graphene Oxide. *Adv. Mater.* **2010**, *22*, 4467–4472.

(56) Paredes, J. I.; Villar-Rodil, S.; Solís-Fernández, P.; Martínez-Alonso, A.; Tascón, J. M. D. Atomic Force and Scanning Tunneling Microscopy Imaging of Graphene Nanosheets Derived from Graphite Oxide. *Langmuir* **2009**, *25*, 5957–5968.

(57) Tu, Y.; Utsunomiya, T.; Kokufu, S.; Soga, M.; Ichii, T.; Sugimura, H. Immobilization of Reduced Graphene Oxide on Hydrogen-Terminated Silicon Substrate as a Transparent Conductive Protector. *Langmuir* **2017**, *33*, 10765–10771.

(58) Robbins, H.; Schwartz, B. Chemical Etching of Silicon:I The System HF, HNO3 and H2O. *J. Electrochem. Soc.* **1959**, *106*, 505.

(59) Steinert, M.; Acker, J.; Wetzig, K. New Aspects on the Reduction of Nitric Acid

during Wet Chemical Etching of Silicon in Concentrated HF/HNO3 Mixtures. *J. Phys. Chem. C* **2008**, *112*, 14139–14144.

(60) Steinert, M.; Acker, J.; Oswald, S.; Wetzig, K. Study on the Mechanism of Silicon Etching in HNO 3 -Rich HF / HNO 3 Mixtures. *J. Phys. Chem. C* **2007**, *2*, 2133–2140.

(61) Steinert, M.; Acker, J.; Henßge, A.; Wetzig, K. Experimental Studies on the Mechanism of Wet Chemical Etching of Silicon in HF / HNO 3 Mixtures. *J. Electrochem. Soc.* **2005**, *152*, C843.

(62) Schwartz, B.; Robbins, H. Chemical Etching of Silicon: IV. Etching Technology. *J. Electrochem. Soc.* **1976**, *123*, 1903–1909.

(63) Schwartz, B.; Robbins, H. Chemical Etching of Silicon: III . A Temperature Study in the Acid System. *J. Electrochem. Soc.* **1961**, *108*, 365–372.

(64) De Groot, M. T.; Koper, M. T. M. The Influence of Nitrate Concentration and Acidity on the Electrocatalytic Reduction of Nitrate on Platinum. *J. Electroanal. Chem.* **2004**, *562*, 81–94.

(65) Dima, G. E.; Beltramo, G. L.; Koper, M. T. M. Nitrate Reduction on Single-Crystal Platinum Electrodes. *Electrochim. Acta* **2005**, *50*, 4318–4326.

(66) Tao, L.; Wang, Q.; Dou, S.; Ma, Z.; Huo, J.; Wang, S.; Dai, L. Edge-Rich and Dopant-Free Graphene as a Highly Efficient Metal-Free Electrocatalyst for the Oxygen Reduction Reaction. *Chem. Commun.* **2016**, *52*, 2764–2767.

(67) Lacina, K.; Kubesa, O.; Vanýsek, P.; Horáčková, V.; Moravec, Z.; Skládal, P. Selective Electrocatalysis of Reduced Graphene Oxide towards Hydrogen Peroxide Aiming Oxidases-Based Biosensing: Caution While Interpreting. *Electrochim. Acta* **2017**, *223*, 1–7.

(68) Lucchese, M. M.; Stavale, F.; Ferreira, E. H. M.; Vilani, C.; Moutinho, M. V. O.;

Capaz, R. B.; Achete, C. A.; Jorio, A. Quantifying Ion-Induced Defects and Raman Relaxation Length in Graphene. *Carbon* **2010**, *48*, 1592–1597.

(69) Yang, J.; Calle-Vallejo, F.; Duca, M.; Koper, M. T. M. Electrocatalytic Reduction of Nitrate on a Pt Electrode Modified by P-Block Metal Adatoms in Acid Solution. *ChemCatChem* **2013**, *5*, 1773–1783.

(70) Calle-Vallejo, F.; Huang, M.; Henry, J. B.; Koper, M. T. M.; Bandarenka, A. S. Theoretical Design and Experimental Implementation of Ag/Au Electrodes for the Electrochemical Reduction of Nitrate. *Phys. Chem. Chem. Phys.* **2013**, *15*, 3196–3202.

(71) Sidik, R. A.; Anderson, A. B.; Subramanian, N. P.; Kumaraguru, S. P.; Popov, B. N. O_2 Reduction on Graphite and Nitrogen-Doped Graphite: Experiment and Theory. *J. Phys. Chem. B* **2006**, *110*, 1787–1793.

(72) Hildreth, O. J.; Schmidt, D. R. Vapor Phase Metal-Assisted Chemical Etching of Silicon. *Adv. Funct. Mater.* **2014**, *24*, 3827–3833.

(73) Tsujino, K.; Matsumura, M. Morphology of Nanoholes Formed in Silicon by Wet Etching in Solutions Containing HF and H2O2 at Different Concentrations Using Silver Nanoparticles as Catalysts. *Electrochim. Acta* **2007**, *53*, 28–34.

(74) Allen, M. J.; Tung, V. C.; Gomez, L.; Xu, Z.; Chen, L. M.; Nelson, K. S.; Zhou, C.; Kaner, R. B.; Yang, Y. Soft Transfer Printing of Chemically Converted Graphene. *Adv. Mater.* **2009**, *21*, 2098–2102.

(75) Xiao, P.; Gu, J.; Chen, J.; Zhang, J.; Xing, R.; Han, Y.; Fu, J.; Wang, W.; Chen, T. Micro-Contact Printing of Graphene Oxide Nanosheets for Fabricating Patterned Polymer Brushes. *Chem. Commun.* **2014**, *50*, 7103–7106.

(76) Perl, A.; Reinhoudt, D. N.; Huskens, J. Microcontact Printing: Limitations and Achievements. *Adv. Mater.* **2009**, *21*, 2257–2268.

(77) Wu, C. T.; Utsunomiya, T.; Ichii, T.; Sugimura, H. Microstructured SiOx/COP Stamps for Patterning TiO2on Polymer Substrates via Microcontact Printing. *Langmuir* **2020**, *36*, 10933–10940.

(78) Wu, C. T.; Soliman, A. I. A.; Utsunomiya, T.; Ichii, T.; Sugimura, H. Formation of Submicron-Sized Silica Patterns on Flexible Polymer Substrates Based on Vacuum Ultraviolet Photo-Oxidation. *RSC Adv.* **2019**, *9*, 32313–32322.

(79) Kubota, W.; Ishizuka, R.; Utsunomiya, T.; Ichii, T.; Sugimura, H. Chemical Etching of Silicon Assisted by Graphene Oxide. *Jpn. J. Appl. Phys.* **2019**, *58*, 050924.

(80) Kubota, W.; Utsunomiya, T.; Ichii, T.; Sugimura, H. Chemical Etching of Silicon Assisted by Graphene Oxide in an HF-HNO3 Solution and Its Catalytic Mechanism. *Langmuir* **2021**, *37*, 9920–9926.

(81) Alfonsetti, R.; Lozzi, L.; Passacantando, M.; Picozzi, P.; Santucci B ’, S. XPS Studies on SiOx Thin Films. *Appl. Surf. Sci.* **1993**, *70*, 222–225.

(82) Keister, J. W.; Rowe, J. E.; Kolodziej, J. J.; Niimi, H.; Tao, H.-S.; Madey, T. E.; Lucovsky, G. Structure of Ultrathin SiO2/Si(111) Interfaces Studied by Photoelectron Spectroscopy. *J. Vac. Sci. Technol. A Vacuum, Surfaces, Film.* **1999**, *17*, 1250–1257.

(83) Kim, J. D.; Kim, M.; Chan, C.; Draeger, N.; Coleman, J. J.; Li, X. CMOS-Compatible Catalyst for MacEtch: Titanium Nitride-Assisted Chemical Etching in Vapor Phase for High Aspect Ratio Silicon Nanostructures. *ACS Appl. Mater. Interfaces* **2019**, *11*, 27371–27377.

(84) Asay, D. B.; Kim, S. H. Evolution of the Adsorbed Water Layer Structure on Silicon Oxide at Room Temperature. *J. Phys. Chem. B* **2005**, *109*, 16760–16763.

(85) Fukuta, Y.; Fujita, H.; Toshiyoshi, H. Vapor Hydrofluoric Acid Sacrificial

Release Technique for Micro Electro Mechanical Systems Using Labware. *Japanese J. Appl. Physics, Part 1 Regul. Pap. Short Notes Rev. Pap.* **2003**, *42*, 3690–3694.

(86) Rietig, A.; Langner, T.; Acker, J. A Revised Model of Silicon Oxidation during the Dissolution of Silicon in HF/HNO3 Mixtures. *Phys. Chem. Chem. Phys.* **2019**, *21*, 22002–22013.

(87) Gondek, C.; Lippold, M.; Röver, I.; Bohmhammel, K.; Kroke, E. Etching Silicon with Hf-H2o2-Based Mixtures: Reactivity Studies and Surface Investigations. *J. Phys. Chem. C* **2014**, *118*, 2044–2051.

(88) Granitzer, P.; Rumpf, K. *Nanostructured Semiconductors: From Basic Research to Applications*; Jenny Stanford Publishing, 2014.

(89) Matsumoto, A.; Son, H.; Eguchi, M.; Iwamoto, K.; Shimada, Y.; Furukawa, K.; Yae, S. General Corrosion during Metal-Assisted Etching of: N -Type Silicon Using Different Metal Catalysts of Silver, Gold, and Platinum. *RSC Adv.* **2019**, *10*, 253–259.

(90) Balasundaram, K.; Sadhu, J. S.; Shin, J. C.; Azeredo, B.; Chanda, D.; Malik, M.; Hsu, K.; Rogers, J. A.; Ferreira, P.; Sinha, S.; Li, X. Porosity Control in Metal-Assisted Chemical Etching of Degenerately Doped Silicon Nanowires. *Nanotechnology* **2012**, *23*, 305304.

(91) Romano, L.; Kagias, M.; Vila-Comamala, J.; Jefimovs, K.; Tseng, L. T.; Guzenko, V. A.; Stampanoni, M. Metal Assisted Chemical Etching of Silicon in the Gas Phase: A Nanofabrication Platform for X-Ray Optics. *Nanoscale Horizons* **2020**, *5*, 869–879.

(92) Fan, X.; Wagner, S.; Schädlich, P.; Speck, F.; Kataria, S.; Haraldsson, T.; Seyller, T.; Lemme, M. C.; Niklaus, F. Direct Observation of Grain Boundaries

in Graphene through Vapor Hydrofluoric Acid (VHF) Exposure. *Sci. Adv.* **2018**, *4*, 1–10.

(93) Fan, X.; Siris, R.; Hartwig, O.; Duesberg, G. S.; Niklaus, F. Rapid and Large-Area Visualization of Grain Boundaries in MoS 2 on SiO 2 Using Vapor Hydrofluoric Acid. *ACS Appl. Mater. Interfaces* **2020**, *12*, 34049–34057.

(94) Habuka, H.; Otsuka, T. Reaction of Hydrogen Fluoride Gas at High Temperatures with Silicon Oxide Film and Silicon Surface. *Japanese J. Appl. Physics, Part 1 Regul. Pap. Short Notes Rev. Pap.* **1998**, *37*, 6123–6127.

(95) Helms, C. R.; Deal, B. E. Mechanisms of the HF/H 2 O Vapor Phase Etching of SiO 2 . *J. Vac. Sci. Technol. A Vacuum, Surfaces, Film.* **1992**, *10*, 806–811.

(96) Parker, J. H.; Feldman, D. W.; Ashkin, M. Raman Scattering by Silicon and Germanium. *Phys. Rev.* **1967**, *155*, 712–714.

(97) Basko, A. C.; Denis, M. F. Raman Spectroscopy as a Versatile Tool for Studying the Properties of Graphene. *Nature Nanotechnology*. 2013, pp 234–246.

(98) Shinohara, H.; Mizuno, J.; Shoji, S. Studies on Low-Temperature Direct Bonding of VUV, VUV/O3 and O2 Plasma Pretreated Cyclo-Olefin Polymer. *Sensors Actuators, A Phys.* **2011**, *165*, 124–131.

(99) Safaei, A.; Chandra, S.; Leuenberger, M. N.; Chanda, D. Wide Angle Dynamically Tunable Enhanced Infrared Absorption on Large-Area Nanopatterned Graphene. *ACS Nano* **2019**, *13*, 421–428.

(100) Zhang, Y.; Guo, L.; Wei, S.; He, Y.; Xia, H.; Chen, Q.; Sun, H.-B. B.; Xiao, F.-S. S. Direct Imprinting of Microcircuits on Graphene Oxides Film by Femtosecond Laser Reduction. *Nano Today* **2010**, *5*, 15–20.

(101) Yang, R.; Zhang, L.; Wang, Y.; Shi, Z.; Shi, D.; Gao, H.; Wang, E.; Zhang, G. An Anisotropic Etching Effect in the Graphene Basal Plane. *Adv. Mater.* **2010**,

22, 4014–4019.

(102) Song, Y.; Mohseni, P. K.; Kim, S. H.; Shin, J. C.; Ishihara, T.; Adesida, I.; Li, X. Ultra-High Aspect Ratio InP Junctionless FinFETs by a Novel Wet Etching Method. *IEEE Electron Device Lett.* **2016**, *37*, 970–973.

(103) Wallentin, J.; Anttu, N.; Asoli, D.; Huffman, M.; Åberg, I.; Magnusson, M. H.; Siefer, G.; Fuss-Kailuweit, P.; Dimroth, F.; Witzigmann, B.; Xu, H. Q.; Samuelson, L.; Deppert, K.; Borgström, M. T. InP Nanowire Array Solar Cells Achieving 13.8% Efficiency by Exceeding the Ray Optics Limit. *Science* **2013**, *339*, 1057–1060.

(104) Yokoyama, T.; Asoh, H.; Ono, S. Site-Selective Anodic Etching of InP Substrate Using Self-Organized Spheres as Mask. *Phys. Status Solidi Appl. Mater. Sci.* **2010**, *207*, 943–946.

(105) Faur, M.; Faur, M.; Jayne, D. T.; Goradia, M.; Goradia, C. XPS Investigation of Anodic Oxides Grown on P-Type InP. *Surf. Interface Anal.* **1990**, *15*, 641–650.

(106) Fairley, N.; Fernandez, V.; Richard-Plouet, M.; Guillot-Deudon, C.; Walton, J.; Smith, E.; Flahaut, D.; Greiner, M.; Biesinger, M.; Tougaard, S.; Morgan, D.; Baltrusaitis, J. Systematic and Collaborative Approach to Problem Solving Using X-Ray Photoelectron Spectroscopy. *Appl. Surf. Sci. Adv.* **2021**, *5*, 100112.

(107) Adachi, S.; Kawaguchi, H. Chemical Etching Characteristics of (001) InP. *J. Electrochem. Soc.* **1981**, *128*, 1342–1349.

(108) Hollinger, G.; Bergignat, E.; Joseph, J.; Robach, Y. On the Nature of Oxides on InP Surfaces. *J. Vac. Sci. Technol. A Vacuum, Surfaces, Film.* **1985**, *3*, 2082–2088.

(109) Cuypers, D.; De Gendt, S.; Arnauts, S.; Paulussen, K.; van Dorp, D. H. Wet Chemical Etching of InP for Cleaning Applications. *ECS J. Solid State Sci.*

Technol. **2013**, *2*, P185–P189.

(110) Liu, H. C.; Tsai, S. H.; Hsu, J. W.; Shih, H. C. The Phase Identification of H 2 SO 4 - Etched InP by X-Ray Diffraction. *J. Electrochem. Soc.* **1999**, *146*, 3510–3515.

(111) Notten, P. H. L. The Etching of InP in HCl Solutions: A Chemical Mechanism. *J. Electrochem. Soc.* **1984**, *131*, 2641–2644.

(112) Cuypers, D.; De Gendt, S.; Arnauts, S.; Paulussen, K.; van Dorp, D. H. Wet Chemical Etching of InP for Cleaning Applications. *ECS J. Solid State Sci. Technol.* **2013**, *2*, P185–P189.

(113) Chen, Y.; Zhang, C.; Li, L.; Zhou, S.; Chen, X.; Gao, J.; Zhao, N.; Wong, C. P. Hybrid Anodic and Metal-Assisted Chemical Etching Method Enabling Fabrication of Silicon Carbide Nanowires. *Small* **2019**, *15*, 1–8.

(114) Wang, Q.; Zhou, K.; Zhao, S.; Yang, W.; Zhang, H.; Yan, W.; Huang, Y.; Yuan, G. Metal-Assisted Chemical Etching for Anisotropic Deep Trenching of GaN Array. *Nanomaterials* **2021**, *11*.

(115) Horikiri, F.; Ohta, H.; Asai, N.; Narita, Y.; Yoshida, T.; Mishima, T. Excellent Potential of Photo-Electrochemical Etching for Fabricating High-Aspect-Ratio Deep Trenches in Gallium Nitride. *Appl. Phys. Express* **2018**, *11*, 091001.

(116) Mathkar, A.; Tozier, D.; Cox, P.; Ong, P.; Galande, C.; Balakrishnan, K.; Leela, A.; Reddy, M.; Ajayan, P. M. Controlled, Stepwise Reduction and Band Gap Manipulation of Graphene Oxide. **2012**.

(117) K. S. Novoselov; Geim, A. K.; Morozov, S. V.; Jiang, D.; Zhang, Y.; Dubonos, S. V.; Grigorieva, I. V.; A. A. Firsov. Electric Field Effect in Atomically Thin Carbon Films. *Nature* **2004**, *306*, 666.

(118) Lee, C.; Wei, X.; Kysar, J. W.; Hone, J. Measurement of the Elastic Properties

and Intrinsic Strength of Monolayer Graphene. *Science.* **2008**, *321*, 385–388.

(119) Balandin, A. A.; Ghosh, S.; Bao, W.; Calizo, I.; Teweldebrhan, D.; Miao, F.; Lau, C. N. Superior Thermal Conductivity of Single-Layer Graphene. *Nano Lett.* **2008**, *8*, 902–907.

(120) Wassei, J. K.; Kaner, R. B. Graphene, a Promising Transparent Conductor. *Mater. Today* **2010**, *13*, 52–59.

(121) Li, X.; Cai, W.; An, J.; Kim, S.; Nah, J.; Yang, D.; Piner, R.; Velamakanni, A.; Jung, I.; Tutuc, E.; Banerjee, S. K.; Colombo, L.; Ruoff, R. S. Large-Area Synthesis of High-Quality and Uniform Graphene Films on Copper Foils. *Science* **2009**, *324*, 1312–1314.

(122) Berger, C.; Song, Z.; Li, T.; Li, X.; Ogbazghi, A. Y.; Feng, R.; Dai, Z.; Alexei, N.; Conrad, M. E. H.; First, P. N.; De Heer, W. A. Ultrathin Epitaxial Graphite: 2D Electron Gas Properties and a Route toward Graphene-Based Nanoelectronics. *J. Phys. Chem. B* **2004**, *108*, 19912–19916.

(123) Mao, S.; Pu, H.; Chen, J. Graphene Oxide and Its Reduction: Modeling and Experimental Progress. *RSC Adv.* **2012**, *2*, 2643–2662.

(124) Suk, J. W.; Kitt, A.; Magnuson, C. W.; Hao, Y.; Ahmed, S.; An, J.; Swan, A. K.; Goldberg, B. B.; Ruoff, R. S. Transfer of CVD-Grown Monolayer Graphene onto Arbitrary Substrates. *ACS Nano* **2011**, *5*, 6916–6924.

(125) Yang, S.; Brüller, S.; Wu, Z. S.; Liu, Z.; Parvez, K.; Dong, R.; Richard, F.; Samorì, P.; Feng, X.; Müllen, K. Organic Radical-Assisted Electrochemical Exfoliation for the Scalable Production of High-Quality Graphene. *J. Am. Chem. Soc.* **2015**, *137*, 13927–13932.

(126) Parvez, K.; Wu, Z. S.; Li, R.; Liu, X.; Graf, R.; Feng, X.; Müllen, K. Exfoliation of Graphite into Graphene in Aqueous Solutions of Inorganic Salts. *J. Am. Chem.*

Soc. **2014**, *136*, 6083–6091.

(127) Parvez, K.; Li, R.; Puniredd, S. R.; Hernandez, Y.; Hinkel, F.; Wang, S.; Feng, X.; Müllen, K. Electrochemically Exfoliated Graphene as Solution-Processable, Highly Conductive Electrodes for Organic Electronics. *ACS Nano* **2013**, *7*, 3598–3606.

(128) Munuera, J. M.; Paredes, J. I.; Enterría, M.; Pagán, A.; Villar-Rodil, S.; Pereira, M. F. R.; Martins, J. I.; Figueiredo, J. L.; Cenis, J. L.; Martínez-Alonso, A.; Tascón, J. M. D. Electrochemical Exfoliation of Graphite in Aqueous Sodium Halide Electrolytes toward Low Oxygen Content Graphene for Energy and Environmental Applications. *ACS Appl. Mater. Interfaces* **2017**, *9*, 24085–24099.

(129) Lu, J.; Yang, J.; Wang, J.; Lim, A.; Wang, S.; Loh, K. P. One-Pot Synthesis of Fluorescent Carbon Graphene by the Exfoliation of Graphite in Ionic Liquids. *ACS Nano* **2009**, *3*, 2367–2375.

(130) Yang, D.; Velamakanni, A.; Bozoklu, G.; Park, S.; Stoller, M.; Piner, R. D.; Stankovich, S.; Jung, I.; Field, D. A.; Ventrice, C. A.; Ruoff, R. S. Chemical Analysis of Graphene Oxide Films after Heat and Chemical Treatments by X-Ray Photoelectron and Micro-Raman Spectroscopy. *Carbon* **2009**, *47*, 145–152.

(131) Ferrari, A. C.; Basko, D. M. Raman Spectroscopy as a Versatile Tool for Studying the Properties of Graphene. *Nat. Nanotechnol.* **2013**, *8*, 235–246.

(132) Li, C.; Bando, Y.; Golberg, D. Current Imaging and Electromigration-Induced Splitting of GaN Nanowires as Revealed by Conductive Atomic Force Microscopy. *ACS Nano* **2010**, *4*, 2422–2428.

(133) Dai, H.; Wong, E. W.; Lieber, C. M. Probing Electrical Transport in Nanomaterials: Conductivity of Individual Carbon Nanotubes. *Science* **1996**, *272*, 523–526.

(134) Otsuka, Y.; Naitoh, Y.; Matsumoto, T.; Kawai, T. Point-Contact Current-Imaging Atomic Force Microscopy: Measurement of Contact Resistance between Single-Walled Carbon Nanotubes in a Bundle. *Appl. Phys. Lett.* **2003**, *82*, 1944–1946.

(135) Mativetsky, J. M.; Treossi, E.; Orgiu, E.; Melucci, M.; Veronese, G. P.; Samorì, P.; Palermo, V. Local Current Mapping and Patterning of Reduced Graphene Oxide. *J. Am. Chem. Soc.* **2010**, *132*, 14130–14136.

(136) Tu, Y.; Nakamoto, H.; Ichii, T.; Utsunomiya, T.; Khatri, O. P.; Sugimura, H. Fabrication of Reduced Graphene Oxide Micro Patterns by Vacuum-Ultraviolet Irradiation: From Chemical and Structural Evolution to Improving Patterning Precision by Light Collimation. *Carbon* **2017**, *119*, 82–90.

(137) Kudin, K. N.; Ozbas, B.; Schniepp, H. C.; Prud'homme, R. K.; Aksay, I. A.; Car, R. Raman Spectra of Graphite Oxide and Functionalized Graphene Sheets. *Nano Lett.* **2008**, *8*, 36–41.

(138) Nemanich, R. J.; Solin, S. A. First- and Second-Order Raman Scattering from Finite-Size Crystals of Graphite. *Phys. Rev. B* **1979**, *2*, 392–401.

(139) Nagashio, K.; Nishimura, T.; Kita, K.; Toriumi, A. Systematic Investigation of the Intrinsic Channel Properties and Contact Resistance of Monolayer and Multilayer Graphene Field-Effect Transistor. *Jpn. J. Appl. Phys.* **2010**, *49*, 0513041–0513046.

(140) Tu, Y.; Utsunomiya, T.; Ichii, T.; Sugimura, H. Enhancing the Electrical Conductivity of Vacuum-Ultraviolet-Reduced Graphene Oxide by Multilayered Stacking. *J. Vac. Sci. Technol. B, Nanotechnol. Microelectron. Mater. Process. Meas. Phenom.* **2017**, *35*, 03D110.

(141) He, H.; Riedl, T.; Lerf, A.; Klinowski, J. Solid-State NMR Studies of the

Structure of Graphite Oxide. *J. Phys. Chem.* **1996**, *100*, 19954–19958.

(142) Ghaderi, N.; Peressi, M. First-Principle Study of Hydroxyl Functional Groups on Pristine, Defected Graphene, and Graphene Epoxide. *J. Phys. Chem. C* **2010**, *114*, 21625–21630.

(143) Hirotomi, Y.; Kubota, W.; Utsunomiya, T.; Ichii, T.; Sugimura, H. Fabrication of Reduced Graphene Oxide with High Electrical Conductivity by Thermal-Assisted Photoreduction of Electrochemically-Exfoliated Graphene Oxide. *Jpn. J. Appl. Phys.* **2022**, *61*, SL1012.

Achievements

Original papers

[1]Wataru Kubota, Ryuko Ishizuka, Toru Utsunomiya, Takashi Ichii, Hiroyuki Sugimura "Chemical etching of silicon assisted by graphene oxide" *Jpn. J. Appl. Phys.* **58**, 050924 (2020)

[2]Wataru Kubota, Toru Utsunomiya, Takashi Ichii, Hiroyuki Sugimura "Local current mapping of electrochemically-exfoliated graphene oxide by conductive AFM" *Jpn. J. Appl. Phys.* **59**, SN1001 (2020)

[3]Wataru Kubota, Toru Utsunomiya, Takashi Ichii, Hiroyuki Sugimura "Chemical Etching of Silicon Assisted by Graphene Oxide in an HF–HNO_3 Solution and Its Catalytic Mechanism" *Langmuir* **37**, 9920 (2021)

[4]Wataru Kubota, Ryoya Yamaoka, Toru Utsunomiya, Takashi Ichii, Hiroyuki Sugimura "Vapor phase chemical etching of silicon assisted by graphene oxide for microfabrication and micro-contact printing" *ACS Appl. Nano Mater.* **5**, 11707 (2022)

[5]Wataru Kubota, Toru Utsunomiya, Takashi Ichii, Hiroyuki Sugimura "Chemical etching of InP assisted by graphene oxide." *Jpn. J. Appl. Phys.,* Submitted.

International Conference

[1]Wataru Kubota, Ryuko Ishizuka, Toru Utsunomiya, Takashi Ichii, Hiroyuki Sugimura, "Chemical etching of Si assisted by two types of graphene oxide." 3rd International Symposium on Anodizing Science and Technology, 2019（Poster）

[2]Wataru Kubota, Toru Utsunomiya, Takashi Ichii, Hiroyuki Sugimura, "Local current mapping of electrochemically-exfoliated graphene oxide by conductive AFM." 27th International Colloquium on Scanning Probe Microscopy, 2019（Poster）

[3]Wataru Kubota, Toru Utsunomiya, Takashi Ichii, Hiroyuki Sugimura, “Chemical Etching of Silicon Assisted by Graphene Oxide in HF-H_2O_2 Vapor.” Interfinish2020 20th world congress, 2021（Oral）

[4]Wataru Kubota, Ryoya Yamaoka, Toru Utsunomiya, Takashi Ichii, Hiroyuki Sugimura, “Pattern etching of silicon assisted by graphene oxide in a vapor phase combined with micro-contact printing” IVC-22, 2022　（Oral）

[5]Wataru Kubota, Toru Utsunomiya, Takashi Ichii, Hiroyuki Sugimura, “Chemical etching of InP assisted by graphene oxide.” MNC-2022, 2022（Poster）

Domestic Conference

[1]窪田 航，宇都宮 徹，一井 崇，杉村 博之，「電気化学剥離による酸化グラフェンの作製及び光還元」第 20 回関西表面技術フォーラム，2018 年（ポスター）

[2]窪田 航，宇都宮 徹，一井 崇，杉村 博之，「電気化学酸化法による酸化グラフェンの作製及び Si エッチング」平成 30 年度日本鉄鋼協会・日本金属学会関西支部鉄鋼プロセス研究会・材料化学研究会第 2 回合同研究会, 2018 年（ポスター）

[3]窪田 航，石塚 隆高, 宇都宮 徹，一井 崇，杉村 博之「酸化グラフェンアシスト Si エッチングの反応メカニズム解明」第 66 回応用物理学会春季学術講演会，2019 年（ポスター）

[4]窪田 航，宇都宮 徹，一井 崇，杉村 博之「HF-HNO_3 エッチング液を用いた酸化グラフェンアシストシリコンエッチング」第 80 回応用物理学会秋季学術講演会 2019 年（口頭）

[5]窪田 航，宇都宮 徹，一井 崇，杉村 博之 ”Development of graphene oxide assisted silicon etching.” 第 2 回先端ナノミクス若手研究者交流会 2019 年（ポスター）

[6]窪田 航，宇都宮 徹，一井 崇，杉村 博之「酸化グラフェンアシストシリコンエッチングにおける反応活性点」 第 81 回応用物理学会秋季学術講演会 2020（口頭）

[7]窪田 航，宇都宮 徹，一井 崇，杉村 博之 「ふっ硝酸を用いた酸化グラフェンアシストシリコンエッチング」 表面技術協会第 143 回講演大会 2021（口頭）

[8]窪田 航，宇都宮 徹，一井 崇，杉村 博之「気相中酸化グラフェンアシストシリコンエッチング」 第 68 回応用物理学会春季学術講演会 2021（口頭）

[9]窪田 航，宇都宮 徹，一井 崇，杉村 博之「酸化グラフェンマイクロパターンを援用したシリコンの気相中エッチング」第 82 回応用物理学会秋季学術講演会 2021（口頭）

[10]窪田 航，山岡 遼也，宇都宮 徹，一井 崇，杉村 博之「酸化グラフェンマイクロパターンを援用した気相中シリコンエッチング」先端ナノミクス若手研究者交流会 2022 (ポスター)

[11]窪田 航，宇都宮 徹，一井 崇，杉村 博之「酸化グラフェンアシスト InP エッチング法の開発」表面技術協会第 145 回講演大会 2022（ポスター）

[12]窪田 航，宇都宮 徹，一井 崇，杉村 博之「InP 基板の酸化グラフェンアシストエッチング」第 69 回応用物理学会春季学術講演会 2022（口頭）

[13]窪田 航，山岡 遼也，宇都宮 徹，一井 崇，杉村 博之「マイクロコンタクトプリンティングを併用したシリコンの気相中酸化グラフェンアシストエッチング」第 83 回応用物理学会秋季学術講演会 2022（口頭）

Acknowledgments

First, I would like to express my deepest appreciation to my supervisor Prof. Dr. Hiroyuki Sugimura for giving me the opportunity to do my master and PhD work in the Nanoscopic Surface Architecture Laboratory (NSA Lab) at Kyoto University. His deep knowledge in the field of surface science expanded the possibility of my research work. Moreover, he gave me the opportunity to stay in India, which was my first chance to go abroad, and the short stay in India was a valuable experience to have a relationship with foreign researchers and changed my value.

I also want to express my gratitude to Prof. Dr. Kuniaki Murase and Prof. Dr. Tetsuya Uda for dedicating time and attention to understand my research and offering constructive advice to improve my dissertation. Their suggestions and feedback gave me the opportunity to review my research work from different perspectives.

I am deeply grateful to Prof. Dr. Takashi Ichii and Prof. Dr. Toru Utsunomiya for all the instruction they have given me in my 6 years in the lab. Not only their advice for my research work but also their attitude towards what researchers should be were indispensable for my growth in PhD course.

I want to thank Ms. Setsuko Yoshikubo for supporting my daily research work. Her assistance enables me to do my research work efficiently. I also want to express my gratitude to Ms. Sari Nakano for her assistance in handling my university documents while Ms. Yoshikubo was away.

I want to thank Mr. Yutaka Sonobayashi, Mr. Kenji Kazumi, and Mr. Nobuharu Sasaki for their support in utilizing XPS and SEM. Their expertise in the equipment is essential for the analysis of my research work.

I cannot sufficiently appreciate Mr. Yuya Yamada for his constant encouragement. He has shared both pleasant and hard experiences in our 6-year bachelor, master and PhD

course. Without his encouragement, I have not been able to complete my PhD course in which many things were restricted by COVID-19. I also thank my colleague, Mr. Kosuke Imura and Mr. Toru Hiwasa for their hearty encouragement in my master course.

I would like to express my appreciation to the Postdoctoral researcher of Dr. Harshal Prakashrao Mungse and Dr. Ahmed Ibrahim Abdelhamid Soliman, and my senior PhD student in NSA Lab, Dr. Yudi Tu, Dr. Cheng Tsu Wu, Dr. Mitsuhiro Gonda, and Maria Carmela Tan Garcia, and my junior PhD course student, Mr. Yifan Bao, for their insightful indicates and meaningful discussion in the weekly meeting or daily discussion.

I want to thank all of the NSA lab members. Especially, I would like to express my sincere appreciation to my senior master course students, Mr. Yuki Takatani, Mr. Yuya Takara, Mr. Makoto Yoneda, Ms. Zixin Luo, Mr. Ryuko Ishizuka, Mr. Kazuyuki Itakura, Mr. Katsufumi Okamoto, Ms. Lithing Lin, and Mr. Makoto Murata for taking the time to teach me how to handle the equipment and other matters related to the laboratory. I also would like to give special thanks to Mr. Ryuko Ishizuka, Mr. Hiroshi Shimakawa, Mr. Ryoya Yamaoka, Mr. Yuji Hirotomi, Mr. Yuta Goto, and Mr. Kaichi Yamamoto for their collaboration in the field of graphene oxide division in NSA Lab.

I want to express my appreciation to the Japan Society for the Promotion of Science (JSPS) for their financial support during my PhD course. Without the scholarship, my life in PhD course would not have been possible for me.

Finally, I want to thank my family for their endless support in my PhD course, and to offer my special thanks to all the members of B3 floor in Kumano Dormitory for their hearty daily communication.

Wataru Kubota